Manipulating & measuring quantum ghosts & randomness

Nicholas Bornman

Supervisor: Prof. Andrew Forbes

School of Physics
University of the Witwatersrand

A thesis submitted to the Faculty of Science in fulfilment of the requirements for the degree of
Doctor of Philosophy

May 2021

To my dear late mother,

Sirena Lynn Bornman
6 February 1958 - 28 November 2018

You were the best mother I could ever have hoped for. I'm unsure whether I'll ever be able to pull myself together again, but my memories of you help me move forward.

"Sometimes hope for the future is found in the ashes of yesterday" - Karen Kingsbury

Declaration

I hereby declare that this thesis is my own, unaided work (except where acknowledgements indicate otherwise). It is being submitted for the degree of Doctor of Philosophy at the University of the Witwatersrand, Johannesburg. It has not been submitted before for any degree or examination at any other university.

Nicholas Bornman
May 2021

Acknowledgements

Throughout my doctoral studies, many people have provided both direct and indirect support. I would like to pay homage to a number of them.

First and foremost, to my supervisor Professor Andrew Forbes, I wish to express my deepest gratitude. I have heard people say that one's choice of academic supervisor is just as important as the topic itself, and in you I had a supervisor and mentor second to none. Thank you for your constant pushing, constructive feedback and understanding when things were going well and also when they weren't. The hard and soft skills I have learned from you and the opportunities you've afforded me are truly invaluable.

To all my friends in both the Structured Light Laboratory as well as external colleagues, I thank you for all the technical help and guidance as well as the innumerable light-hearted moments which made this endeavour much more enjoyable.

Finally, I wish to thank my loving family. To my late mother Sirena: not a day goes by that I don't miss you. You moulded me into the man I am today, and I love you dearly. I've been crushed since your passing, but I take some comfort in the fact that your suffering has passed and that I know you would have been very proud of me. To my father Pieter, brother Joshua and sister-in-law Ani: the past few years have been torrid and I would not have been able to get through this endeavour without you. Thanks for all the support. I love you guys.

This work was supported with generous funding from the National Research Foundation and the DSI–CSIR Inter-bursary programme.

Abstract

Despite having been around for roughly 85 years, quantum mechanics continues to produce many surprising results. Furthermore, although theoretical work aiming to fully complete quantum mechanics is still ongoing, the form typically employed in quantum information and quantum computing studies can be axiomatised by four succinct postulates.

In this work we will discuss, in detail, four interesting quantum photonics and quantum information experiments which can neatly be divided into two groups: quantum ghost imaging and quantum random number generation. The interplay between the four postulates underpinning contemporary quantum mechanics, and the experiments themselves, will also be touched on throughout this work.

First, we present a novel four-way quantum ghost imaging setup which employs entanglement swapping to create correlations between initially completely independent down-converted biphoton states. The projection and measurement techniques used give rise to an anti-symmetric biphoton state (in contrast with the symmetric states normally used in quantum ghost imaging). This, in turn, results in a surprising 'contrast-reversed' ghost image with respect to the original object; the symmetric case would give rise to an ordinary ghost image. Such considerations of state symmetry may prove important in future higher-dimensional imaging and communication protocols which incorporate entanglement swapping (which is a key component of a future quantum network).

Second, we investigate the connection between ghost imaging and state symmetry further by using a two-way ghost imaging experiment which is modified to tailor the symmetry of the down-converted state. In this case, when postselecting on anti-symmetric subspaces, the reconstructed ghost image turns out to be a juxtaposed version of the original object, rotated both clockwise and counterclockwise. This again emphasises the importance a state's symmetry has on the observed physics.

Third, although quantum mechanics has been an extremely successful theory, it is fundamentally incomplete. We therefore explore the potential of using quantum field theory, which is a more complete set of ideas, to explain quantum ghost imag-

ing specifically and the measurement/detection process in quantum photonics more generally. We find that the so-called Unruh-DeWitt detector model is successful in explaining quantum ghost imaging when one draws an analogy between the pixels comprising the original object plus the pixels comprising the measurement device, and two arrays of Unruh-DeWitt detectors. This different approach may be a useful first step in considering quantum imaging in non-inertial reference frames and the nature of entanglement of down-converted states in nontrivial gravitational backgrounds, for example.

Finally, a key feature of quantum mechanics is the inherent indeterminacy built into the formalism, by way of the postulates. We present work whereby this uncertainty is exploited to demonstrate the generation of true higher-dimensional random numbers from the orbital angular momentum degree of freedom of down-converted biphoton states. Digital spatial light modulators are used to tailor the probability distribution of the state, allowing us to mitigate bias and imperfections in the experimental setup. With these techniques, we are able to generate more than one bit of truly random information from each orbital angular momentum detection event. Entropy and randomness are increasingly important both fundamentally and commercially, and hence such proof of principle studies are important.

List of publications

Peer-reviewed journal articles

1. **Bornman, N.**, Agnew, M., Zhu, F., Vallés, A., Forbes, A. and Leach, J., 2019. Ghost imaging using entanglement-swapped photons. *npj Quantum Information*, 5(1), pp.1-6

2. **Bornman, N.**, Prabhakar, S., Vallés, A., Leach, J. and Forbes, A., 2019. Ghost imaging with engineered quantum states by Hong–Ou–Mandel interference. *New Journal of Physics*, 21(7), p.073044

3. **Bornman, N.**, Kempf, A. and Forbes, A., 2019. Quantum imaging using relativistic detectors. *Physical Review D*, 100(12), p.125004

4. de Oliveira, M., **Bornman, N.** and Forbes, A., 2020. Holographically controlled random numbers from entangled twisted photons. *Physical Review A*, 102(3), p.032620

5. **Bornman, N.**, Forbes, A. and Kempf, A., 2020. Random number generation and distribution out of thin (or thick) air. *Journal of Optics*, 22(7), p.075705

Conference proceedings

1. **Bornman, N.**, Vallés, A., Prabhakar, S., Agnew, M., Zhu, F., Forbes, A. and Leach, J., 2019, September. Quantum ghost imaging and state symmetry. In *Quantum Communications and Quantum Imaging XVII* (vol. 11134, p. 1113406). International Society for Optics and Photonics

2. Vallés, A., **Bornman, N.**, Leach, J. and Forbes, A., 2019, September. Ghost imaging with engineered quantum states unveiling rotated objects. In *JSAP-OSA Joint Symposia* (paper 21a_E214_4). Optical Society of America.

Table of contents

List of figures

List of tables

Chapter 1

Introduction: quantum mechanics & its postulates

University corridors and cafeterias are often filled with debate between researchers of various 'hard science' disciplines over which theory of Nature has been the most groundbreaking and successful. While mathematics is rightly referred to as 'The Queen of Science', other discoveries, such as general relatively, evolution by natural selection, the kinetic theory of gasses and the Big Bang have all both revolutionised the way humanity understands the world as well as opened up countless practical opportunities. However, one theory in particular undoubtedly belongs on this list despite its somewhat chaotic genesis; its immensely far-reaching, meticulously verified yet often counterintuitive predictions; its numerous real-world applications, with many more still untouched; and its strangely persistent quality of being poorly understood from both theoretical and philosophical grounds. This great theory is quantum mechanics.

Quantum mechanics is a fundamental physical theory which provides a strong mathematical framework with which to formulate various physical laws describing nature. Although it does not specify which specific laws a particular system follows, it provides a coherent set of rules and postulates with which to develop said system [1]. Its importance in contemporary life is undergirded by its broad list of successful applications, from understanding elementary particle behaviour to an extraordinary degree of accuracy, to modelling the movement of electrons in semiconductors, to optimising the atomic fission process in nuclear reactors and to providing guaranteed security in quantum communication systems. Furthermore, despite the fact that quantum mechanics has been prototypically applied to understanding small-scale systems (on the scale of atoms and subatomic particles), by the famous *correspondence principle* (originally outlined in [2]), it should be possible to reproduce results observed on a

more macroscopic scale, such as in bio-logical or engineering systems, by appropriately scaling corresponding systems derived from baseline quantum mechanics [3]. As such, Nature is indeed quantum.

Delving deeper into quantum mechanics, many different subfields exist, all focusing on different aspects of quantum systems. For example, quantum thermodynamics focuses on the thermodynamics of quantum systems which may or may not be in equilibrium and the thermodynamic laws arising from the system's quantum nature [4], whereas particle physics studies the irreducible matter and force particles composing the universe and their interactions [5]. By instead shifting focus onto the information content of quantum systems, we arrive at the field of *quantum information*. The combination of traditional information theory (first formulated in the 1940s [6]) and quantum mechanics (which was born in the early 1900s) has prompted many deep theoretical - and philosophical - questions as to the exact nature of Nature, such as whether observables can be said to objectively exist before we measure them and how measurements performed in certain local regions of spacetime affect distant regions (the ideas behind *local realism* [1]). However, this combination has also been quite fruitful in practice, having given rise to many technologies such as completely secure communication systems [7, 8]; teleporting information from one particle to another, distant particle [9, 10]; ultra-precise quantum metrology [11]; and, of course, quantum computers, which focus on the information processing capabilities of quantum systems in that they can solve certain problems exceedingly faster than classical computers [12, 13] and potentially allow for more efficient drug research [14] and financial market modelling [15], among other applications. Quantum information (QI) will be a major focus of this thesis.

It is possible to encode information in, and perform QI experiments using, any degree of freedom of any set of particles as long as they display the requisite quantum behaviour. Modern demonstrations include single photon modes in an optical cavity coupled to an isolated, two-level atom [16], trapped and cooled ^{9}Be ions [17] and nuclear spin states [18] among others. Another approach, and the one we focus on in this thesis, is that of quantum photonic experiments whereby *optical photons* serve as the information carriers. While both traditional photon-based quantum information and, especially, quantum computation implementations have drawbacks (such as problems in scaling such systems up and interacting single photons with one another, which is usually done by way of extremely lossy nonlinear Kerr media [1]), unlike the other information carriers given above, photons are very easy to manipulate and suffer far less decoherence. Either way, quantum photonics undoubtedly holds much promise

in quantum communication and cryptographic systems [19]. Furthermore, recent discoveries open the door to scalable photonic-based quantum computers without the need for nonlinear media [20], and new models such as the cluster state approach [21, 22] provide new avenues to, for example, implement the CNOT gate (see [23] for a review). Photonics-based QI experiments were performed as part of this thesis.

There have been dozens of demonstrations of QI phenomena using photonics. While such demonstrations often overlap in some sense, the forthcoming chapters will chiefly focus on two phenomena. First, that of *quantum ghost imaging*, in which the correlations created between a pair of entangled photons are used to image an object, even though each photon individually contains no information about said object (see [24] for a comprehensive review of ghost imaging). And second, that of *quantum random number generation*, whereby the inherent indeterminacy of quantum mechanics is used as an entropic source from which to generate true random bit strings (see, for example, [25, 26] for further information on quantum randomness and randomness extraction devices). Various aspects of ghost imaging will be discussed in Chapters 2 to 4, while Chapter 5 will focus on random number generation.

Returning to our broader discussion of quantum mechanics above, an important step when formulating any theory is to axiomatise it by breaking it down into its most basic concepts and rules. These rules can then be applied to specific examples and more complicated theories can be built on said axioms. Quantum mechanics is no different. Although different sets of postulates exist, all should more or less be equivalent. A common set of such postulates is given in Chapter 2 of [1]; the quantum photonics experiments in the chapters to come will touch on the ideas contained in these postulates. They are:

Postulate 1: Given an isolated physical system, the state space of the system is an associated Hilbert space H over the field of complex numbers. The state of the system is described completely by a positive semi-definite, Hermitian, trace 1 density operator, ρ, acting on the state space. Furthermore, if the quantum system has a probability p_i of being in the state ρ_i, the density operator for this ensemble is the convex sum $\rho = \sum_i p_i \rho_i$.

Postulate 2: Lossless operations (those which don't cause a loss of information) on, and by extension, the time evolution of a closed quantum system, are described by unitary transformations: the system at time t_1, ρ_1, is related to the system at time t_2, ρ_2, by a unitary operator, U, that only depends on the times t_1, t_2, according to

$$\rho_2 = U \rho_1 U^\dagger.$$

Postulate 3: A set of measurement operators, $\{M_m\}$, which act on the state space H describe quantum measurements performed on the system. Here, m labels the possible measurement outcomes. The measurement operators satisfy the completeness relation,

$$\sum_m M_m^\dagger M_m = \mathbb{I}.$$

Given a state ρ before the measurement, the probability of observing outcome m when performing said measurement is

$$p(m) = \mathrm{Tr}\left(\rho M_m^\dagger M_m\right),$$

with the state of the system immediately after having observed m, ρ_m, being given by

$$\rho \to \rho_m = \frac{M_m \rho M_m^\dagger}{\mathrm{Tr}\left(\rho M_m^\dagger M_m\right)}.$$

Postulate 4: A composite system (one consisting of two or more distinct physical quantum systems) has a state space comprising the tensor product of the individual component Hilbert spaces. Furthermore, if subsystem i is described by the state ρ_i, the state ρ of the composite system is the tensor product of the individual subsystems, $\rho = \bigotimes_i \rho_i$.

P1 sets the stage, providing a framework with which to describe an isolated quantum system's state; **P2** describes how such a closed system evolves; **P3** outlines how we extract knowledge from the system by way of measurements; and **P4** provides us with a way of combining irreducible quantum systems into larger, composite ones [1].

With **P1** in mind, quantum theorists often assume that one simply has access to the 'ideal' initial state on which one can then perform relevant manipulations (**P2**) and subsequent measurements (**P3**). However, in practice, this is not the case. Although it is, relatively speaking, easy to generate single photons, the *deterministic, on demand* generation of single photons remains a challenge (although studies into using nitrogen-vacancy centres in diamonds [27] or trapped atoms [28] as potential sources have proven promising). Contemporary methods of generating pairs of entangled photons pose further challenges: the commonplace process of using spontaneous parametric down-conversion (SPDC), whereby a strong coherent laser source pumps a nonlinear crystal such as β-barium borate (BBO) or periodically-poled potassium titanyl phosphate (PPKTP), to generate a pair of entangled photons is probabilistic and extremely inefficient [29, 30]. However, given such a down-converted pair, the spectrum of

the various degrees of freedom one may wish to encode information in are also not optimal. For example, one often wishes to create so-called maximally-entangled states whose components have equal amplitudes, yet down-conversion creates states whose probability amplitudes taper off, especially when considering higher-dimensional degrees of freedom such as a photon's orbital angular momentum [31]. Techniques such as pump shaping [32, 33] do attempt to address this, but suffice it to say that much work still needs to be done on creating better sources which generate single and entangled photons with the requisite properties.

Instead of considering methods of generating, out of the box, the states we need, this thesis will consider both the evolution/manipulation (**P2**), and measurement (**P3**) of quantum optical states within the context of quantum ghost imaging and quantum random number generation experiments. Photons are bosons of spin 1 and therefore the wavefunction of two (or more) identical photons must be symmetric under a permutation ('swapping') of the particles [5] (i.e. for a wavefunction Ψ of two bosons each individually parameterised by $\mathbf{x}_1$ and $\mathbf{x}_2$, we must have $\Psi(\mathbf{x}_1, \mathbf{x}_2) = \Psi(\mathbf{x}_2, \mathbf{x}_1)$). However, a general quantum state consists of a superposition of pure states in which the photons may have different values for some degrees of freedom (and are hence distinguishable), and therefore, in general, could consist of both symmetric and anti-symmetric terms (where for the latter, $\Psi(\mathbf{x}_1, \mathbf{x}_2) = -\Psi(\mathbf{x}_2, \mathbf{x}_1)$). Interesting physics arises from quantum systems described by completely symmetric or completely anti-symmetric states, such as Bose-Einstein condensation [34], superconductivity [35], all the way to better understanding the collapse of stars into white dwarfs [36]. The effect that a state's symmetry has on the image obtained in quantum ghost imaging will be of fundamental importance to the discussions to come.

In particular, Chapter 2 (which is largely based on the author's work in [37]) presents a novel quantum ghost imaging protocol in which, in contrast with traditional two-photon ghost imaging experiments, the requisite correlations are created between two completely independent photons by combining and entanglement swapping two pairs of mutually independent down-converted photons. Among others, an interesting result is the counter-intuitive, 'contrast reversed' image obtained when the two-photon state is tailored to be anti-symmetric, whereas the ordinary contrast image is measured in the purely symmetric case. This manipulation (**P2**) of the state had a clear effect on the measured (**P3**) image. Such entanglement swapping protocols may also be important for any future quantum networks in which entangled quantum bits, namely *qubits* (or even higher-dimensional *qudits*) would need to be created from isolated, initially separable single photons.

Chapter 3 (which is based on [38]) considers the concept of symmetry further by studying a single entangled photon pair whose symmetry is engineered (**P2**) using a Hong-Ou-Mandel filter [39]. In contrast with the results of Chapter 2, the image obtained with this experimental setup, in the anti-symmetric projection case, is a juxtaposition of the original object rotated both clockwise and counterclockwise, resulting in a sort of 'double' image. This further speaks to the important effect a state's symmetry can have on the observed physics. However, in both of these chapters' experiments, the measurement process we employed necessarily involved *postselecting* on the observance of coincidence counts (i.e. simultaneous photon detection events) between either two (Chapter 3) or four (Chapter 2) avalanche photodiode detectors. We hence, admittedly, were not utilising the full quantum state ρ but rather a conditioned 'subset' of ρ. Furthermore, the process of postselection itself doesn't fall neatly into either **P2** (manipulation) or **P3** (measurement) in that we essentially manipulate the state, to obtain one we desire, by throwing away information *after* the measurement process. This further highlights the need for research into sources which can produce exactly the desired quantum states as well as potential measurement protocols which could forgo the need for postselection.

The postulates above are very abstract and don't provide any specific information about, for example, the laws a particular system obeys. Indeed, **P3** merely gives the probability distribution for the possible measurement outcomes, given a set of measurement operators $\{M_m\}$, and specifies the new state of the system immediately after said measurement if we indeed measure the system. Were we not to perform the measurement, the state remains unchanged, both on paper and in practice. **P3**, emphatically, does not tell us how to go about measuring a quantum system nor how a specific measurement interacts with and perturbs said system. This inherent uncertainty (in that the best we can hope for is a probability distribution, not a deterministic answer) and the strange interplay between a system's seemingly objective state and our more subjective choice of whether to observe said system or not, result in important unsolved philosophical, as well as operational, problems in physics (a famous case in point being the so-called *measurement problem* [40]). So, as tested and trusted as it is, quantum mechanics is certainly not complete.

Quantum field theory (QFT) [5] is a quantum theory which can, however, explain some observed phenomena which usual quantum mechanics cannot, such as particle creation/annihilation and transforming results between different inertial reference frames. Indeed, studying quantum informational aspects of Nature from the framework of QFT has recently given rise to the niche area of Relativistic Quantum Information (RQI) [41,

42]. And within RQI, a common model used to understand the measurement/detection process (**P3**) is the Unruh-DeWitt (UDW) detector [43, 44]. This detector consists of a local, first quantised, two-level system coupled to the quantum field we wish to probe. A typical calculation in this model involves first coupling the detector-field systems via a well-defined Hamiltonian and then allowing this composite system to evolve (**P2**). Thereafter, changes in the state of the detector at some later time can be interpreted as the detection of a particle/excitation of the field (such as the electromagnetic field) we're probing. The UDW detector model fits well in the context of quantum information experiments: it has been applied to cavity quantum electrodynamics and studying the Casimir effect [45, 46, 46], and some common models in quantum optics are in fact derivatives of the UDW detector model. Finally, given that it is based on a well-defined Hamiltonian which couples the detectors and the quantum state being measured, this model may shed a little light on the more operational complexities of the measurement problem.

Chapter 4 (based on the author's work in [47]) proposes a novel approach to quantum imaging by applying the UDW detector model to a traditional quantum ghost imaging setup: we take the object (in one optical arm) and the spatially-resolved measuring device (in the second arm) to both be made up of initially independent arrays of UDW detectors prepared in particular initial states. After coupling these detectors to a scalar field state (which functions as an analogy for the typical down-converted state), evolving the system (**P2**) and finally measuring (**P3**) the state of the detectors, we find that it is possible to model the quantum ghost imaging process using this new QFT-based framework. This opens up the door to, among other things, studying imaging in accelerating frames and curved gravitational backgrounds, for example.

We have discussed **P1** to **P3** above. However, since all of the experiments in the body of this thesis will involve at least two photons, and since **P4** is pertinent to composite systems with two or more degrees of freedom, **P4** silently permeates all of our discussions. It is worth noting, however, that **P4** gives rise to arguably the most fundamental - but strangest - concept behind many observed quantum phenomena: *quantum entanglement*. A composite system is said to be entangled if its density operator (i.e. its quantum state) cannot be written as a tensor product of its individual subsystems' states. An in-depth discussion of entanglement could fill a lengthy book (see [1] for a good introduction), but the concept will nonetheless appear repeatedly in the forthcoming chapters.

We have also touched on another important difference between classical and quantum physics above: the idea of the randomness or, rather, *quantum indeterminacy*, of

measurement outcomes (indeed, this randomness is built into **P3**). Quantum mechanics, and therefore Nature, has uncertainty built into its formalism at a fundamental level: in general situations, even with perfect knowledge (on the part of the experimenter) of a system as well as perfect measurement apparatus, it is impossible to deterministically predict the outcome of any particular measurement. The absolute best that one can calculate is the probability of measuring a certain value for a chosen observable. While perhaps unintuitive at our macroscopic 'classical' scale, this indeterminacy can have important practical applications. In Chapter 5 (based on [48]), we present a novel demonstration of one such application, namely a true quantum random number generator which uses the orbital angular momentum (OAM) degree of freedom of single photons as the source of entropy. Randomness plays an extremely fundamental role in our everyday life, from weather [49, 50] and financial market modelling [51], all the way to cryptography [52]. The use of OAM as a source of entropy is noteworthy in that a well-defined OAM state lies in a countably infinite-dimensional Hilbert space. As such, one can theoretically extract as many bits from a single photon as one wishes, with the limitations being set by the experimental setup (such as its numerical aperture). The protocol which will be demonstrated could also be incorporated into existing randomness generators as an enhancement.

Finally, after the main body of work in Chapters 2 to 5, concluding remarks and ideas for future work are given in Chapter 6.

Chapter 2

Ghost imaging using entanglement-swapped photons

Chapter 2, based on [37], details a new experiment which is the first to exploit entanglement swapping to correlate photons, which are initially completely independent, for use in quantum ghost imaging. This should be contrasted with ordinary ghost imaging (in both the classical and quantum regimes), in which the photons, while eventually propagating and hence becoming spatially separated, originate from the same source/medium and are hence correlated from the beginning of the experiment.

Specifically, given two independent pairs of entangled photons, say A-B and C-D, the novel experiment's combination of a Hong-Ou-Mandel (HOM) filter and a postselection/Bell-state projection scheme for photons B and C creates entanglement between the remaining two photons, A and D, which can then be used in a traditional quantum ghost imaging protocol. The particular choice of postselection event, namely either the presence or absence of photon coincidence events in arms B and C, allows one to tailor either an anti-symmetric or symmetric state, respectively, for photons A and D. While a HOM filter is unitary (and is therefore in spirit with postulate **P2**), as discussed in the introduction, the projective Bell measurement/postselection is not unitary as we essentially use a conditioned state. It hence blurs the line between **P2** and **P3**. However, the conditioned state's symmetry nonetheless has an important bearing on the observed physics. For this experiment, in the anti-symmetric case, the ghost image we observe turns out to be 'contrast reversed' with respect to the original object, while one would measure an 'ordinary contrast' image in the symmetric case. The concept of (anti-)symmetry is tightly linked to those of *(in)distinguishability* and *(non-)identical* particles (see, for example, [53] for a discussion of these concepts). This procedure of using postselection to alter a state's symmetry should be kept in mind

while reading this chapter. Indeed, there is no strong notion in classical physics of state symmetry/(in)distinguishability, since all classical particles are distinguishable.

2.1 Introduction

Information protocols based on photonic states of light are of interest for a number of reasons. For example, the multiple degrees of freedom, such as spatial, frequency, polarisation, and the high-dimensional nature of light all provide access to a large alphabet in which to encode information [54, 55, 56]. The increased information capacity provides the ability to communicate at high data rates and provides mechanisms to test quantum fundamentals [57]. However, an ongoing challenge is the exact generation, precise manipulation, and efficient detection of such states of light.

In the context of quantum networks based on photonic states of light, the challenge is to distribute quantum information over large distances in an efficient manner. At the core of a quantum network is a process known as entanglement swapping, which relies on a Bell-state measurement. Entanglement swapping [58] generates correlations between systems that have not interacted and has been observed in many degrees of freedom, for example, polarisation [59] and orbital angular momentum [60], and it can also be used for the quantum teleportation of multiple degrees of freedom [61]. One protocol that requires correlations is ghost imaging, and while it is now known that ghost imaging only requires correlations in one basis, the implications of entanglement swapping on such a process remain unknown.

The term 'ghost imaging' arose only in 1995 in the context of studying EPR correlations in position and momentum [62]. It was noted that the position correlations of an entangled photon pair generated by means of spontaneous parametric down-conversion (SPDC) could be used in an imaging experiment, as shown in Fig. 2.1(a). In a conventional ghost imaging experiment, the photon in the object arm is detected with a 'bucket' detector with no spatial resolution so that the object information is erased, while the photon in the other arm, which has never interacted with the object, is collected with a spatially-resolved detector. Consequently, when the photons are measured in coincidence, the spatial correlations allow image reconstruction. Since this seminal work, many manifestations of the above have been realised, including the use of thermal light in the classical regime [63, 64, 65], momentum-correlated ghost imaging [66], spiral ghost imaging with orbital angular momentum [67, 68], time domain ghost imaging [69], computational (a technique which only requires bucket detectors) [70, 71, 72] and compressive (which reduces the number of required measurements) ghost

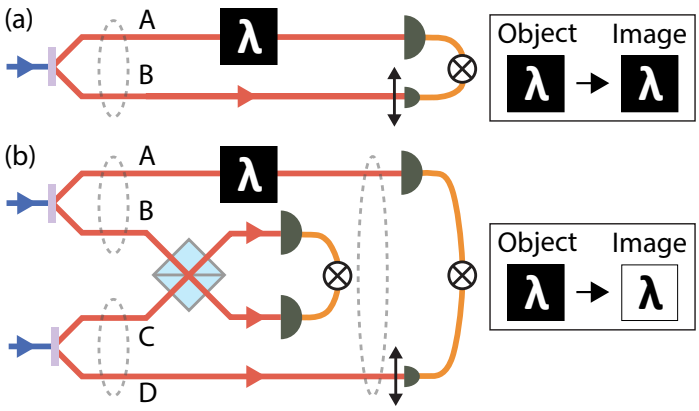

Fig. 2.1 **Two- and four-photon ghost imaging schematics, using entangled photon pairs**. (a) Traditional two-photon ghost imaging using photon pairs generated by parametric down-conversion. By exploiting the quantum correlations between photon A which 'sees' the object but is detected with a bucket detector and photon B, which doesn't see the object but on which we perform spatially-resolved measurements, the object information can be determined. (b) Our four-photon ghost imaging setup showing contrast inversion. In this four-photon case, two pairs of photons are generated in two independent parametric down-conversion processes. The state of the photons A and D become entangled when photons B and C undergo a Bell state measurement. Contrast reversal of the object is observed when photons B and C are projected onto the anti-symmetric state.

imaging [73], as well as the use of nondegenerate SPDC for dual wavelength ghost imaging [74, 75].

In this work we combine the essential tools of quantum networking with high-dimensional quantum states of light and the core principles of ghost imaging. We provide a full theoretical analysis of the observed phenomena and experimental evidence of ghost imaging using two sets of entangled photon pairs. We demonstrate that the spatial state of non-interacting photons that were initially independent, in other words, photons that have never interacted and start with no position or momentum correlations, can be used for ghost imaging. Entanglement swapping is employed to establish the correlations needed to reconstruct a ghost image of an object. In doing so, we demonstrate that the Bell projection required for entanglement swapping plays a crucial role in the ghost imaging outcome: projection onto the set of anti-symmetric states results in contrast inversion whereas a projection onto the set of symmetric states results in conventional ghost imaging, in other words, no contrast inversion. As a consequence, a projection onto all sets simultaneously, both symmetric and anti-symmetric, results in no image at all. This is due to the inability to establish any

spatial correlations between the two independent sources. This work also paves the way for long distance image transfer across a quantum network [76].

2.2 Experimental setup

The experimental setup, depicted in detail in Fig. 2.2, consists of a Ti:sapphire laser at a wavelength of 808nm and a repetition rate of 80MHz. A 0.5-mm-thick BBO crystal is pumped to produce 360mW of upconverted light at 404nm. This light then pumps two BBO crystals, each 1mm thick, to produce down-converted entangled photons, labelled A and B from crystal 1 and C and D from crystal 2. We filter the down-conversion immediately after the crystal using 20-nm bandpass filters centred at 810nm. Additionally, photons B and C are later filtered with 3-nm bandpass filters centred at 808nm to ensure a good HOM dip visibility.

In order to produce correlations between photons A and D, photons B and C are interfered on a beamsplitter. Using a translation stage in the path of photon B, the path lengths of photons B and C can be matched so that they undergo Hong-Ou-Mandel (HOM) interference. This projects their joint state into one of the four two-dimensional Bell states, from which the only anti-symmetric state can be selected by postselecting on four-fold coincidences. An object placed in arm A is experimentally realised using a spatial light modulator (SLM); a second SLM in arm D is used to make measurements using a single-pixel SLM scanning technique. Such SLMs allow us to tailor the spatial structure of the incident paraxial light [77], allowing arbitrary changes in the intensity and phase profiles to be effected. These devices will feature in a number of the forthcoming chapters and the interested reader is hence directed to [78, 79] for detailed explanations of modern spatial light modulation devices and techniques.

The light is collected using single-mode fibres in arms A and D as this results in very few background counts. However, we use multi-mode fibres in arms B and C to ensure that we are collecting as many spatial modes as possible after the interference filter. The light is detected using single-photon avalanche diodes (Excelitas SPCM-800-14-FC) while time tagging and coincidence counting are performed using a Picoquant HydraHarp.

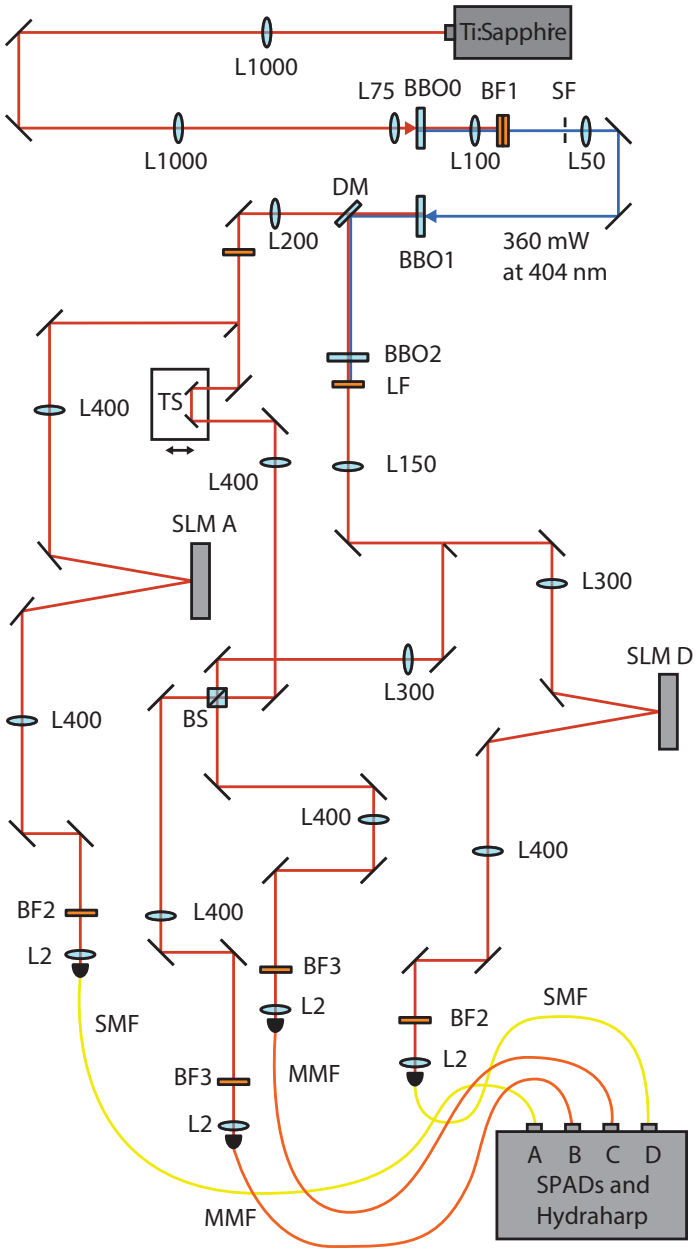

Fig. 2.2 **Detailed experimental setup used to observe four-photon ghost imaging**. The focal lengths of the lenses are marked in millimetres, in other words, L100 corresponds to a lens of focal length 100mm. BBO0: 0.5-mm-thick BBO crystal. BF1: two consecutive bandpass filters at 405 ± 5nm. SF: 100-μm circular aperture. BBO1: 1-mm-thick BBO crystal. DM: dichroic mirror. BBO2: 1-mm-thick BBO crystal. LF: longpass filter, cutoff wavelength 750nm. SLM: spatial light modulator. BF2: bandpass filter at 808 ± 1.5nm. BF3: bandpass filter at 810 ± 10nm. TS: translation stage. BS: non-polarising beamsplitter. SMF: single-mode fibre. MMF: multi-mode fibre. SPAD: single-photon avalanche diode.

2.3 Four-way ghost imaging theory

Consider the simplified four-photon entanglement-swapped ghost imaging setup shown schematically in Fig. 2.1(b). It consists of two independent parametric down-conversion processes that generate two EPR states [66]. Photon pairs A-B and C-D are initially entangled in their spatial degrees of freedom, so the initial four-photon state in the position (i.e. pixel) basis is given by

$$|\varphi\rangle_{ABCD} = \sum_{i=1}^{d} \frac{1}{\sqrt{d}} |r_i\rangle_A |r_i\rangle_B \otimes \sum_{j=1}^{d} \frac{1}{\sqrt{d}} |r_j\rangle_C |r_j\rangle_D, \tag{2.1}$$

where $|r_{i/j}\rangle$ are eigenstates in the pixel basis Hilbert space of dimension d, and $r_{i/j}$ are, respectively, the position vector at the SPDC source for photons A-B/C-D. Note that because the crystal planes are imaged to the SLMs in paths A and D (see Fig. 2.2), these correspond to pixels on SLM A and D, respectively.

We now consider the state of photons in paths B and C, which are incident on a beamsplitter (BS). A coincidence in the two output paths of the BS projects onto the anti-symmetric states; the absence of a coincidence in the two output paths of the BS projects onto the symmetric states [80, 81, 82]. In high dimensions ($d > 2$), there are a number of different orthogonal bases in which we can represent the state. The states that we consider are the Bell-like states $\{|\Psi^{\pm}_{nm}\rangle_{BC}\}$ and $\{|\Phi_n\rangle_{BC}\}$ which, taken together, form a basis: the anti-symmetric states are

$$|\Psi^{-}_{nm}\rangle_{BC} = \frac{1}{\sqrt{2}} \left[|r_n\rangle_B |r_m\rangle_C - |r_m\rangle_B |r_n\rangle_C \right], \tag{2.2}$$

while the symmetric ones are

$$|\Psi^{+}_{nm}\rangle_{BC} = \frac{1}{\sqrt{2}} \left[|r_n\rangle_B |r_m\rangle_C + |r_m\rangle_B |r_n\rangle_C \right], \tag{2.3}$$

$$|\Phi_n\rangle_{BC} = |r_n\rangle_B |r_n\rangle_C, \tag{2.4}$$

with $1 \leq n < m \leq d$. We do not consider the Bell-like states $|\Phi^{\pm}_{nm}\rangle_{BC} = \frac{1}{\sqrt{2}} [|r_n\rangle_B |r_n\rangle_C \pm |r_m\rangle_B |r_m\rangle_C]$ as they are not orthogonal to one another when $d > 2$, for example, $\langle \Phi^{+}_{1,2} | \Phi^{+}_{1,3} \rangle \neq 0$.

If one could perform a perfect joint measurement on photons B and C, the probability of finding the biphoton state to be anti-symmetric is $(d-1)/2d$, whereas the probability is $(d+1)/2d$ for the symmetric case (see Section A.1 of the Appendix for details). Furthermore, projecting exclusively onto any of these three sets ($\{|\Psi^{-}_{nm}\rangle_{BC}\}$, $\{|\Psi^{+}_{nm}\rangle_{BC}\}$

or $\{|\Phi_n\rangle_{BC}\}$) leaves the biphoton state in paths A and D, ρ_{AD}, in a mixture of all possible two-qubit entangled subspaces spanned by the corresponding set [60]. The state is only pure if there are two pixels, $d = 2$ (or only a single two-dimensional subspace is considered).

The transmissive mask object we place in path A, O, is binary. Therefore, the value of pixel i, namely $O(i)$, is either 1 (transmissive) or 0 (opaque) and the set $\{O(i)\}$ hence contains all the information about the object. Finally, $\mathcal{B} = \sum_i O(i)$ is the number of transmissive pixels.

The mathematical calculations detailed in Section A.1 of the Appendix show that the detection of a photon after the mask in path A combined with different projections for the two photons in paths B and C can herald different states for photon D. This is the key to this ghost imaging system: provided that photon A is detected, the state of photon D exhibits contrast reversal or not, with respect to O, depending on the projection choice. The various possible ghost images are given by the sets of intensities $\{I_{\Psi^-}(i)\}, \{I_{\Psi^+}(i)\}, \{I_{\Phi}(i)\}, \{I_{\mathrm{AS}}(i)\}$ and $\{I_{\mathrm{S}}(i)\}$, where each $I(i)$ corresponds to the probability of detecting light at pixel i in path D, given the different projections in paths B-C (AS = anti-symmetric, S = symmetric). By considering the object formation and detection in the pixel basis, we disregard any phase information between the pixels. As such, this is somewhat akin to classical object imaging. However, one could instead use the SLM and single-mode fibres for remote state preparation and then herald a qubit in path B; the implications of this for quantum teleportation are discussed in Section 2.5.

The pixel intensities in each case are given by

$$I_{\Psi^-}(i) = I_{\Psi^+}(i) = \frac{\mathcal{B} - O(i)}{2d^2}, \tag{2.5}$$

$$I_{\Phi}(i) = \frac{O(i)}{d^2}, \tag{2.6}$$

$$I_{\mathrm{AS}}(i) = \frac{\mathcal{B} - O(i)}{2d^2}, \text{ and } I_{\mathrm{S}}(i) = \frac{\mathcal{B} + O(i)}{2d^2}. \tag{2.7}$$

The contrast of the ghost image formed from projections onto either the Ψ^- (Eq. 2.2) or Ψ^+ (Eq. 2.3) Bell-like set of states is clearly reversed with respect to the object, since the binary pixel value of the object $O(i)$ is subtracted from a constant $\mathcal{B}$ for the corresponding ghost image pixel i (Eq. 2.5). In other words, brighter pixels of the object correspond to dimmer pixels in the image, and vice versa. An ordinary contrast ghost image is reconstructed when projecting onto the Φ (Eq. 2.4) set of states

(Eq. 2.6). However, note that the Ψ^- set is the only set of anti-symmetric states in the Bell-like state basis and so projecting onto this set is equivalent to projecting onto any and all anti-symmetric states (I_{AS}). Furthermore, projecting onto symmetric states is equivalent to projecting onto the Ψ^+ and Φ sets. In this case, the combination of pixel intensities results in an ordinary contrast ghost image (I_{S}). As per Appendix Section A.1, one can quantify this contrast by calculating normalised contrast values $\mathcal{C}$, with respect to the initial object, for each of these ghost imaging cases

$$\mathcal{C}_{\Psi^-} = \mathcal{C}_{\Psi^+} = \frac{-1}{\mathcal{B}(d-1)}, \tag{2.8}$$

$$\mathcal{C}_{\Phi} = \frac{1}{\mathcal{B}}, \tag{2.9}$$

$$\mathcal{C}_{\mathrm{AS}} = \frac{-1}{\mathcal{B}(d-1)}, \text{ and } \mathcal{C}_{\mathrm{S}} = \frac{1}{\mathcal{B}(d+1)}. \tag{2.10}$$

Interestingly, it can be seen (from summing together I_{AS} and I_{S}, Eq. 2.7) that if the anti-symmetric and symmetric ghost images are added together, one obtains a uniform pixel intensity value which is independent of any particular pixel i. This is equivalent to one having performed no projection, onto any particular subset of states, in paths B-C and then measuring the ghost image. As one would expect, no image is observed in this case as no correlations would be created between the independent photons A and D, and the resultant state in path D is maximally mixed, i.e. $\rho_{D|\mathrm{AS},A} + \rho_{D|\mathrm{S},A} \propto \mathbb{I}$ (see the Appendix Section A.1).

Theoretical simulations of the predicted ghost images for an initial 'λ' object mask are shown in Fig. 2.3; we see that the image in the anti-symmetric projection and postselection case ($I_{\mathrm{AS}} = I_{\Psi^-}$) exhibits contrast reversal with respect to the object, which is not the case for symmetric projection and postselection. Furthermore, the sum of the anti-symmetric, Fig. 2.3(e) and symmetric, Fig. 2.3(f), images produces a constant image which contains no information.

2.4 Four-way entanglement swapped ghost imaging results

In our experimental realisation (outlined in Section 2.2), after using two BBO crystals to produce two pairs of independent photons, we choose to project the photons in paths B and C onto the set of anti-symmetric states to effect entanglement swapping

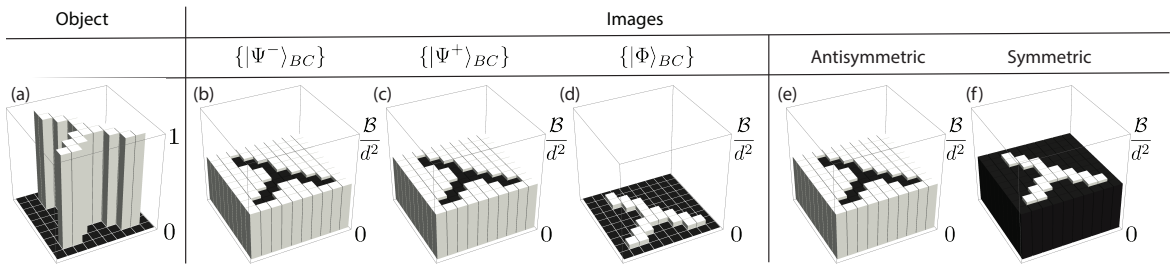

Fig. 2.3 **Predicted ghost images for different projections in paths B-C**. (a) 3D representation of a binary 'λ' object in a $d = 100$-dimensional space (i.e. 100 pixels) with $\mathcal{B} = 20$ pixels 'on'; each pixel transmission value is either 0 or 1. (b)-(f) Simulations of the predicted ghost images, with the height of each pixel representing the pixel intensity/probability of detecting a signal. The anti-symmetric ghost image (e) corresponds with projection onto the $\{|\Psi^-\rangle_{BC}\}$ set (b); the symmetric image (f) corresponds with projecting onto either (or both) the $\{|\Psi^+\rangle_{BC}\}$ set (c) or the $\{|\Phi\rangle_{BC}\}$ set (d).

between the remaining two photons (A and D). As such, I_{AS} in Eq. 2.7 is tested. However, the system is first characterised by using simple two-pixel ($d = 2$) images. The crystal plane is relayed to SLM A and D, at which point photons A and D exhibit strong position correlations. With SLM A masked with a two-pixel hologram (the object), with one half 'on' (pixel value 1) and the other half 'off' (value 0), SLM D is masked with either the same hologram or a contrast-reversed version. By subsequently measuring the number of four-fold coincidences between all four paths as we vary the path length difference (using the translation stage in path B) between paths B and C, we gauge the efficiency of the Hong-Ou-Mandel (HOM) filter.

The results of this test are shown in Fig. 2.4. Indeed, the dip appears when both SLMs are loaded with the same two-pixel mask, while there is no change in the coincidences when the measurement SLM D is instead masked with the contrast-reversed pattern (see the Appendix Section A.2 for further details). The presence of the HOM dip confirms that our system is indeed projecting onto the set of anti-symmetric states. As such, the corresponding two-pixel, four-photon ghost image results are shown in Figs. 2.5(a)-(c), which compares the original object, the simulated ghost image and the experimentally-observed image. Clearly, the ghost image in Fig. 2.5(c) is contrast reversed with respect to the object in Fig. 2.5(a), verifying our earlier predictions. Apart from this first observation of a contrast-reversed image in a four-way ghost imaging protocol, positive and negative images have also been observed algorithmically using thermal light [83, 84], in a quantum interference experiment [85], and simulated using thermal fermions [86].

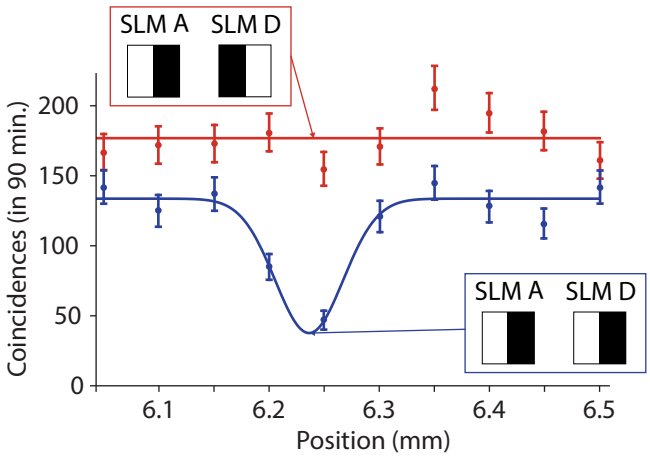

Fig. 2.4 **Hong-Ou-Mandel dip test**. The four-fold coincidence counts are shown as a function of the path B translation stage position for the two cases: either the contrast-reversed (red) or ordinary contrast (blue) two-pixel mask (with respect to the SLM A object) loaded on SLM D. There is no discernible reduction in counts for the contrast-reversed case, while there is the prominent, prototypical HOM dip, with a visibility of 0.56, for the ordinary contrast case.

We repeated the experiment using a 2×2-pixel image ($d = 4$) loaded onto SLM A with a single pixel 'on' and the other three 'off'. SLM D was used to scan through these four pixels, one at a time, to obtain four measurements which were combined to form the ghost image in path D. The results, shown in Figs. 2.5(d)-(f), again show a contrast-reversed image when projecting onto anti-symmetric states in paths B-C, albeit with a lower contrast than the $d = 2$ case. This is in line with Eq. 2.10.

We chose $\mathcal{B} = 1$ (i.e. object masks with only one bright pixel) in an attempt to maximise the ghost image's contrast (see the Appendix Section A.3 for a further discussion on the protocol's inherent efficiency). Indeed, only when $\mathcal{B} = 1$ is the pixel value in the ghost image, which corresponds to the bright pixel in the original object, theoretically equal to zero (see Eq. 2.7). The measured contrasts for the two ghost images are compared with the corresponding contrast predictions in Fig. 2.6. For the $d = 2$ case (Fig. 2.5(c)), we obtain a contrast value of -0.59 ± 0.13; for the $d = 4$ case (Fig. 2.5(f)), a value of -0.19 ± 0.15 (with the errors calculated by assuming Poisson statistics in the measured count rates). This compares favourably with the predicted contrast values of -1.0 and -0.33 respectively. However, the images in Fig. 2.5 are based on the raw data, without any background subtraction applied. After data processing and subtracting the anticipated four-way count accidentals, the measured values become -0.66 ± 0.13 and -0.26 ± 0.14 for the $d = 2$ and $d = 4$ cases respectively, in good agreement with the theory.

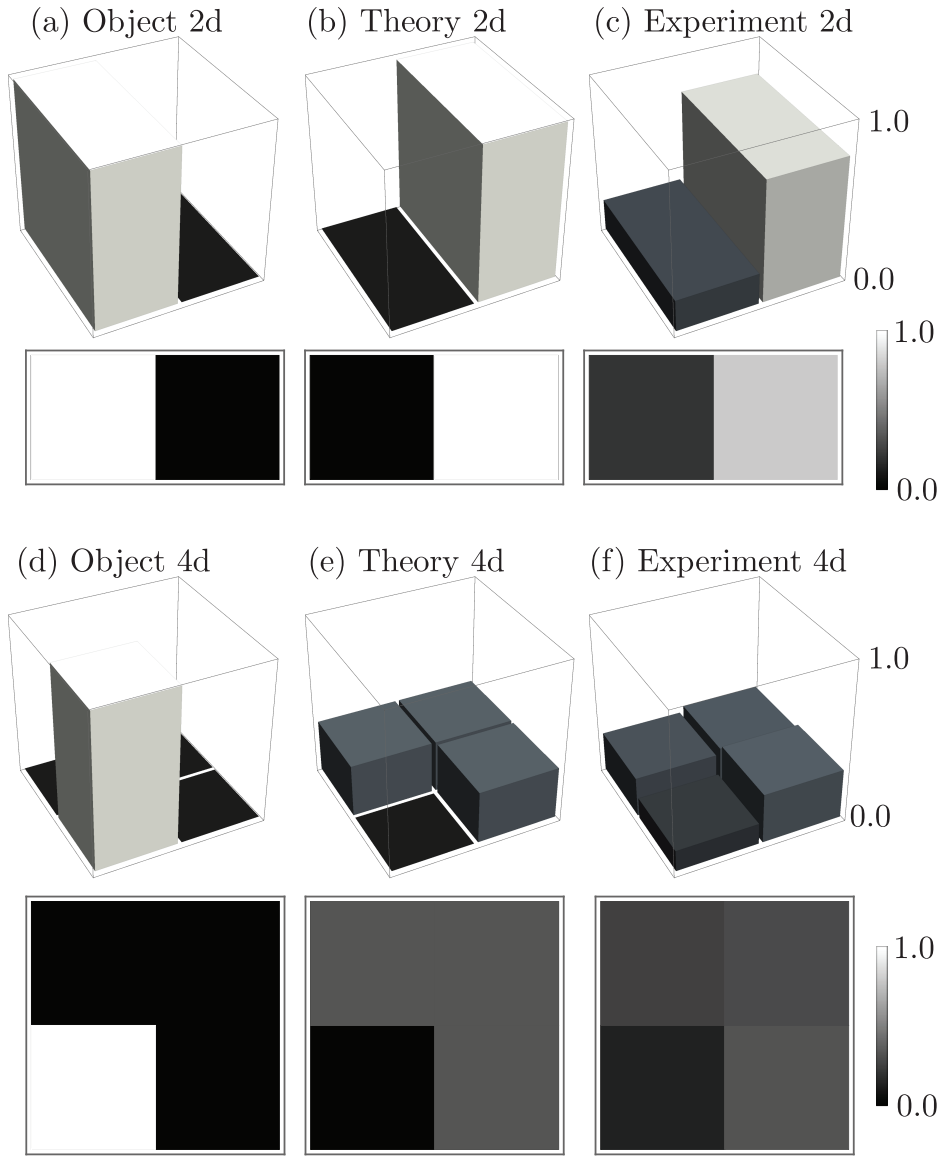

Fig. 2.5 **Contrast-reversed ghost images measured in four-way coincidence with an anti-symmetric HOM projection**. (a)-(c) the $d = 2$ case, and (d)-(f) the $d = 4$ case. The plots are normalised such that the sum of the pixel values is 1. The total four-way counts for the $d = 2$ case were $\{45, 175\}$ counts, over 90 minutes, while they were $\{\{168, 191\}, \{98, 227\}\}$ counts, over 800 minutes, for the $d = 4$ case.

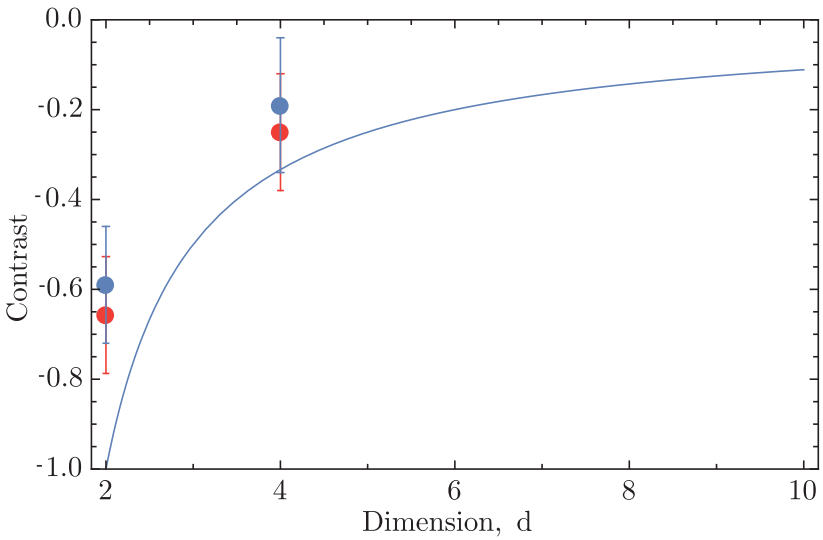

Fig. 2.6 **Ghost image contrast as a function of dimension, d, for anti-symmetric projection**. The data points correspond to the measured contrasts for the data shown in Fig. 2.5, with the error bars found assuming Poissonian noise; the solid line is the theoretical prediction of Eq. 2.10. The blue points are the raw data contrasts; the red points are background-subtracted contrast values.

Finally, it is worth mentioning that the contrasts observed in Fig. 2.5 are so because of the chosen objects, namely with only one pixel 'on'; for higher-resolution objects (d) with more pixels turned on ($\mathcal{B}$), the contrast would be deleteriously affected in line with Eq. 2.10.

2.5 Discussion

In this experiment, we made use of quantum interference and postselection between the independent photons to manipulate the state (**P2** and **P3**) and create correlations. These correlations arise from the quantum nature of light, and information was encoded and measurements performed in only one basis, namely the position basis. However, it is well known that classical correlations are sufficient to perform ghost imaging [64, 65] and therefore the 'classical vs. quantum' ghost imaging question can be applied to our experiment.

Indeed, a classical analogue of our experiment would be of significant interest. Such a realisation would require two independently correlated sources of light and a means to classically correlate two independent modes from said sources. The specific method by which the two modes are classically correlated could then result in a variety of possible ghost images, for example, images that are inverted, rotated, or shifted. It would be

interesting to study the precise nature of such classically correlated images as well as their relative contrasts with respect to the initial object. It should be emphasised, however, that the method used here to correlate the two modes is *quantum* in nature and that there is no obvious classical analogue to projection onto (anti-)symmetric states. Indeed, correlating bright modes in a classical manner is possible, but very different from using quantum interference.

While a form of ghost imaging would be possible with a classical analogue of this experiment, the quantum teleportation of spatial states of light is one facet that is only possible with our system: no classical ghost imaging system is able to perform state teleportation. The implications of our scheme for quantum teleportation are hence of significant interest due to the high-dimensional nature of the spatial states considered here as well as the corresponding restrictions of Bell-state measurements [87]. To simplify our discussion, we first consider the protocol's implications for qubit teleportation and then consider the implications for higher-dimensional qudits.

Quantum teleportation is the teleporting of an unknown, arbitrary quantum state onto a new information carrier (here a photon) in a remote spatial location [1]. An implementation of this only requires three photons, but it is conventional to start with a four-photon system such as the one outlined above. When thinking of our experiment with a view to performing teleportation, a photon in path A is used to herald the presence of a single photon in path B whose state we wish to teleport onto the photon in path D. As always, depending on the outcome of the Bell-state measurement, a unitary operation may be required on the photon in path D in order to recover the teleported state.

However, a significant difference between the ghost imaging and teleportation protocols is that the SLM, which was used to create the classical 'object' in the ghost imaging protocol, is now used in combination with the single-mode fibre to remotely prepare a qubit in the teleportation protocol: given a quantum state $|\psi\rangle = \alpha|0\rangle + \beta|1\rangle$ where α and β are complex probability amplitudes of the pixel basis states, these amplitudes can be set using the SLM. After doing so, the detection of a particular photon mode in path A heralds the presence of the qubit to be teleported in path B.

The data presented in Figs. 2.5(a)-(c) was taken within the context of our ghost imaging protocol. In spite of this context, and as discussed in the previous two paragraphs, the data also holds when metaphorically viewed through a 'quantum teleportation lens' in which the SLM and single-mode fibre in path A are used to remotely prepare a quantum state in path B. Although we only performed the measurements in the pixel basis, further measurements in mutually unbiased bases (for example, the

momentum basis) would be required in order to unequivocally demonstrate quantum teleportation. Nevertheless, our results are consistent with the qubit teleportation of a spatial state of light, and full quantum teleportation of a spatial state qubit would be possible with a simple modification to our existing system: the modified system would require a complete Bell-state measurement rather than a single projective one onto the $\{|\Psi^-\rangle\}$ set. The efficiency of such a scheme would be limited to 1/2 when using linear optics [88]. Such state teleportation has been demonstrated in prior work [60], whereas the emphasis of this work has been on full-field quantum imaging between initially independent photons as well as the impact that manipulating the state symmetry has on the resulting object/image relation (**P2** and **P3**).

Finally, we consider the implications our system has for higher-dimensional qudit teleportation and quantum networks. Indeed, higher-dimensional entanglement itself is proving to be a useful resource in photonics (for further details on this topic, see [89]). The work of Calsamiglia [87] precludes perfect high-dimensional Bell-state measurements using only linear optics: high-dimensional image teleportation can only be achieved using multiple photons in an extended version of the setups in [90, 61], or by implementing nonlinear optical imaging methods such as outlined in [85]. For our system, when photons B and C are projected onto either anti-symmetric ($\{|\Psi^-\rangle\}$) or symmetric ($\{|\Psi^+\rangle, |\Phi\rangle\}$) sets, photons A and D are left in a mixed state of all possible two-dimensional biphoton states spanning the corresponding set. This situation is analogous to the simultaneous two-dimensional entanglement swapping observed in [60]. The state ρ_{AD} is mixed, and hence knowledge of the state of photon A does not give precise knowledge of photon D's state. This results in the contrast reduction seen above for higher-dimensional quantum imaging.

2.6 Conclusion

To conclude, Chapter 2 presents work constituting the first implementation of ghost imaging using initially completely independent information carriers as well as the first observation of ghost imaging using entanglement swapping. We reveal the underlying physics of quantum imaging with non-interacting photons, showing the importance of state symmetry, postselection and object/image dimension on the resultant ghost image. We have also outlined the implications of this experiment for quantum teleportation of spatial states of light. Indeed, our system enables teleportation exactly in two dimensions but the scenario is more complex for higher dimensions. These findings, which we observe in a quantum setting, point to new considerations for traditional

classical ghost imaging whereby new signal processing methods could be developed to enhance and alter the observed images. Finally, this scheme also contains all the features required for a high-dimensional quantum communication network in that quantum imaging, with more than two pixels, could be seen as a form of higher-dimensional communication. Such quantum teleportation and entanglement swapping schemes may become important for such future networks.

Chapter 3

Ghost imaging with engineered quantum states by Hong-Ou-Mandel interference

In Chapter 2 we studied a system in which entanglement swapping was implemented between two independent pairs of entangled photons to create a state which was used to perform quantum ghost imaging. The quantum state was manipulated to adopt a certain symmetry using a HOM filter and postselection. This had important bearings on the ghost images which were observed. While these concepts are interesting, their discussion did take place within the context of a relatively complicated quantum photonics setup. Furthermore, the small number of four-way coincidence counts took hours to collect as a result of the cascade of extremely inefficient nonlinear crystals. The single-pixel scanning technique of the measurement SLM also contributed to the low count rate. Finally, the entanglement swapping protocol relied on postselection which necessitates the discarding of photon detection events (which were already relatively scarce).

In this chapter, which is based on work published in [38], the concepts of state symmetry and postselection will again feature but within the context of a simpler, single entangled pair quantum ghost imaging experiment. Ordinarily, the biphoton state arising from SPDC is symmetric and is the one used in typical quantum ghost imaging experiments. Here, however, both symmetric and anti-symmetric states are considered by tailoring (**P2**) the chosen symmetry using appropriate combinations of Dove prisms and the usual HOM interference filter. A simple proof that the symmetry of a quantum state is independent of the chosen basis is provided, along with a detailed theoretical analysis of all experimental results.

As in Chapter 2, we require projective Bell measurements, in which photon bunching events at the output ports of the HOM filter are discarded, in order to engineer the anti-symmetric state. This is not required in the symmetric case as the down-converted state is symmetric from the beginning and there is hence no need for a HOM filter. However, one still needs to postselect on two-way coincidences in both cases to ensure that only entangled photons (not spurious dark counts), and hence the correct correlations, are included in the results. We show that, interestingly, in the HOM filter/two-way postselection (i.e. anti-symmetric) case, the ghost image observed is a juxtaposition of the original object rotated both clockwise and counterclockwise, while the usual ghost image is measured in the absence of the HOM-beamsplitter combination (i.e. in the symmetric case). Again, the biphoton state's symmetry appears to have an important effect on the observed physics, with these notions having no clear classical analogy. Finally, two different measurement (**P3**) protocols, which are both performed using the SLMs (which allow for the easy, all-digital control of the setup) are tested and compared.

3.1 Introduction

The main ideas behind ghost imaging were introduced in Chapter 2, but we shall recap them here briefly for completeness. First, one creates a pair of correlated photons. Given this, one photon from the pair interacts with an arbitrary object and is collected by a bucket detector with no spatial resolution. The other photon does not interact with the object but is rather sent directly to a spatially-resolved device for measurement. Despite neither photon individually containing any information of the object, a ghost image can be reconstructed when the photons are measured in coincidence due to the initial spatial correlations created within the nonlinear crystal.

The first ghost imaging experiment, by Pittman et al. [62], used quantum entanglement as the source of the correlations between the pair of separate photons (usually arising from the SPDC process [91]). However, other sources of correlations (even classical sources) can be used, with such studies often drawing useful analogies between the classical and quantum regimes [92, 93]. In addition to the studies mentioned in Section 2.1, 3D ghost images have been reconstructed using single-pixel detectors [94], and ghost imaging has even been studied in the presence of atmospheric turbulence [95]. Finally, [37] presented the first demonstration of entanglement-swapped ghost imaging. One should consult [24, 96] for comprehensive reviews of ghost imaging.

Here we demonstrate a form of ghost imaging in which the object and measurement arms are placed after an optional Hong-Ou-Mandel (HOM) interference filter [39]. This allows the quantum imaging to be carried out using either symmetric or anti-symmetric states. Furthermore, we employ spatial light modulators (SLMs) to dynamically control both the object and the imaging process. In particular, we use digitally-controlled holograms in the measurement arm to reconstruct the object without the need for a mechanical scanning system or a spatially-resolved camera. The symmetry selection step of the setup, which includes a pair of Dove prisms and the HOM filter in the anti-symmetric case, results in either the original ghost image or a 'double object' image consisting of the original object rotated both clockwise and counterclockwise.

3.2 Experiment

The experimental setup, shown in Fig. 3.1, is described conceptually here in order to outline the role of each optical element in the forthcoming sections; a more detailed description of the setup can be found in the Appendix Section B.1.

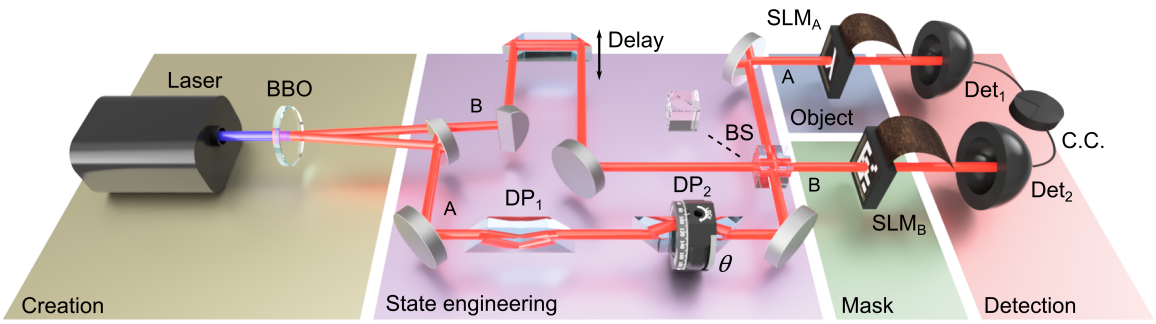

Fig. 3.1 **Experimental HOM ghost imaging setup**. The experiment is divided conceptually into state creation (gold), state engineering (purple), object (blue), measurement (green) and detection (red) steps. BBO: nonlinear crystal; $DP_{1\&2}$: Dove prisms; BS: 50:50 beamsplitter; $SLM_{A\&B}$: spatial light modulators; $Det_{1\&2}$: bucket detectors formed from interference filters, few-mode fibres and avalanche photodiodes; C.C.: coincidence counter.

In the first part of the experiment, an entangled biphoton state is produced by way of a SPDC photon pair source, which gives a state that is completely symmetric. Next, the photon pair passes through a quantum state engineering system made up of Dove prisms (which control the phase of the state's probability amplitudes depending on the orbital angular momentum charge of the photon passing through them) and a HOM interference filter. The latter is used to single out specific states based on their

symmetry. Finally, ghost imaging is performed with the engineered two-photon state using holographic object and measurement mask projections and coincidence counting hardware.

These tools (namely digital projections in the object and image reconstruction steps of the setup) are common in computational ghost imaging [72] and allow us to use only bucket detectors, removing the need for cameras or mechanical scanning systems. Indeed, the chosen binary object, O, is encoded on $\mathrm{SLM_A}$ and the measurement is performed by dynamically modifying the hologram encoded on $\mathrm{SLM_B}$ (the techniques employed here using SLMs are described in detail in [78, 79]). The two different measurement procedures which were investigated, namely a single pixel scan and a random mask scan, are introduced in Section 3.4.1.

3.3 Engineered ghost imaging theory

We first study the biphoton state in the orbital angular momentum (OAM) basis [31]. However, any set of spatial modes which form a basis can be used to express a paraxial mode with an arbitrary spatial profile (two common ones being the Laguerre-Gaussian (LG) or Hermite-Gaussian (HG) modes). It is also evident that any arbitrary state can be written as the sum of a symmetric part and an anti-symmetric part. The effect that a state's symmetry has on, for example, coincidence events in an entanglement experiment has recently been studied in [81], where it was shown how one can control the spatial state's symmetry by exploiting a HOM interferometric measurement [39]. Such techniques work regardless of the chosen spatial basis [97]. In particular, the HOM filter passes only anti-symmetric states when conditioned on two-photon coincidence events, and the symmetry of the input state can be tuned by changing the relative phases between basis states by using two Dove prisms rotated at a judicious angle θ relative to one another.

To begin, consider the state, in the OAM basis, generated by SPDC at the crystal plane

$$|\Psi\rangle = \sum_{\ell} a_{\ell} |\Psi_{\ell}^{+}\rangle, \tag{3.1}$$

where $|\Psi_{\ell}^{\pm}\rangle = \frac{1}{\sqrt{2}} \left(|\ell\rangle_A |-\ell\rangle_B \pm |-\ell\rangle_A |\ell\rangle_B \right)$, $|\ell\rangle$ is an OAM eigenstate with an OAM value of $\hbar\ell$, and a_{ℓ} are the corresponding probability amplitudes (which are determined from a variety of factors such as the down-conversion efficiency, the nonlinear crystal type and size, etc.). With reference to Fig. 3.1, the two Dove prisms, set at a relative

angle θ in path A, have the effect $|\ell\rangle_A \to e^{i2\ell\theta}|\ell\rangle_A$ on a photon passing through them. In this case, Eq. 3.1 transforms as

$$\begin{aligned} |\Psi\rangle &\to \sum_\ell \frac{a_\ell}{\sqrt{2}} \left(|\ell\rangle_A |-\ell\rangle_B e^{i2\ell\theta} + |-\ell\rangle_A |\ell\rangle_B e^{-i2\ell\theta} \right) \\ &= \sum_\ell a_\ell \left(|\Psi_\ell^+\rangle \cos(2\ell\theta) + i|\Psi_\ell^-\rangle \sin(2\ell\theta) \right). \end{aligned} \tag{3.2}$$

Next, note that when the relative angle is set to $\theta = \frac{\pi}{4}$, the only $|\Psi_\ell^+\rangle$ ($|\Psi_\ell^-\rangle$) terms that survive are those with even (odd) ℓ. When this state is then passed through the calibrated HOM filter, only the anti-symmetric modes (i.e. $|\Psi_\ell^-\rangle$, those with odd ℓ values) remain when the system is conditioned on two-way coincidences after the filter [81]. All symmetric states are removed since they don't give rise to coincidences.

One might rightly ask whether such symmetry filtering holds if the state is expressed in any basis other than the OAM basis. Since symmetry is an intrinsic property of a quantum state, a state which is (anti-)symmetric in one basis is (anti-)symmetric in all bases. A proof of this, showing that the symmetry of a quantum state is invariant under a change of basis, is given in the Appendix Section B.2. Therefore, we can express a state in any basis we choose without affecting its symmetry. Furthermore, when considering arbitrary images in which information is encoded in the transverse position of the pixels the image/beam is comprised, the pixels are more easily described using a transverse position vector rather than a combination of OAM-containing modes (such as LG modes). So, it is arguably more intuitive to describe imaging in the position basis (also known as the pixel basis). With this in mind, Eq. 3.1 can be re-expressed as

$$|\Psi\rangle = \sum_{\boldsymbol{r}\in\mathcal{S}} c(\boldsymbol{r}) |\boldsymbol{r}\rangle_A |\boldsymbol{r}\rangle_B, \tag{3.3}$$

where the sum runs over all SLM pixels, a set we call $\mathcal{S}$. We consider this discrete case since the SLM itself consists of discrete pixels. Here $c(\boldsymbol{r})$ is the probability amplitude for photons A and B to be found, in the crystal plane, at the transverse position $\boldsymbol{r} = (x, y)$ (they have the same position since they originate at the same point in the crystal).

Next, the state is manipulated (**P2**) by first passing photon A through two Dove prisms, one of which is rotated at an angle θ with respect to the other. In this case, $R(2\theta) \in \mathrm{SO}(2)$ represents a rotation of the transverse position of photon A (when $\theta = 0$, $R(2\theta) = \mathbb{I}$). From here onwards, we drop the explicit θ dependence for brevity. Note also that paths A and B are assumed to have the same path length unless stated

otherwise. As such, at the BS plane, under the action of the Dove prisms, Eq. 3.3 becomes

$$|\Psi\rangle \rightarrow \sum_{\boldsymbol{r}} c(\boldsymbol{r})|R\boldsymbol{r}\rangle_A|\boldsymbol{r}\rangle_B. \tag{3.4}$$

3.3.1 No HOM filter state

If we remove the BS (and hence the HOM filter) from the setup in Fig. 3.1, the plane where the BS was before is imaged directly onto the SLM. The 'no beamsplitter' state, $|\Psi_{nbs}\rangle$, at the SLM plane is then simply Eq. 3.4, so

$$|\Psi_{nbs}\rangle = \sum_{\boldsymbol{r}} c(\boldsymbol{r})|R\boldsymbol{r}\rangle_A|\boldsymbol{r}\rangle_B. \tag{3.5}$$

Accordingly, a ghost imaging experiment performed using this state is predicted to result in a reconstructed ghost image identical to the original object but rotated by an angle 2θ relative to the object.

3.3.2 HOM filter state

Next, suppose that the BS is not removed from the setup in Fig. 3.1 (i.e. a HOM interference filter is used to combine paths A and B). The well-known action of the BS is

$$|\boldsymbol{r}\rangle_A \rightarrow \frac{1}{\sqrt{2}}\left(|\boldsymbol{r}\rangle_A + |\boldsymbol{r}\rangle_B\right);\ |\boldsymbol{r}\rangle_B \rightarrow \frac{1}{\sqrt{2}}\left(|\boldsymbol{r}\rangle_B - |\boldsymbol{r}\rangle_A\right), \tag{3.6}$$

and as such, the 'beamsplitter' state, $|\Psi_{bs}\rangle$, at the SLM plane is

$$\begin{aligned} |\Psi_{bs}\rangle &= \frac{1}{2}\sum_{\boldsymbol{r}} c(\boldsymbol{r})\left(|R\boldsymbol{r}\rangle_A + |R\boldsymbol{r}\rangle_B\right)\left(|\boldsymbol{r}\rangle_B - |\boldsymbol{r}\rangle_A\right) \\ &= \frac{1}{2}\sum_{\boldsymbol{r}} c(\boldsymbol{r})\left(|R\boldsymbol{r}\rangle_A|\boldsymbol{r}\rangle_B - |\boldsymbol{r}\rangle_A|R\boldsymbol{r}\rangle_B + |R\boldsymbol{r},\boldsymbol{r}\rangle_B - |R\boldsymbol{r},\boldsymbol{r}\rangle_A\right). \end{aligned} \tag{3.7}$$

Postselecting on coincidences between paths A and B has the effect of dropping the latter two terms in Eq. 3.7, so

$$|\Psi_{bs}\rangle = \mathcal{K}\sum_{\boldsymbol{r}} c(\boldsymbol{r})\left(|R\boldsymbol{r}\rangle_A|\boldsymbol{r}\rangle_B - |\boldsymbol{r}\rangle_A|R\boldsymbol{r}\rangle_B\right), \tag{3.8}$$

with $\mathcal{K}$ a normalisation constant.

It is easier to analyse the predicted ghost imaging results if all R dependence in Eq. 3.8 is shifted to either photon A or B completely. In the Appendix Section B.3 we outline how this shift is performed. As a result, Eq. 3.8 is equal to

$$|\Psi_{bs}\rangle = \mathcal{K} \sum_{\boldsymbol{r}} c(\boldsymbol{r}) |\boldsymbol{r}\rangle_A \left(|R^{-1}\boldsymbol{r}\rangle_B - |R\boldsymbol{r}\rangle_B \right). \tag{3.9}$$

It appears that the ghost image in this 'HOM-filter-postselection', and hence anti-symmetric, case will be a juxtaposition of the original object O rotated by an angle of both 2θ and -2θ.

3.3.3 Object reconstruction

Given either state $|\Psi_{nbs}\rangle$ (Eq. 3.5) or $|\Psi_{bs}\rangle$ (Eq. 3.9), the detection section of the experiment is carried out by masking $\mathrm{SLM_A}$ with a binary object O. All information about O is contained in the function $O(\boldsymbol{r})$: $O(\boldsymbol{r}) = 0$ if pixel $\boldsymbol{r}$ in the object is black and 1 if pixel $\boldsymbol{r}$ is white ('black' in practice meaning light incident on pixel $\boldsymbol{r}$ in $\mathrm{SLM_A}$ is not coupled to the detector, and inversely for 'white'). This object masking process is described by $|O\rangle_A = \mathcal{N} \sum_{\boldsymbol{r}} O(\boldsymbol{r}) |\boldsymbol{r}\rangle_A$, with $\mathcal{N}$ the appropriate normalisation. After masking $\mathrm{SLM_A}$ with O (and absorbing $\mathcal{K}$ into $\mathcal{N}$), the state of photon B, in both the absence and presence of the HOM filter, is

$$\langle O|\Psi_{nbs}\rangle = \mathcal{N}^* \sum_{\boldsymbol{r}} c(\boldsymbol{r}) O(R\boldsymbol{r}) |\boldsymbol{r}\rangle_B, \tag{3.10}$$

$$\langle O|\Psi_{bs}\rangle = \mathcal{N}^* \sum_{\boldsymbol{r}} c(\boldsymbol{r}) \left(O(R\boldsymbol{r}) - O(R^{-1}\boldsymbol{r}) \right) |\boldsymbol{r}\rangle_B. \tag{3.11}$$

If we assume that the pump beam is expanded such that its intensity is more or less constant over the object/measurement areas of the SLMs (or, equivalently, assuming a flat-top pump beam), the probability amplitudes c are all constant. The two cases above can then be visualised more clearly

$$\langle O|\Psi_{nbs}\rangle \propto \sum_{\boldsymbol{r}} O(R\boldsymbol{r}) |\boldsymbol{r}\rangle_B, \tag{3.12}$$

$$\langle O|\Psi_{bs}\rangle \propto \sum_{\boldsymbol{r}} \left(O(R\boldsymbol{r}) - O(R^{-1}\boldsymbol{r}) \right) |\boldsymbol{r}\rangle_B, \tag{3.13}$$

where, recall, $R = R(2\theta)$ is a rotation in the plane transverse to the optical axis. The intensity of pixel $|\boldsymbol{r}\rangle_B$ in the reconstructed ghost image in both cases is hence

$$|\langle \boldsymbol{r}|_B \langle O|\Psi_{nbs}\rangle|^2 \propto |O(R\boldsymbol{r})|^2 , \tag{3.14}$$

$$|\langle \boldsymbol{r}|_B \langle O|\Psi_{bs}\rangle|^2 \propto \left|O(R\boldsymbol{r}) - O(R^{-1}\boldsymbol{r})\right|^2 . \tag{3.15}$$

Eqs. 3.14 and 3.15, which are experimentally tested in the following section, align with the earlier predictions, namely that we expect to observe a single rotated ghost image in the symmetric, no HOM filter case of Section 3.3.1 and a juxtaposed 'double' ghost image, with opposite rotations, in the anti-symmetric, HOM filter case of Section 3.3.2.

3.4 Results & discussion

The experimental system is first characterised by measuring the SPDC spiral bandwidth and confirming the symmetry filtering effect of the HOM filter (the gold and purple sections of Fig. 3.1), with the results given in Fig. 3.2. By measuring the coincidence counts within the range $\ell_A, \ell_B \in [-15, 15]$, first without and then with the Dove prisms and beamsplitter, we see that the HOM filter indeed removes the even ℓ values (as discussed below Eq. 3.2) and transmits the odd ones. This is equivalent to only transmitting all of the anti-symmetric $|\Psi_\ell^-\rangle$ Bell states.

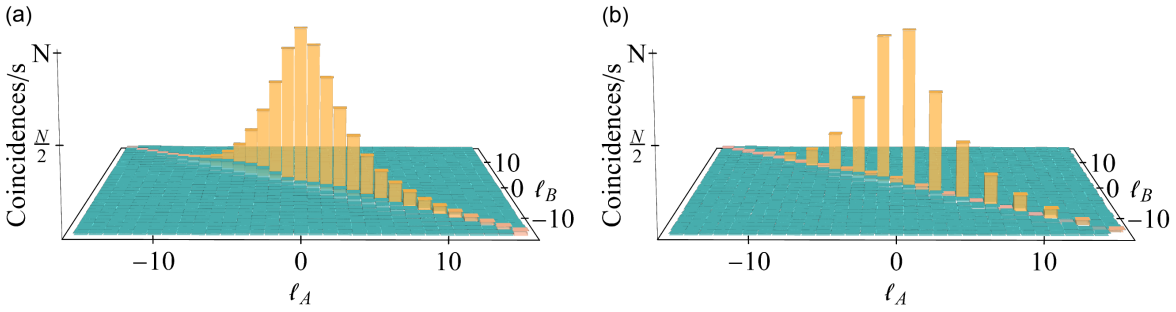

Fig. 3.2 **Spiral bandwidth and HOM filter characterisation**. The system is characterised within the discrete OAM topological charge range $\ell_A, \ell_B \in [-15, 15]$; the coincidence counts are normalised with respect to the maximum value. (a) OAM spiral bandwidth of the SPDC photons without HOM filtering, and (b) the analogous spiral bandwidth after introducing the HOM filter and setting the relative angle between the Dove prisms to $\theta = \frac{\pi}{4}$.

In Section 3.4.1, we investigate standard ghost imaging (without a HOM filter, but with the two Dove prisms) where the object is created and the measurements are dynamically performed using the SLM. The pros and cons of two different measurement

techniques are also discussed. Then, in Section 3.4.2, we investigate the effect that anti-symmetric HOM filtering has on the reconstructed ghost image.

3.4.1 Standard ghost imaging & measurement techniques

First, ghost imaging was performed with the setup of Fig. 3.1 but with the BS removed (i.e. without the HOM filter). In this case the initial state, which is imaged onto the SLM, is symmetric (when $\theta = 0$). $\mathrm{SLM_A}$ was masked with a 960×960-resolution object O (as in Figs. 3.3(a)-(b)) and a digital raster scan performed using $\mathrm{SLM_B}$ (with a 48×48 resolution). The results are shown in Figs. 3.3(c)-(d) for a relative Dove prism angle of $\theta = 0$ and Figs. 3.3(e)-(f) for $\theta = \frac{\pi}{4}$.

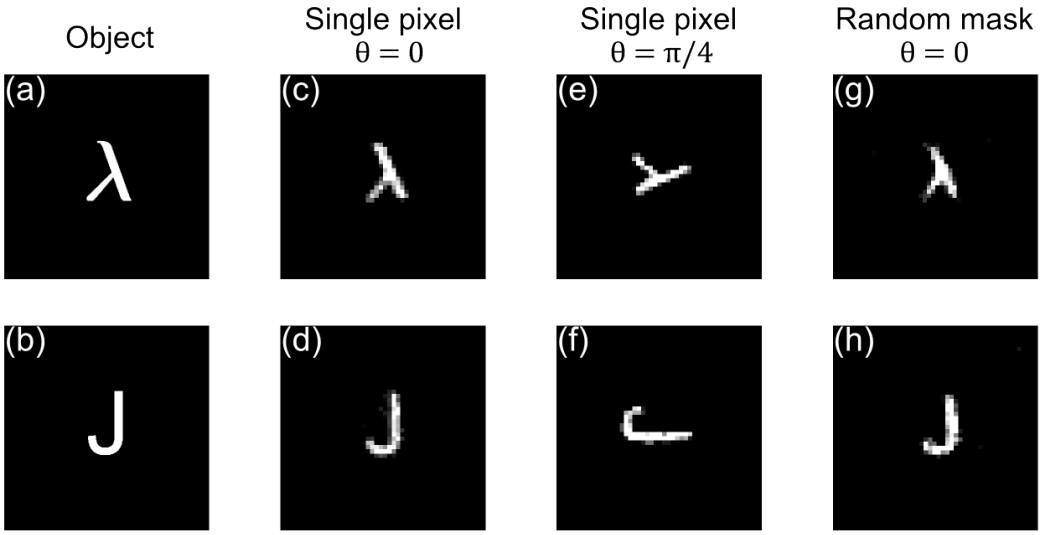

Fig. 3.3 **Standard ghost imaging results without the HOM filter**. (a)-(b) The objects O encoded on $\mathrm{SLM_A}$, with white pixels indicating transmitted photons and black pixels blocked photons. The reconstructed ghost images of the corresponding object, using a single pixel 48×48-resolution scan with $\mathrm{SLM_B}$, are shown in (c)-(d) for a relative Dove prism angle of $\theta = 0$ and (e)-(f) for $\theta = \frac{\pi}{4}$. (g)-(h) show the corresponding ghost images obtained when using the random mask scan technique.

The ghost images of Figs. 3.3(c)-(f) were reconstructed with the set of measured coincidence counts, namely $\{c_i\}$, and the single pixel raster scan technique, using $\mathrm{SLM_B}$, according to

$$\text{Ghost image} = \frac{c_1}{n} P_1 + \frac{c_2}{n} P_2 + \cdots , \tag{3.16}$$

where c_i is the two-photon coincidence count recorded for raster position P_i and n is a normalisation constant (see the Appendix Section B.4 for more details on this and

the random mask technique). The digital single pixel scan reproduces the expected ghost image accurately. However, the scanning resolution (and ultimately that of the ghost image) in this case is limited by the intensity of the biphoton signal at the SLM plane. Most photons incident on the SLM are discarded with this technique and the integration time for each raster position must necessarily increase as the pixel size decreases in order to overcome noise.

As such, a different 'random mask' measurement scheme [98], based on the concept of compressed sensing [99], was also tested. This was done in order to overcome the noise in low signal cases without needing to sacrifice resolution [100]. The theoretical details of the technique are outlined in the Appendix Section B.4 and the experimental results obtained are given in Figs. 3.3(g)-(h). The same 960×960 binary object O is loaded onto $\mathrm{SLM_A}$ as before. However, instead of scanning over every pixel with $\mathrm{SLM_B}$ and recording the corresponding coincidence count value, a set of N 48×48-resolution binary masks, $\{M_i\}$, is first generated. For each mask M_i, each pixel is randomly chosen to be white or black such that the ratio of the total number of black:white pixels is 1:1. Each mask is then loaded, in sequence, onto $\mathrm{SLM_B}$ and the corresponding coincidence count value, c_i, recorded. Finally, with the sets $\{M_i\}$, $\{c_i\}$, for a large enough N, the ghost image is reconstructed by taking a convex sum of the random masks weighted by their corresponding coincidence count value, i.e.

$$\text{Ghost image} \approx \frac{(c_1 - \bar{\boldsymbol{c}})}{n} M_1 + \frac{(c_2 - \bar{\boldsymbol{c}})}{n} M_2 + \cdots , \tag{3.17}$$

where $\bar{\boldsymbol{c}}$, the mean coincidence count value [100], is included to correctly shift the image's pixel values. Experimentally, one notices that the ghost image's sharpness increases with an increase in N. Furthermore, if one were to use masks with a different proportion of black:white pixels, as the number of white pixels decreases, the noise of each image decreases (as does $\bar{\boldsymbol{c}}$), with the extreme case of 1 white pixel being the single pixel scan of Eq. 3.16. However, this results in a concomitant decrease in both the detected signal and the image resolution (for a fixed integration time).

3.4.2 Double ghost images

The random mask measurement protocol was tested, without the HOM filter in the setup, for the objects given in Figs. 3.4(a)-(d) using $N = 4000$ random masks and an integration time of 1s per mask. The results for the $\theta = \frac{\pi}{4}$ case are given in Figs. 3.4(e)-(h) and for $\theta = -\frac{\pi}{8}$ in Figs. 3.4(m)-(p). As in Fig. 3.3, without the HOM filter but in the presence of two Dove prisms, the observed ghost image is the original

object O rotated by an angle of 2θ. While perhaps unsurprising, it is interesting to note how easily one arrives at this conclusion when the theoretical calculation is performed in the pixel basis, as this result may be more obfuscated if the calculations were performed in another higher-dimensional basis (such as the LG modes).

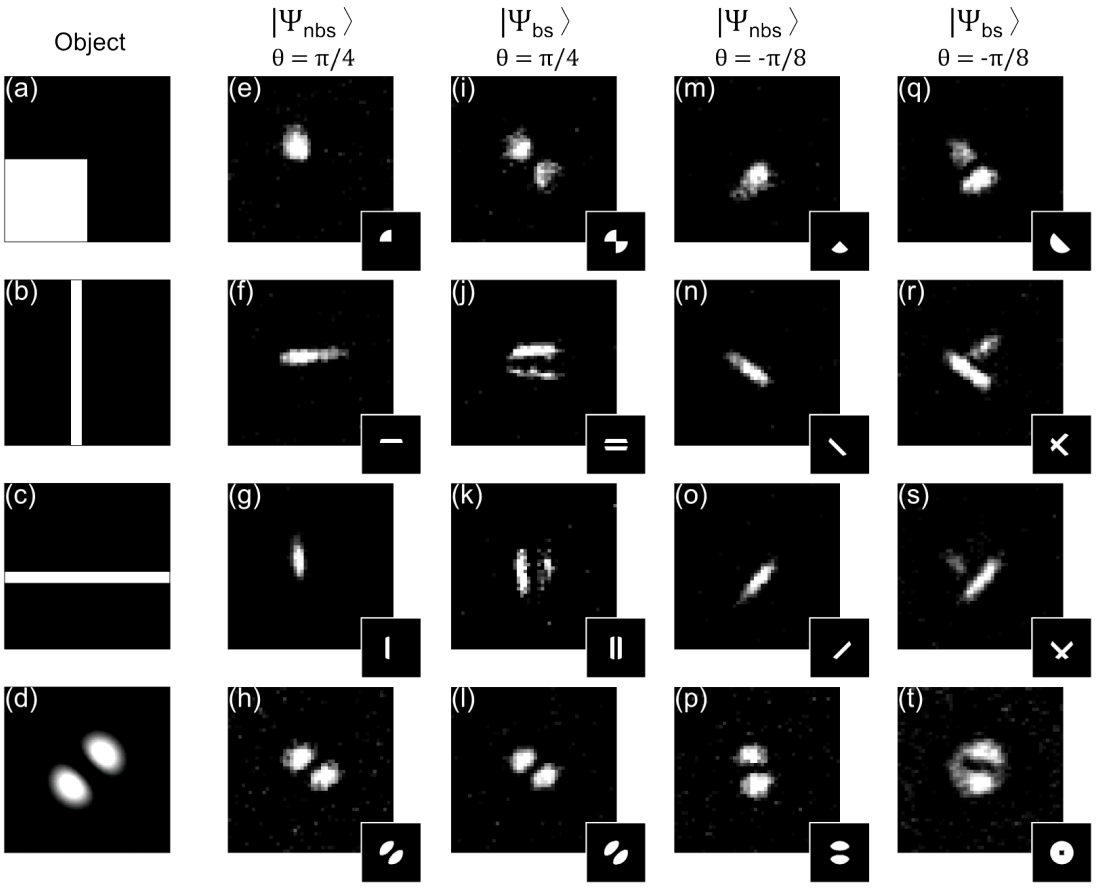

Fig. 3.4 **Ghost imaging, with and without HOM filtering, using the random mask scan technique**. (a)-(d) The objects encoded on $\mathrm{SLM_A}$. In the absence of the HOM filter, the reconstructed ghost images (given the objects in the leftmost column) are given in (e)-(h) for $\theta = \frac{\pi}{4}$ and (m)-(p) for $\theta = -\frac{\pi}{8}$. With the HOM filter, the corresponding ghost images are given in (i)-(l) for the $\theta = \frac{\pi}{4}$ case, and (q)-(t) for the $\theta = -\frac{\pi}{8}$ case, where we clearly see the juxtaposed 'double' ghost image. The insets give simulations of the anticipated results in each case.

The more interesting result is seen once the Dove prisms and HOM filter (which comprises a BS and two length-matched optical paths) are included before the object and measurement sections of Fig. 3.1. Indeed, the non-zero Dove prism angle θ and HOM filter together tailor the $|\Psi_{bs}\rangle$ state, in which case Eq. 3.15 suggests that the reconstructed ghost image, given object O, is a combination of O rotated by both 2θ (R) and -2θ (R^{-1}). This is indeed observed experimentally: Figs. 3.4(i)-(l) give

experimental results for this anti-symmetric ghost imaging for $\theta = \frac{\pi}{4}$, and Figs. 3.4(q)-(t) for $\theta = -\frac{\pi}{8}$. This appears to highlight again the important effect that an input state's symmetry has on a ghost image in particular and quantum optics results in general. Note also that this 'doubling' effect could perhaps be understood as the beamsplitter 'splitting' the image into two and recombining the image information from the two different optical paths. Indeed, when measured in coincidence, a rotated photon A is either transmitted by the beamsplitter and interacts with the object, in which case the unrotated photon B (whose phase is -2θ with respect to photon A) is measured by the detection scheme, or the unrotated photon B is reflected by the beamsplitter and interacts with the object, with the rotated photon A (with a 2θ phase relative to photon B) being measured. Further investigation into the exact bearing that the state's symmetry has on the observed image is hence warranted.

Next, note that for $\theta = \frac{\pi}{4}$ the ghost images in the bottom row of Fig. 3.4 are identical, with or without the HOM filter, and match the corresponding object's intensity profile (save for a superficial rotation). We do not see the 'double' ghost image, since the two juxtaposed halves overlap. This is a result of the invariance of the object under a π rotation. Such a rotational 'invariance' effect could conceivably find application in quantum systems in which one wishes to finely align a setup or ascertain the precise centres of down-converted photons' optical axes.

Finally, the difference in intensity between the two juxtaposed objects in the anti-symmetric images of Figs. 3.4(i)-(l) and (q)-(t) (the anti-clockwise rotated object appears dimmer than the clockwise rotated one) is due to disparities in the losses of each path (different detector efficiencies, slight misalignment in one arm, etc.).

3.5 Conclusion

In Chapter 3 of this thesis, a HOM filter and Dove prisms were used to engineer particular quantum states and investigate their effects in quantum ghost imaging experiments. The results agreed perfectly with the detailed theory in both the usual as well as the anti-symmetric Dove prism-HOM filtering case. In the latter situation, the reconstructed ghost image was a juxtaposition of the original object rotated both clockwise and counterclockwise. As in Chapter 2, the results here highlight the importance that a quantum state's symmetry, as well as the state preparation and postselection processes (**P2** and **P3**), have on the observed physics. However, as always, more studies are needed to understand this all further.

Finally, it is worth mentioning that although such higher-dimensional filtering demonstrations are often understood in terms of the OAM basis, here it was translated to the pixel basis (which is arguably more intuitive when discussing images) given the invariance of a quantum state's symmetry under a change of basis. Furthermore, completely digital devices were employed for fast and convenient image reconstruction.

Chapter 4

Quantum imaging using relativistic detectors

One of the main aspects of tailoring the state in Chapters 2 and 3 was the process of postselection. This is a less than optimal strategy in that it involves conditioning the quantum state on the observance of a specific event (in this case, mutual photon detection events, i.e. coincidence counts) and 'throwing away' all other events. This process of manipulating and then measuring (**P2** and **P3**) the quantum state is repeated many times on an ensemble of photons all prepared in the same state. Ideally, one would love to be able to perfectly glean the quantum state and its statistics in one shot, without having to repeat the measurement process multiple times. However, quantum mechanics generally prevents this and one has to hence perform quantum tomography on an ensemble of identical states [101]. Furthermore, once one has interacted with and 'observed' a quantum state, the wavefunction of the system collapses and the state necessarily changes based on the observed measurement outcome. This, as mentioned earlier, is encapsulated in the measurement problem. Indeed, **P3** doesn't give any specific details as to how exactly our experiments and measurements perturb a quantum system: it simply dictates the potential outcomes' statistics and prescribes the new state conditioned on us having observed a particular measurement outcome. Physicists hence often try to gain information about a quantum system while not (or at least minimally) disturbing said system by using techniques such as coupling ancilla qubits to the system, judicious choices of entanglement witnesses or performing weak measurements [102]. This should all be contrasted with classical physics/computing, where the framework allows us to measure a system without disturbing it. Yet Nature is quantum and is hence described by our four postulates in Section 1.

While very successful in its own right, we know that the brand of quantum mechanics used in typical quantum information and quantum optics studies is ultimately incomplete. Indeed, notions such as different reference frames, particle creation and annihilation, and the confounding effects of acceleration and curved gravitational backgrounds are not accounted for in ordinary quantum mechanics. Quantum field theory (QFT), a set of ideas which treat quantum fields as being fundamental rather than particles [5], can however account for both everything normal quantum mechanics can, as well as these additional phenomena. And while QFT is usually applied to fields such as particle physics, material science and high energy physics, the combination of QFT and quantum information, namely Relativistic Quantum Information (RQI), has proven to be quite fruitful in recent years [41, 42].

Here, in Chapter 4 (which is based on [47]), we change tactics and propose the idea of using the *Unruh-DeWitt detector* model (a popular theoretical RQI model of a detector) to understand the quantum imaging described in the preceding chapters in particular and the quantum measurement/detection process more generally. We first present a quantum field theory version of a SPDC state. This state, coupled to Unruh-DeWitt (UDW) detectors, is used to investigate a single-pixel ghost image under both inertial and non-inertial settings, and a two-pixel image under inertial conditions. The reconstructed images obtained for various possible inputs can be distinguished better than a pure guess and hence it appears the formalism can indeed be used to describe quantum imaging, even between non-inertial frames. Given the explicit interaction Hamiltonian underpinning the model, studies of UDW detectors could shed some light on the measurement problem. We also consider the origin of the correlations between the UDW detectors, which, at least for the presented simulation, don't appear to arise from the usual notion of entanglement.

4.1 Introduction

How to quantitatively describe the process of 'measurement' in quantum physics has vexed scientists for many years: experimental readouts take place on the classical macroscopic scale, yet the active elements of detectors generally operate on the quantum level. "How, then, can one establish a correspondence between the quantum and the familiar classical reality?" [103]. In addition to understanding the detection process in inertial frames, the inevitable rise of quantum-based communication between satellites, for example, heightens the need to understand the effects of non-inertial frames on the behaviour of entanglement and the detection process in practice. Indeed, quantum

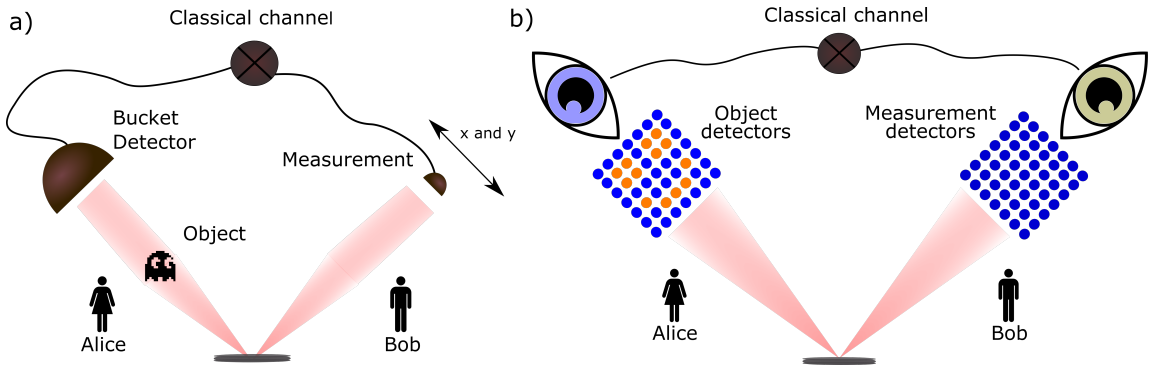

Fig. 4.1 **(a) Typical quantum ghost imaging experiment schematic and (b) our Unruh-DeWitt imaging analogy**.

entanglement does not appear to be Lorentz invariant under acceleration [104], and given that the very notion of a state's particle content (and therefore information content) is frame dependent according to the Unruh effect [43], relativity cannot strictly be ignored.

A popular model of particle detectors which provides such a correspondence was introduced by Unruh and DeWitt [43, 44] and consists of a first-quantised, two-level system (such as a two-level atom or the spin degree of freedom of an electron) coupled to the quantum field to be probed. The Unruh-DeWitt (UDW) detector has since been applied to the interaction between atoms and the electromagnetic field in cavities [105], the Casimir-Polder force [46], as well as in attempts to solve the issue of the non-existence of a position operator in QFT [106], among others.

In a quantum optics laboratory, important experiments such as ghost imaging [24] and observations of Hong-Ou-Mandel filtration [39], as discussed in Chapters 2 and 3, necessitate the detection of time-stamped and/or position-stamped entangled photons. Indeed, after creating a pair of down-converted photons, the 'object' photon needs to be registered by a detector lacking spatial resolution while spatially-resolved measurements are performed on the second photon (see Fig. 4.1(a)). However, such studies do not take into account important physics phenomena, such as special relativity. UDW detectors, which can account for relativity, fit well within the context of quantum optics. Indeed, it can be argued [107] that models of the interaction between light and atoms employed in quantum optics, such as the Jaynes-Cummings model [108, 109], are in fact derivatives of the UDW detector model. Furthermore, optics as a whole appears to be a useful testbed for phenomena occurring in curved classical gravitational backgrounds (for example, analogue Hawking radiation is observed when strong laser pulses are passed through bulk crystals [110, 111]).

In this chapter, Chapter 4, we present a novel way of studying quantum imaging using UDW detectors, with a particular focus on the relatively easily implementable quantum optics experiment presented in the earlier chapters: ghost imaging. Inspired by the binary nature of UDW detectors, this chapter is threefold. First, we briefly present a quantum field theory version of a SPDC state. Second, using this state, we explore the potential of UDW detectors to explain traditional quantum ghost imaging (in an inertial frame) using an analogy: each pixel which makes up the static object, and the pixels of the device used to perform spatially-resolved measurements (**P3**) on the second photon (such as a spatial light modulator [78]), are taken to be separate UDW detectors, as per Fig. 4.1(b). All of these detectors are prepared in a particular initial state representing the object and measurement device, and are coupled to a scalar field in the SPDC state. After the combined system evolves (**P2**) and the field degrees of freedom are traced out, projective measurements are performed on the detectors to accomplish the imaging. Finally, we consider a case in which some UDW detectors are uniformly accelerating and the effect that this acceleration has on the reconstructed ghost image.

4.2 Unruh-DeWitt detector basics

We adopt the conventions of [5], work in $d+1$ dimensional spacetime, and model the electromagnetic field as a scalar field $\hat{\phi}(t,\mathbf{x}) = \hat{\phi}(x)$ in the Dirac picture

$$\hat{\phi}(x) = \int \frac{d^d k}{(2\pi)^d} \frac{1}{\sqrt{2E_{\mathbf{k}}}} \left(\hat{a}_{\mathbf{k}} e^{-ik\cdot x} + \hat{a}^\dagger_{\mathbf{k}} e^{ik\cdot x} \right), \tag{4.1}$$

where the usual relativistic dispersion relation holds

$$E_{\mathbf{k}} = \sqrt{|\mathbf{k}|^2 + m^2}. \tag{4.2}$$

We model a quantum ghost imaging experiment by coupling a system of n Unruh-DeWitt detectors to $\hat{\phi}$. Given an appropriate parameter (the proper time of the laboratory frame, for instance), the worldline X_i^μ of the centre of mass of detector i can be parameterised. Each detector is given a finite spatial 'smearing' profile, $f_i(\mathbf{x})$, to avoid complications arising from regularising point-like detectors; detector i is coupled with $\hat{\phi}$ by way of its monopole moment operator $\hat{Q}_i(t)$ (assuming minimal coupling [46])

$$\hat{Q}_i(t) = e^{i\Omega_i t} |e\rangle_i\langle g|_i + e^{-i\Omega_i t} |g\rangle_i\langle e|_i, \tag{4.3}$$

where $|g\rangle_i$ and $|e\rangle_i$ represent the ground and excited state, respectively, of detector i and Ω_i is the energy gap between the two levels. Detector i's temporal behaviour (i.e. how it is switched 'on' and 'off') is given by the switching function $\varepsilon_i(t)$ (in real-world detectors, such as avalanche photodiodes, this switching function would be a square or saw wave function) and is coupled to $\hat{\phi}$ with coupling strength λ_i. The system's dynamics is then fully described by the interaction part of the Hamiltonian

$$\hat{H}^{\text{int}}(t) = \sum_{i=1}^{n} \hat{H}_i^{\text{int}}(t), \tag{4.4}$$

where

$$\hat{H}_i^{\text{int}}(t) = \lambda_i \varepsilon_i(t) \hat{Q}_i(t) \int d^d x f_i(\mathbf{x} - \mathbf{X}_i(t)) \hat{\phi}(x). \tag{4.5}$$

Next, denote the initial state of the n detectors by $|\mathbf{D}\rangle$ and let $|\mathbf{\Phi}\rangle$ be the initial state of the scalar field $\hat{\phi}$. Assuming the detectors and the field to be initially uncoupled, namely $|\Psi(t_0)\rangle = |\mathbf{D}\rangle \otimes |\mathbf{\Phi}\rangle$ at some reference time t_0, the evolution of the system to $|\Psi(t)\rangle = \hat{U}(t, t_0)|\Psi(t_0)\rangle$ at time $t > t_0$ is determined by the *Dyson operator*

$$\hat{U}(t, t_0) = \mathcal{T} \exp\left(-i \int_{t_0}^{t} \hat{H}^{\text{int}}(t') dt'\right), \tag{4.6}$$

with $\mathcal{T}$ the *time-ordering* operator. Compare all of this with **P2**: the unitary operator appearing in Eq. 4.6, which can be found by solving the Schrödinger equation with a time-dependent Hamiltonian, is precisely what determines the system's evolution. **P2**, however, doesn't give the exact form of U. It is instead given by the specific laws and dynamics we use to model the physics, which in this case is the UDW detector interaction Hamiltonian $\hat{H}^{\text{int}}$, which in turn uniquely determines $\hat{U}$.

Next, without loss of generality, let $t_0 \to -\infty$ and $t \to \infty$, since all time dependence can be accommodated by suitably modifying the switching functions ε_j. Hence

$$\hat{U} = \mathcal{T} \exp\left(-i \sum_{j=1}^{n} \int d^d x dt \lambda_j \varepsilon_j(t) \hat{Q}_j(t) f_j(\mathbf{x} - \mathbf{X}_j(t)) \hat{\phi}(x)\right). \tag{4.7}$$

Evolving the detector-field system according to this $\hat{U}$, the state of the detectors at time τ can be found by tracing out the field, i.e.

$$\rho_D(\tau) = \text{Tr}_\phi \left[|\Psi(\tau)\rangle\langle\Psi(\tau)|\right]. \tag{4.8}$$

The challenge of finding $|\Psi(\tau)\rangle$ is complicated by the presence of the time-ordering operator $\mathcal{T}$. In [112], the authors compute $\hat{U}$ perturbatively up to second order, with arbitrary switching functions $\varepsilon_j(t)$, in their study of entanglement harvesting using two UDW detectors. In [113], however, a non-perturbative analysis of entanglement harvesting is performed by choosing Dirac-delta switching functions so that the detectors couple with the scalar field at a discrete instant of time. Practically, this choice of switching function is a realistic assumption in the current imaging context given that the best modern photodetectors, such as superconducting nanowire single-photon detectors [114], have gating times on the order of picoseconds (so detectors separated by millimetres lie outside each others' light cones). We will hence adopt a non-perturbative approach.

4.3 Non-perturbative expression for $\hat{U}$

Assume all detectors couple to the field at time instant τ, so that $\varepsilon_j(t) = \delta(t-\tau)$. This allows us to factorise $\hat{U}$ into components acting on each detector individually using the Baker-Campbell-Hausdorff formula [115]

$$\hat{U} = \exp\left(\sum_{j=1}^{n} \hat{Q}_j(\tau) \otimes \hat{Y}_j(\tau)\right) = \prod_{j=1}^{n} \exp\left(\hat{Q}_j(\tau) \otimes \hat{Y}_j(\tau)\right), \tag{4.9}$$

where

$$\hat{Y}_j(\tau) = -i\lambda_j \int d^d p \left(F_j(\mathbf{p}, X_j(\tau))\hat{a}^\dagger_{\mathbf{p}} + \text{c.c.}\right), \tag{4.10}$$

$$F_j(\mathbf{p}, X_j(\tau)) = \frac{\tilde{f}_j(\mathbf{p})}{(2\pi)^d\sqrt{2E_{\mathbf{p}}}} e^{i(E_{\mathbf{p}}\tau - \mathbf{p}\cdot\mathbf{x}_j(\tau))}, \tag{4.11}$$

with $\tilde{f}_j$ the Fourier transform of f_j. The operator $\hat{Q}_j(\tau)$ is an involution (i.e. $\hat{Q}_j^2(\tau) = \hat{\mathbf{1}}_j$), and hence each exponential factor in Eq. 4.9 can be expressed in terms of hyperbolic functions using their Taylor series expansions

$$\exp\left(\hat{Q}_j(\tau) \otimes \hat{Y}_j(\tau)\right) = \hat{\mathbf{1}}_j \otimes \cosh\left(\hat{Y}_j(\tau)\right) + \hat{Q}_j(\tau) \otimes \sinh\left(\hat{Y}_j(\tau)\right). \tag{4.12}$$

Next, defining $\hat{X}^{i_s}_{j_s}(\tau) = \frac{1}{2}\left(e^{\hat{Y}_{j_s}(\tau)} + i_s e^{-\hat{Y}_{j_s}(\tau)}\right)$ and

$$\hat{\delta}_{j_s}^{i_s}(\tau) = \begin{cases} \hat{\mathbf{1}}_{j_s} & \text{if } i_s = 1, \\ \hat{Q}_{j_s}(\tau) & \text{if } i_s = -1, \end{cases} \tag{4.13}$$

Eq. 4.12 can be recast as

$$\exp\left(\hat{Q}_j(\tau) \otimes \hat{Y}_j(\tau)\right) = \sum_{i_s \in \{-1,1\}} \left(\hat{\delta}_j^{i_s}(\tau) \otimes \hat{X}_j^{i_s}(\tau)\right). \tag{4.14}$$

Suppressing the τ dependence from here onward and using Eq. 4.14 to rewrite Eq. 4.9 gives an exact expression for the time-evolution operator

$$\hat{U} = \sum_{\bar{j} \in \{-1,1\}^n} \hat{\delta}_1^{j_1} \otimes \hat{\delta}_2^{j_2} \cdots \hat{\delta}_n^{j_n} \otimes \hat{X}_{(\bar{j})}, \tag{4.15}$$

where $\hat{X}_{(\bar{j})} = \prod_{m=1}^{n} \hat{X}_m^{j_m}$, with $\bar{j} = (j_1, j_2, \cdots, j_n) \in \{-1, 1\}^n$. Finally, since all the $\hat{Y}_j$ operators commute (they all act on the scalar field at the same time), $\hat{X}_{(\bar{j})}$ can be expressed as

$$\hat{X}_{(\bar{j})} = \frac{1}{2^n} \sum_{\bar{k} \in \{-1,1\}^n} \tilde{\delta}_{j_1,k_1} \tilde{\delta}_{j_2,k_2} \cdots \tilde{\delta}_{j_n,k_n} e^{\sum_{t=1}^{n} k_t \hat{Y}_t}, \tag{4.16}$$

where

$$\tilde{\delta}_{j_s,k_s} = \begin{cases} 1 & \text{if } k_s = 1, \\ j_s & \text{if } k_s = -1. \end{cases} \tag{4.17}$$

4.4 SPDC state model

To create an entangled photon state in typical quantum optics experiments, a coherent source of light, such as a laser, is directed onto a nonlinear crystal. This results in an indeterminate number of pairs of entangled photons by the process of spontaneous parametric down-conversion (SPDC). To model such a situation, we begin with the following quantum field theory version of a coherent state parameterised by a coherent amplitude $\alpha(\mathbf{q})$ [55, 113]

$$|\alpha(\mathbf{q})\rangle \equiv \hat{D}_{\alpha(\mathbf{q})}|0\rangle := \exp\left(\int d^d q \left[\alpha(\mathbf{q})\hat{a}_{\mathbf{q}}^\dagger - \alpha^*(\mathbf{q})\hat{a}_{\mathbf{q}}\right]\right)|0\rangle, \tag{4.18}$$

where $\hat{D}$ is the optical phase space displacement operator. A pump photon with momentum $\mathbf{q}$ from the coherent state has some probability of creating a pair of photons

with momenta $\mathbf{p}$ and $\mathbf{k}$. This probability, along with the nature of the entanglement between the two output photons, is encapsulated in the quantity $\chi(\mathbf{p},\mathbf{k};\mathbf{q})$. This process is modelled by making the replacement

$$\hat{a}^\dagger_{\mathbf{q}} \to \int d^dp d^dk \chi(\mathbf{p},\mathbf{k};\mathbf{q})\hat{a}^\dagger_{\mathbf{p}}\hat{a}^\dagger_{\mathbf{k}}, \tag{4.19}$$

in Eq. 4.18. Note that this substitution necessarily involves postselecting on the photons which undergo the down-conversion process. And finally, we define $\hat{J}$ such that our SPDC state is

$$e^{\hat{J}}|0\rangle := \exp\left(\int d^dq d^dp d^dk \left[\alpha(\mathbf{q})\chi(\mathbf{p},\mathbf{k};\mathbf{q})\hat{a}^\dagger_{\mathbf{p}}\hat{a}^\dagger_{\mathbf{k}} - \text{c.c.}\right]\right)|0\rangle. \tag{4.20}$$

Some comments are in order. First, Eq. 4.20 is invariant under exchange of the two photons, so $\chi(\mathbf{p},\mathbf{k};\mathbf{q}) = \chi(\mathbf{k},\mathbf{p};\mathbf{q})$ (the state describing down-conversion is symmetric). It also does not account for the annihilation of the pump photon, as Eq. 4.19 merely creates two photons. This is known as the *semiclassical approximation* and is applicable given the extreme inefficiency of the SPDC process in practice. Finally, it is worth mentioning that since SPDC does not occur in a vacuum but in a nonlinear crystal, Lorentz symmetry is consequently broken. Hence all our results need to be interpreted from a chosen reference frame (here the laboratory frame).

4.5 Ghost imaging scheme

Let $|\Psi(t_0)\rangle = |\mathbf{D}\rangle \otimes |\mathbf{\Phi}\rangle$, with $|\mathbf{\Phi}\rangle = e^{\hat{J}}|0\rangle$, be the initial state of the detector-field system. Evolving the system and tracing out the field degrees of freedom at some time $t > \tau$ gives the density matrix of the detectors

$$\begin{aligned}\rho_D &= \text{Tr}_\phi\left(\hat{U}|\Psi(t_0)\rangle\langle\Psi(t_0)|\hat{U}^\dagger\right) \\ &= \sum_{\bar{j},\bar{l}} \hat{\delta}^{j_1}_1 \cdots \hat{\delta}^{j_n}_n |\mathbf{D}\rangle\langle\mathbf{D}| \hat{\delta}^{l_1}_1 \cdots \hat{\delta}^{l_n}_n \mathscr{G}(\bar{l},\bar{j}),\end{aligned} \tag{4.21}$$

with $\mathscr{G}(\bar{l},\bar{j}) = \langle 0|e^{-\hat{J}}\hat{X}^\dagger_{(\bar{l})}\hat{X}_{(\bar{j})}e^{\hat{J}}|0\rangle$. Now, using the definitions from the preceding sections, it can easily be seen that $\mathscr{G}$ can be recast in the following form

$$\mathscr{G}(\bar{l},\bar{j}) = \frac{1}{2^{2n}} \sum_{\bar{k},\bar{m}\in\{-1,1\}^n} \left(\prod_{s,v=1}^{n} \tilde{\delta}_{l_v,m_v} \tilde{\delta}_{j_s,k_s} \times \langle 0|e^{-\hat{J}} e^{\sum_t (k_t-m_t)\hat{Y}_t} e^{\hat{J}}|0\rangle \right). \tag{4.22}$$

Next, a braided corollary of the BCH formula, namely

$$e^{\hat{A}} e^{\hat{B}} e^{-\hat{A}} = \exp\left(\sum_{k=0}^{\infty} \frac{1}{k!} \underbrace{[\hat{A},[\hat{A},[\cdots,[\hat{A}}_{k},\hat{B}]]\cdots]] \right), \tag{4.23}$$

allows $e^{-\hat{J}} e^{\sum_t (k_t-m_t)\hat{Y}_t} e^{\hat{J}}$ to be expressed in terms of nested commutators of the operators $\hat{J}$ and $\sum_t (k_t - m_t)\hat{Y}_t$. Although the exponent in Eq. 4.23 does not terminate in this case, a helpful pattern for the even k and odd k terms does emerge, giving

$$\begin{aligned} e^{-\hat{J}} e^{\sum_t (k_t-m_t)\hat{Y}_t} e^{\hat{J}} = \exp\Bigg[-i \int d^d p_0 d^d p ([F(\mathbf{p}_0)(\delta^{(d)}(\mathbf{p}_0 - \mathbf{p}) + K_e(\mathbf{p}_0,\mathbf{p})) \\ + F^*(\mathbf{p}_0)(\mathbb{X}(\mathbf{p}_0,\mathbf{p}) + K_o(\mathbf{p}_0,\mathbf{p}))]\hat{a}^\dagger_{\mathbf{p}} + \text{c.c.}) \Bigg], \end{aligned} \tag{4.24}$$

with $F(\mathbf{p}) = \sum_t (k_t - m_t)\lambda_t F_t(\mathbf{p}, X_t(\tau))$, $\mathbb{X}(\mathbf{p}_1,\mathbf{p}_2) = 2(2\pi)^d \int d^d q \alpha(\mathbf{q}) \chi(\mathbf{p}_1,\mathbf{p}_2;\mathbf{q})$, and

$$K_e(\mathbf{p}_0,\mathbf{p}) = \sum_{\substack{k=2,\\ k \text{ even}}} \frac{1}{k!} \int d^d p_1 \cdots d^d p_{k-1} \mathbb{X}^*(\mathbf{p}_0,\mathbf{p}_1)\mathbb{X}(\mathbf{p}_1,\mathbf{p}_2)\cdots\mathbb{X}(\mathbf{p}_{k-1},\mathbf{p}), \tag{4.25}$$

$$K_o(\mathbf{p}_0,\mathbf{p}) = \sum_{\substack{k=3,\\ k \text{ odd}}} \frac{1}{k!} \int d^d p_1 \cdots d^d p_{k-1} \mathbb{X}(\mathbf{p}_0,\mathbf{p}_1)\mathbb{X}^*(\mathbf{p}_1,\mathbf{p}_2)\cdots\mathbb{X}(\mathbf{p}_{k-1},\mathbf{p}). \tag{4.26}$$

Finally, Eq. 4.24 clearly has the form of the displacement operator $\hat{D}$ in Eq. 4.18, parameterised now by the coherent amplitude $\beta(\mathbf{p})$ where

$$\beta(\mathbf{p}) = -i \int d^d p_0 \left[F(\mathbf{p}_0)(\delta^{(d)}(\mathbf{p}_0 - \mathbf{p}) + K_e(\mathbf{p}_0,\mathbf{p})) + F^*(\mathbf{p}_0)(\mathbb{X}(\mathbf{p}_0,\mathbf{p}) + K_o(\mathbf{p}_0,\mathbf{p})) \right]. \tag{4.27}$$

As such, the argument in Appendix A of [113] follows verbatim, which allows us to greatly simplify the vacuum expectation value of the Eq. 4.24 operator, with β as per Eq. 4.27, as

$$\langle 0|e^{-\hat{J}}e^{\sum_t (k_t - m_t)\hat{Y}_t}e^{\hat{J}}|0\rangle = \exp\left(-\frac{1}{2}\int d^d p\,|\beta(\mathbf{p})|^2\right), \tag{4.28}$$

so that, finally, we have

$$\mathscr{G}(\bar{l},\bar{j}) = \frac{1}{2^{2n}}\sum_{\bar{k},\bar{m}\in\{-1,1\}^n}\left(\prod_{s,v=1}^{n}\tilde{\delta}_{l_v,m_v}\tilde{\delta}_{j_s,k_s}\times\exp\left(-\frac{1}{2}\int d^d p\,|\beta(\mathbf{p})|^2\right)\right). \tag{4.29}$$

It is somewhat difficult to glean an intuitive understanding of the detectors' density matrix from this general formula; the numerical simulations in forthcoming sections do shed some light on its behaviour. But, as a sanity check, it can easily be seen that ρ_D satisfies the properties of a density matrix. The quantities χ and α can freely be chosen to model specific dynamics of the SPDC process, and are given a detailed treatment in many works (such as [116]). A laser beam's angular spectrum, $\alpha(\mathbf{q})$, is typically described by a Gaussian distribution. However, if the length scales in an experiment are much larger than the wavelength of the laser, the plane wave approximation is apt. In this case, α can be taken to be a Dirac-delta distribution, $\alpha(\mathbf{q}) = \delta^{(d)}(\mathbf{q} - \mathbf{p}_p)$ for some known constant $\mathbf{p}_p$, namely the momentum vector of the monochromatic photons emanating from the coherent pump source. We make this assumption here for ease of calculation. Furthermore, assuming a perfect phase-matching condition in the nonlinear crystal in which perfect momentum conservation occurs, we can choose $\chi(\mathbf{p}_1,\mathbf{p}_2;\mathbf{q}) = \delta^{(d)}(\mathbf{p}_1 + \mathbf{p}_2 - \mathbf{q})$. Given all of this, β simplifies to a much easier expression

$$\beta(\mathbf{p}) = -i\left(F(\mathbf{p})\cosh(2(2\pi)^d) + F^*(\mathbf{p}_p - \mathbf{p})\sinh(2(2\pi)^d)\right). \tag{4.30}$$

Finally, note that the perfect momentum conservation condition forces the total photon momentum in the plane transverse to the optical axis of the pump photons, namely transverse to $\mathbf{p}_p$, to be zero. In other words, if a photon passes through point x_T in the transverse plane, the other one passes through point $-x_T$. This is indeed what is typically observed in practice.

4.5.1 Two detector inertial ghost imaging

Here we work through a two detector ghost imaging example. Suppose that we have two parties, Alice and Bob, who are each given a detector, labelled 1 and 2 respectively. Suppose that Alice prepares her detector in the excited state $|e\rangle_1$. This is interpreted

as representing a binary image consisting of a single white 'on' pixel. Bob, without loss of generality, prepares his detector in the ground state $|g\rangle_2$. If the detectors are judiciously arranged in space and if at time τ a photon from the SPDC state interacts with Alice's detector, given the perfect momentum conservation discussed earlier, there is a reasonable chance that the other photon interacted with Bob's detector (although this is definitely not certain, since the vacuum excitation probability of any detector alone is non-zero).

Next, a postselection scheme is adopted in which Alice postselects on the ground state of her detector. For this simple two detector example, if we were to adopt the perhaps more intuitive scheme entailing Alice postselecting on 'seeing a change' in the state of her detector, it can easily be shown that Bob would be unable to ascertain whether Alice had chosen a white or black pixel. After postselecting, Alice communicates the result to Bob via a classical channel: if she measures the ground state for her detector, she instructs Bob to measure his detector and keep the result; if she observes the excited state, Alice and Bob discard their detectors. Either way, they then reprepare the initial state $|e\rangle_1|g\rangle_2$ and run the experiment again. By repeating this experiment multiple times, Bob can infer the probability of Alice having chosen either the ground ('off' pixel) or excited ('on' pixel) state. So, with $|\mathbf{D}\rangle = |e\rangle_1|g\rangle_2$, the state at some time $t > \tau$ is

$$\rho_{D,AB} = \sum_{j_1,j_2,l_1,l_2} \hat{\delta}_1^{j_1}\hat{\delta}_2^{j_2}|e\rangle_1|g\rangle_2\langle e|_1\langle g|_2\hat{\delta}_1^{l_1}\hat{\delta}_2^{l_2}\mathscr{G}(l_1,l_2;j_1,j_2). \tag{4.31}$$

Alice postselects on $|g\rangle_1\langle g|_1$ and communicates her result to Bob, whose state is obtained after tracing out Alice's detector after postselection

$$\begin{aligned}\rho_{D,B} &= \mathcal{K}\,\mathrm{Tr}_A\left[\rho_{D,AB}|g\rangle_1\langle g|_1\right] \\ &= \mathcal{K}\sum_{j_2,l_2}\hat{\delta}_2^{j_2}|g\rangle_2\langle g|_2\hat{\delta}_2^{l_2}\mathscr{G}(-1,l_2;-1,j_2),\end{aligned} \tag{4.32}$$

with $\mathcal{K}$ such that $\mathrm{Tr}(\rho_{D,B}) = 1$. With this state, Bob can reconstruct the ghost image by taking a convex sum of the two possible detector states, with the weightings being the probabilities themselves, i.e.

$$\text{Ghost image} = P(g_2)\cdot\blacksquare + P(e_2)\cdot\square, \tag{4.33}$$

where $P(g_2)/P(e_2)$ is the probability of Bob observing his detector in the ground/excited state given Alice's postselection scheme. Assuming that Alice prepares one of the two

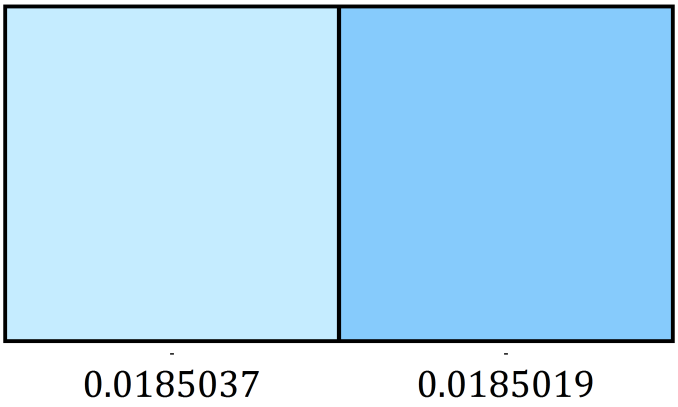

Fig. 4.2 **Numerical simulation of the two possible single-pixel ghost images**. The false-colour images, with the pixel intensities given below them, are rescaled for clarity. Bob measures the left pixel intensity value if Alice initially prepares her detector in the ground state and the right pixel intensity if she prepares the excited state. These images were simulated with the parameters given in the Appendix Section C.1, Table C.1.

initial detector states (and not a superposition of detector states), it is only crucial that the grey level of the resultant single-pixel ghost image in one case differs from that in the other case: a 'brighter' ghost image pixel will correspond with one possibility and a 'darker' pixel the other.

Fig. 4.2 gives a numerical simulation of the two reconstructed, rescaled ghost images Bob could obtain in this case. The pixel intensity indeed differs between the two possible outcomes. So if, for example, Bob reconstructs an image with a pixel intensity corresponding to the right pixel in Fig. 4.2, he can conclude, better than a guess, that Alice chose the excited 'on' pixel as her original object. It hence appears that this formalism can indeed be used to explain quantum imaging within the framework of QFT. This potentially unlocks many field theoretical techniques with which to understand quantum photonics.

Admittedly, the contrast between the two possible ghost images, although well within the numerical error tolerance, is low. This can partly be chalked up to the Dirac-delta coupling between the detectors and the initial field state. Studying the present scheme in the perturbative regime, with switching functions of compact support but with a non-zero measure, would prove interesting since it is likely one would see an increase in the contrast given such finite switching functions with larger supports.

On a more general note, it is as yet unclear how to satisfactorily define an entanglement measure for systems of higher dimension. In the current 2×2 dimensional case

however, a measure such as the negativity $\mathcal{N}$ of a state [117] can be used to investigate the nature of the correlations between Alice and Bob's detectors. $\mathcal{N}$ is defined as

$$\mathcal{N}(\rho_{AB}) = -\sum_i \min(\lambda_i^{T_B}, 0), \tag{4.34}$$

where $\lambda_i^{T_B}$ are the eigenvalues of $\rho_{AB}^{T_B}$, which in turn is the partial transpose of ρ_{AB} with respect to subsystem B. In other words, $\mathcal{N}$ is the absolute value of the sum of the negative eigenvalues of $\rho_{AB}^{T_B}$ (and is 0 if it has none). Now, it has been proven that $\mathcal{N}$ is zero iff the state ρ_{AB} is separable (i.e. not entangled). Interestingly, the negativity of the state in Eq. 4.31 is 0 (given the same parameters used in Fig. 4.2). There is, however, a clear correlation between Alice's initial chosen state and the ghost image pixel in Fig. 4.2. This raises interesting questions as to the source of this correlation. First, it is certainly true that improving this UDW imaging model by using better choices for α, χ, and the switching function (which amounts to choosing a more experimentally realistic pump beam profile and/or phase matching condition) could give rise to a non-zero negativity and stronger correlations between the detectors. However, it is also well known that separability alone is not sufficient to ensure the absence of *quantum* correlations in a state; quantum correlations can be present in mixed, separable states. This is a phenomenon described by the notion of *quantum discord*, $\mathcal{D}(\rho)$ [118]. Discord, which is the difference between two quantum analogues of classical mutual information, can intuitively be thought of as the total correlations present in a bipartite system ρ_{AB} (as measured by the quantum mutual information $\mathcal{I}(\rho_{AB})$) less a quantity $\mathcal{C}_B(\rho_{AB})$ which represents the classical correlations obtained by finding an optimal von Neumann measurement on subsystem B [119] (note that one could instead choose subsystem A, which then in general gives a different value due to the nonsymmetric nature of $\mathcal{C}$). $\mathcal{D}$ is hence a measure of the total 'quantumness' of the correlations, not only those correlations strictly due to entanglement. Although computing $\mathcal{D}$ is highly nontrivial in general, the state in Eq. 4.31 belongs to the subclass of so-called two-qubit 'X' states for which a simple algorithm for finding the discord exists [120]. Applying said algorithm gives $\mathcal{I}(\rho) = 3.5 \times 10^{-7}$ and $\mathcal{C}_B(\rho) = 2.2 \times 10^{-12}$. Since $\mathcal{D}(\rho) = \mathcal{I}(\rho) - \mathcal{C}_B(\rho) \gg \mathcal{C}_B(\rho)$ in this instance, the correlations between Alice and Bob's detectors are, for all intents and purposes, completely quantum in nature. Although it is possible to demonstrate ghost imaging using only classical correlations [63], the quantumness of the correlations here opens the possibility of further studies exploring ghost imaging between spacelike-separated detectors. However, it is worth emphasising that the total correlations between Alice and Bob's detectors, namely

$\mathcal{I}(\rho)$, is still quite small. As mentioned, we anticipate that the correlations could be increased by instead considering switching functions with larger supports or different α, χ functions, for example.

4.5.2 Four detector inertial ghost imaging

In the two detector simulation from the previous section, the information content of the ghost object Alice initially encodes in her single detector is 1 bit. This exactly equals the information bandwidth of the classical channel Alice uses to message Bob (to tell him whether he should keep his measurement or discard it, depending on what she observes). To demonstrate quantum ghost imaging using this model with an object containing more than 1 bit of information yet still employing the 1-bit channel, assume that Alice and Bob are now each given a pair of detectors. Alice's detectors are labelled 1 and 2, Bob's 3 and 4. Suppose that Alice prepares her detectors in the state $|e\rangle_1|g\rangle_2$, namely a two-pixel binary object with pixel 1 'on' and pixel 2 'off'. Bob, without loss of generality, prepares both of his detectors in their ground states. Given the same postselection scheme for Alice as the previous two-pixel case, and having Bob measure his conditioned detectors' state to determine the statistics, the reconstructed ghost image is given by

$$\text{Ghost image} = P(g_3, g_4)\cdot\blacksquare\blacksquare + P(g_3, e_4)\cdot\blacksquare\square + P(e_3, g_4)\cdot\square\blacksquare + P(e_3, e_4)\cdot\square\square. \quad (4.35)$$

Fig. 4.3 gives a numerical simulation of the two-pixel image Bob reconstructs given Alice's initial 'excited-ground' ghost object. As before, our UDW model appears capable of describing ghost imaging within the more complete framework of QFT. The new image contains more information than the classical channel's bandwidth. It should be noted that the contrast between the pixels of the ghost images Bob could recreate decreases markedly as the pixel number increases. This was also the case for the experimental results for the anti-symmetric four-photon ghost imaging demonstration from Chapter 2.

4.6 Non-inertial ghost imaging

Finally, we consider a single-pixel ghost imaging simulation in which one of the parties is accelerating. It is known that non-inertial motion has a nontrivial effect on entanglement [121, 122]. Therefore, if Alice's detector (i.e. the single-pixel object)

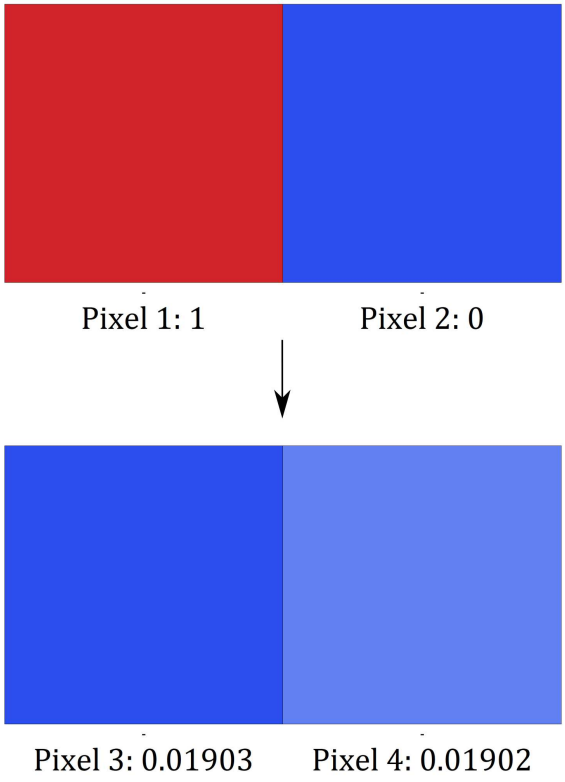

Fig. 4.3 **Numerical simulation of the two-pixel ghost image Bob reconstructs**. The false-colour, scaled ghost image that Bob observes (bottom), assuming Alice initially prepares a 'white-black' image (top). The parameters employed in this simulation are given in the Appendix Section C.1, Table C.2.

were uniformly accelerating instead of remaining stationary with respect to the chosen laboratory reference frame, the correlations between Alice and Bob's detectors, and hence the ghost image Bob reconstructs, would be affected. Furthermore, the ghost image will by affected by the time instant τ at which the detectors couple to the scalar field. While commonplace quantum optics cannot account for such a non-inertial situation, the framework of QFT, and by extension the current UDW scheme, can.

Assume the same two-pixel situation as before, with Bob's detector stationary with respect to the laboratory frame. Alice's detector, on the other hand, is now uniformly accelerating in the x direction with a constant proper acceleration a. It is furthermore given an initial speed such that it is temporarily at rest when $\tau = 0$ (at this instant this situation corresponds to Fig. 4.2, when Alice's detector is the same distance from the optical axis as Bob's). The coordinates of Alice's detector, measured with respect to the laboratory frame and denoted by (T, X, Y, Z), are then given by the well-known Rindler coordinates [123]

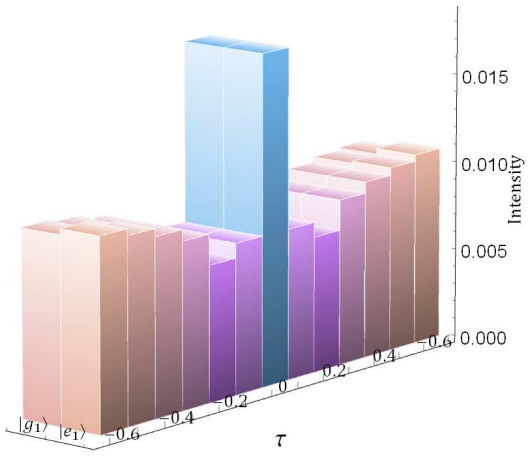

Fig. 4.4 **Non-inertial ghost imaging simulation**. The bars represent the ghost image pixel intensities Bob observes for various detector-field coupling instants τ (for Dirac-delta coupling at τ) and assuming that Alice initially prepares her detector in either its ground or excited state. The parameters employed are given in the Appendix Section C.1, Table C.3.

$$T = x\sinh(at), X = x\cosh(at), Y = y, Z = z, \tag{4.36}$$

where $x = \frac{1}{a}$. Fig. 4.4 gives a simulation of the ghost image pixel intensities Bob would measure (as a function of a sample of possible detector-field coupling instants τ), if Alice initially prepares either the off (ground) or on (excited) detector state.

A contrast between the two possible single-pixel ghost images (which is proportional to the difference in intensity values) in Fig. 4.4, although small, does exist. Therefore, again, it appears that the scheme presented here can describe ghost imaging (and, by extension, spatially-resolved detection in other quantum photonics experiments) between non-inertial frames. However, note the more prominent difference between the intensities for larger values of τ. This is somewhat strange and unexpected. Indeed, one would intuitively expect the contrast to increase as $|\tau|$ decreases since a photon passing through the point x_T in the plane transverse to the pump's optical axis (which is where Bob's detector lies at $\tau = 0$) is correlated with a photon passing through point $-x_T$ (where Alice's detector lies at $\tau = 0$). As such, this model certainly warrants further improvement and investigation: this counterintuitive behaviour may merely be a relic of the particular parameters chosen for the numerical simulation, or may be a more general phenomenon. To isolate the cause, one could choose, as the initial detector state, a suitably 'pre-entangled' one. This would eliminate any complications which may be

arising from the model of the SPDC state in Eq. 4.20. And, as before, performing these calculations in the perturbative regime with more general well-behaved switching functions would be worthwhile too.

4.7 Discussion & conclusion

In this chapter, we have presented a novel theoretical model of the quantum imaging process in quantum optics using a more complete framework of quantum mechanics, namely quantum field theory. First, a QFT version of an entangled down-converted state was introduced. Next, a scheme whereby sets of Unruh-DeWitt detectors (which function as analogues of both the original ghost object as well as the spatially-resolved measuring device) couple to the entangled SPDC state to be probed. This detector-field coupling takes place according to the usual Unruh-DeWitt interaction Hamiltonian, and after the system is allowed to evolve (**P2**), the experimenters measure the detectors. The information gained from the detectors, along with a classical 1-bit channel, demonstrate ghost imaging (one could possibly conceive of different experiments in which one wishes to glean information about the scalar field itself instead). Given the explicitness of the Hamiltonians used in this process (although different models of UDW Hamiltonians are possible [124]), one could hence argue that the Unruh-DeWitt detector model may shed some light on how exactly the experimenter's measurements interact with, or disturb, the quantum system (**P3**).

The SPDC field state presented in Section 4.4 is quite general: only the semiclassical approximation was made, which is widely used in practice. Furthermore, the state is clearly normalisable, which simplifies computations. Previous studies have usually concentrated on harvesting entanglement from the vacuum, but it could be argued that the vacuum state is more often the exception rather than the norm in the laboratory. Further developing the model for an entangled, nonempty state may prove fruitful. Even so, this SPDC field state results in a relatively unwieldy solution for the density matrix of Alice and Bob's detectors once the scalar field is traced out. Furthermore, although convenient mathematically, the assumption of a Dirac-delta switching function in the interaction Hamiltonian is somewhat idealistic: most photon counting modules employed in the laboratory have gating profiles resembling square or saw wave functions. Therefore, a switching function which couples the detectors to the field over a longer period of time may increase the correlations between the detectors and consequently the contrast between ghost image pixels. Such an analysis would need to be perturbative in nature.

The scheme was simulated and confirmed in both single-pixel and two-pixel inertial settings in Figs. 4.2 and 4.3 respectively. In the former case, we found that, interestingly, the negativity of the postselected state between Alice and Bob was 0, implying a lack of entanglement between the parties. The reason for this needs further investigation, especially given that the non-zero value for the quantum discord arises entirely from correlations which are quantum in nature. Despite this, Bob could still infer, better than a simple guess, the state Alice initially prepared in both cases.

Our model was also applied to a non-inertial case with one uniformly accelerating detector. In this situation, the contrast between the different potential ghost image pixels turned out to be non-zero, but still extremely small (smaller than the inertial cases). Although the amount of entanglement harvested from the quantum vacuum, by detectors coupled to it, is very small [125], one would anticipate observing a larger contrast in this 'non-vacuum' case. Our model hence needs to be improved upon if it is to ever be used in practice. However, there are many reasons for physicists to focus on further understanding quantum information in non-inertial and nontrivial gravitational background situations. For one, quantum ghost imaging could be seen as a form of quantum communication (the message being the ghost image itself) and the relaying of quantum information via satellites is becoming a reality [126]. Finally, it would be interesting to consider imaging in nontrivial backgrounds. For example, higher-dimensional quantum communication protocols often focus on the orbital angular momentum (OAM) degree of freedom of photons to encode information [127], and strong gravitational fields (for example, rotating black holes) alter the OAM spectrum of nearby photons [128].

Lastly, it is worth making a comment about how this model relates to the measurement problem. While the outcomes of experimental quantum measurements obey the four postulates, one can define an interaction Hamiltonians akin to Eq. 4.5 within a simpler framework traditionally used in quantum optics. However, given that we know Nature to be relativistic, it makes sense to try to understand the measurement problem within the more complete QFT framework. Indeed, although it has yet to be definitively observed experimentally, the Unruh effect [43] posits that a particle detector accelerating through a vacuum will find its surroundings to be a thermal bath of particles, whereas an inertial detector would measure only the vacuum. If mere non-inertial motion has an effect on what we measure, it stands to reason that a relativistic framework is needed to describe the specifics of the measurement process itself. However, such effects would admittedly only become prominent at accelerations orders of magnitude larger than those encountered in common laboratory settings.

Chapter 5

Holographically controlled random numbers from entangled twisted photons

Another important aspect of quantum mechanics hinted at in previous chapters is the inherent indeterminacy, or randomness, which is built into the formalism. This should be contrasted with classical mechanics in which all particles and objects are distinguishable and in which all solutions to classical equations of motion give completely deterministic answers. Indeed, even the interpretations of the central solutions to the classical equations of motion differ from their quantum analogues. Consider Newton's Second Law, $\mathbf{F} = m\mathbf{a}$. The quantity usually solved for, namely the acceleration vector $\mathbf{a}$, is a quantity we can directly measure and has a very intuitive, everyday interpretation. Furthermore, if we have perfect knowledge of the system (such as the mass m of the classical object in question, perfect understanding of all forces $\mathbf{F}$ acting on the object, the object's initial state, etc.), solving the equation of motion tells us exactly where the object will be, how much energy it will possess, and so on, for all time. In other words, we gain perfect, deterministic knowledge of the system by solving its equation of motion.

However, the quantum case is very different. The object usually sought after when solving quantum mechanics' equation of motion (the Schrödinger equation) is the wavefunction Ψ. This complex function does not have an intuitive, clean interpretation analogous to acceleration or any other physical quantity. Indeed, one cannot directly observe a quantum system's wavefunction. Instead, observables are extracted from Ψ by applying certain operations to it. Furthermore, the wavefunction can never give a deterministic answer as to what to expect when measuring a chosen observable

of a system. Even with perfect knowledge of the wavefunction (which contains all information of the system), the absolute best one can gain is a probability distribution for said system's observables; one can never make 100% certain predictions of what one will observe when measuring a system, only the chances of observing a certain outcome. Indeed, this is precisely encapsulated in **P3**.

This wildly different, unintuitive interpretation of quantum mechanics, as well as the inbuilt randomness, are part of the reason for its strangeness and reputation as being a difficult subject to master. However, this also brings with it important theoretical and philosophical questions as well as exciting technologies not possible with classical mechanics.

In the final chapter of this thesis (which is based on [48]), we will exploit the randomness of quantum mechanics by demonstrating a quantum random number generator (QRNG) which uses the random outcomes of projective measurements performed on quantum superposition states of photons. Multiplexed holograms (encoded on SLMs) are used to spatially map down-converted photons into different optical paths. This gives one full digital control of the mapping process, which we can tailor to theoretically achieve any desired probability distribution by dynamically changing the system's entropy while maintaining the indeterminacy. Furthermore, this method can also be used to account for any bias or imperfections within the transmission and detection systems, allowing one to mitigate the need for time-consuming and perhaps inefficient unbiasing algorithms. After characterising and testing the setup using the path information degree of freedom, the same process is extended to realise a QRNG based on photons' orbital angular momentum (OAM) degree of freedom. The QRNG achieved a min-entropy of $H_{\min} = 0.999 \pm 0.001$ bits per photon (with the theoretical maximum being 1) in the two-dimensional case and passed the NIST battery of randomness tests. The scheme was repeated in a three-dimensional case whereby we observed a min-entropy value of $H_{\min} = 1.577 \pm 0.001$ bits per photon (with the perfect value being 1.585). This all demonstrates the potential of generating true random numbers from the OAM degree of freedom, which in turn opens up access to a novel higher-dimensional Hilbert space from which one can extract multiple random bits per photon.

5.1 Introduction

Our intuition around randomness is often flawed. For example, one would think that if one were to generate a great deal of elements from a truly random source, no patterns

in the generated data would emerge. According to Ramsey theory [129], however, this is not the case: ideal randomness in huge data sets, in which no conceivable patterns in the data exist, is impossible. This, for example, is why ancient cultures assigned meaning to the various arbitrary constellations of the night sky. In part due to our sometimes faulty understanding, studies into randomness continue to remain interesting. Furthermore, random numbers and the closely related concept of entropy are of fundamental importance in areas such as cryptography [8, 7, 130], numerical simulations and Monte-Carlo integration [131, 132], weather [49, 50] and financial market [51] modelling, as well as the computer game and gambling industries [133]. Their importance is difficult to overstate.

Historically and traditionally, random number generation (RNG) has been dominated by mathematically complex algorithms that, given a so-called seed, produce a sequence of bits displaying statistically pseudorandom properties [134]. However, if an attacker gains access to the ultimately deterministic algorithm as well as the seed, all security is lost. Therefore, RNG has undergone a fundamental shift towards focusing on truly unpredictable, indeterministic processes from which to extract entropy. Indeed, understanding the process behind the unpredictability is of fundamental importance: the initial randomness an arbitrary system displays may in fact simply stem from an incomplete knowledge of said system or a limitation of the formalism [135, 136]. In addition, a flawed (and perhaps malicious), seemingly chaotic, but ultimately deterministic RN generator can theoretically output bit strings reminiscent of truly random ones.

This being the case, the inherent indeterminism of quantum physics provides an important source of entropy which can be used to create quantum random number generators (QRNGs) [137]. Within this set of devices, two subcategories of QRNGs exist. One is the trusted-device QRNG, in which a relatively simple but fixed system outputs RNs at a generally high rate and low cost. However, trusted-device QRNGs indeed assume their namesake, namely that one has full confidence in the device and its manufacturer. On the other hand, the second subcategory is the device-independent 'self-testing' QRNG in which the quantum randomness is verified using an entanglement witness or nonlocal Bell inequality violation. Such devices, however, are often extremely inefficient and require initial true random seeds [26].

What is certain, however, is that most QRNGs arise from the field of optics. Indeed, studies focusing on optical parametric oscillators [138], spontaneous Raman scattering [139], amplified spontaneous emission [140, 141], laser phase noise [142] and quantum vacuum fluctuations [143], among many others, have all been considered as appropriate

sources of entropy. Random bit sequences are also often extracted from the Poissonian statistics intrinsic to the photon emission and detection processes [144, 145, 146, 147] (see [148] for a review of RNGs based on these and other optical sources). Furthermore, in the quantum photonics subfield, some nonlocal (even potentially spacelike separated) correlations between entangled photon pairs also display intrinsic random properties [149, 25], such as correlations in polarisation [150], photon arrival times [151], path branching [152] and photon number states [153].

Although these protocols are efficient at generating high quality unpredictable bits, limitations still exist. First, optical transmission and detection systems have experimental imperfections in the equipment, setup, etc., which introduce unwanted, detrimental bias in the generated bits. Even a small bias gravely affects the randomness of a string. To counter this, post-processing algorithms exist which attempt to balance the overall ratio of 0's to 1's (from von Neumann's simple pairwise grouping and discarding protocol [134] to more complex ones [154]). However, post-processing debiasing protocols can limit the RN generation rate (often by sacrificing bits), while pre-detection debiasing often does not (although it may limit a protocol's clock speed). A system which hence allows for the dynamic control of the bias during the generation process - without compromising the 'quantumness' of the protocol - would be beneficial. In fact, unbalancing the ratios of 0's to 1's in a bit string can have some important cryptographic applications [155, 156]. The protocol which will be presented here is such a system.

Second, almost all early optical QRNGs extracted only one random bit for each photon detection event, such as when considering the path or polarisation degree of freedom, for example. These single bit generation schemes, combined with the commonplace but extremely inefficient single and entangled photon sources (chiefly nonlinear crystals), resulted in suboptimal RN generation speeds. Improvements have since been made by employing more efficient sources and equipment. However, another way of upping a system's speed is by considering degrees of freedom lying in higher-dimensional Hilbert spaces. For example, drawing randomness from the positions of arrival photons [157] and single-qubit quantum walks [158] are two such higher-dimensional techniques. Our protocol instead introduces the novel use of the orbital angular momentum (OAM) degree of freedom as a viable source of entropy, given OAMs success in other higher-dimensional demonstrations. Indeed, quantum information processing in photonics using higher-dimensional entanglement between OAM-carrying qudits, rather than the usual binary qubits, is increasing in popularity (see [89, 159] for overviews).

In particular, this chapter first demonstrates a path-branching RNG setup in which, in place of the archetypal beamsplitter, a spatial light modulator (SLM) is employed. The SLM, in a totally probabilistic fashion, directs an incident photon from a spontaneous parametric down-conversion pair down one of two optical paths (with the second photon simply heralding the first). The SLM allows for full digital control over the holograms and by extension, the probability of the incident photon choosing either path. One can hence create and remove bias 'on the fly' by scaling the digital SLM hologram. The theoretical details and experimental results will be fully outlined.

Next, the potential of using biphoton states entangled in their OAM degree of freedom is considered. By probabilistically projecting the incident photon down an OAM-dependent path, one is able to generate sufficiently random bits for various OAM combinations. The same SLM debiasing techniques are available in this OAM case which allows us to tailor (**P2** and **P3**) the probability distribution after having initially measured the down-converted pair's spiral bandwidth. The generation of random bits from OAM is demonstrated in a two- and three-dimensional case, and the observed entropy compares extremely favourably with the maximum possible min-entropy value. This shows the potential of using OAM, a theoretically countably infinite degree of freedom, to generate multiple bits per photon detection event. However, while some modern discrete and even continuous-variable QRNGs, such as [160], have achieved very impressive bit generation rates (ones admittedly much higher than the rates demonstrated in this proof of principle study), the protocol presented here, which stands alone and could achieve higher bit rates with more cutting-edge hardware, could also potentially be incorporated into some existing discrete-variable QRNG schemes to improve their rates.

Finally, the sections of this chapter which contain the experimental setup and results are prefaced by concise sections expounding the theory behind modern studies of randomness as well as the theory behind the spatial modes often considered in general higher-dimensional quantum photonics studies.

5.2 Quantifying randomness

To design and subsequently characterise a quantum random number generator, one needs a basic understanding of the mathematics behind 'randomness'. An ideal random string of length n, in base b, is a sequence of n values uniformly and independently drawn from the set $\{0, 1, \cdots, b-1\}$. The sequence of elements necessarily need to be drawn independently of one another: it should be impossible to predict the subsequent

element in the sequence, even with sight of all previous elements [161]. When $b = 2$, the situation corresponds with n trials of flipping a two-sided unbiased coin.

There are a number of alternative ways of defining and understanding randomness. For example, *Kolmogorov randomness* posits that a string is only fully random if a computer programme needed to reproduce the string is longer than the string itself [162], whereas traditional information theory typically takes completely random numbers to be those which maximise a chosen measure of information entropy [163]. We adopt the latter point of view.

A notion closely related to that of entropy in information theoretical contexts is that of *self-information*. This can intuitively be thought of as the amount of knowledge gained when observing a value x of a random variable X. The pioneer of information theory, Claude Shannon, required self-information I to meet a few intuitive axioms [6]:

1. An event certain to occur yields no new information: $I(p = 1) = 0$.

2. The more unlikely an event is to occur, the more information its observance gives, with this monotonic increase in self-information being continuous and positive: $I(p_1) \leq I(p_2)$ if $p_2 \leq p_1$, with $I(p) \geq 0 \; \forall \; p \in [0, 1]$.

3. The information gained from observing two independent events is the sum of their individual self-information values: $I(p_1 \times p_2) = I(p_1) + I(p_2)$.

Up to a multiplicative factor, it can be proven that there is a unique function which meets all three of these axioms: given a random variable X with the set of possible outcomes $\{x_i\}$ and a probability distribution $P_X(x_i) = p_i$ for $i = 1, 2, ..., d$, the self-information $I_X(x_i)$ is given by [6, 163]

$$I_X(x_i) = -\log_b(p_i), \tag{5.1}$$

in base b. In our case with $b = 2$, I_X is measured in bits. Shannon defined the *Shannon entropy*, $H(X)$, of the random variable X to be the expectation value of this self-information, i.e.

$$H(X) = -\sum_i p_i \log_2(p_i). \tag{5.2}$$

The Shannon entropy is a measure of how informative a random variable X is: it can easily be seen that perfectly random events (i.e. those where p_i is the same for all outcomes x_i) maximise H, whereas perfectly predictable events (those where p_i is either always 0 or 1) minimise it.

In our quantum system, randomness manifests itself in the purely probabilistic outcomes of projective measurements on a state ρ (compare this with **P3**). Furthermore, in a quantum setting, one often uses the notion of a quantum system's *von Neumann entropy* S [164], which is given by $S = -\mathrm{Tr}(\rho \log \rho)$. This formula holds when ρ is expressed in any arbitrary basis. However, a well-defined quantum state (see **P1**) necessarily admits a spectral decomposition $\rho = \sum_i c_i |i\rangle\langle i|$, with $|i\rangle$ the state's eigenvectors and c_i the corresponding real eigenvalues [1]. In this form with ρ diagonal with diagonal entries $\{c_i\}$, the formula for S is formally equivalent to the information-theoretic Shannon entropy of Eq. 5.2, and

$$S(\rho) = -\sum_i c_i \log_2(c_i). \tag{5.3}$$

The entropy of a quantum state is an intrinsic property independent of the chosen basis. However, Eq. 5.3's simplicity highlights the value of expressing a quantum state in its eigenvector basis. ρ is a probabilistic mixture of pure eigenstates $|i\rangle\langle i|$ with the diagonal elements $\{c_i\}$ (corresponding to the probabilities $\{p_i\}$ above) quantifying the various pure state contributions. As such, the set $\{c_i\}$ completely determines the randomness of a system.

While the above two definitions of entropy often appear in various contexts, when working in cryptography or randomness extraction (or other security-related studies), one often wishes to assume the worst case scenario. As such, consider the so-called min-entropy, defined as

$$H_{\min} = -\log_2(\max_i\{p_i\}). \tag{5.4}$$

This measure is the worst-case bound on Eq. 5.2, the lowest limit of the randomness that can be extracted from a system. We will use $H_{\min}$ in what follows since it is a more cautious estimate of a system's randomness.

In addition to measures of entropy, statistical hypothesis testing is another widely used method to quantify RNGs [165, 166]. Given a dataset of bit strings arising from a model of a RNG, hypothesis testing applies unbiased analytical tests to the dataset to gauge whether the generator itself tends to output sufficiently random strings. We use the term 'sufficiently random' since no amount of hypothesis testing can definitively prove that the protocol produces inherently random, irreproducible strings; the tests themselves only offer a simple 'pass or fail' evaluation to improve our confidence that the generator is producing numbers that have characteristics reminiscent of randomness. While many statistical test suites are available, such as John Walker's ENT [167],

DIEHARDER [168] or the well-known NIST-800 22a Statistical Test Suite [161], any finite set of tests can overlook hidden correlations. As such, no particular test suite can be deemed complete and no amount of testing on the outputs from a RNG can guarantee its robustness.

In this proof of principle work however, we employ the NIST Test Suite for the pragmatic reason that it is recognised as the industry standard and is formulated from comprehensive theoretical and experimental analyses. The measured statistics of each test are converted to a p value using a χ^2 reference distribution. These p values can then be interpreted as the likelihood that an ideal RNG would have generated a sequence less random than the tested sequence [161]. We evaluate the test results by comparing the p value to a predetermined significance level α, which is set by the required security level of the application at hand. The significance level can be thought of as the probability that the test will deny that a perfectly random sequence is in fact random (i.e. it represents the probability of observing a false negative): obtaining a p value greater than α implies that one accepts the hypothesis that the random number generator produces truly random strings while a p value of less than α implies that the random number generator may be faulty. A confidence threshold of $\alpha = 0.01$ was chosen, in which case on average 1 in 100 sequences from an ideal RNG will fail the tests by chance. It should be stressed that statistical tests usually only test the outputted sequences (and do not include any modelling of the random number generator itself) and hence, at best, can be viewed as sanity checks against obvious flaws rather than being definitive proof of randomness. As mentioned earlier, it remains essential to assess the physical process behind a RNG [169].

5.3 Spatial modes & SPDC

The electromagnetic field, and in particular its excitations at the single photon level, has proven to be a rich source of easily engineered quantum mechanical phenomena. On the classical level, Maxwell's equations describe the behaviour of electromagnetic radiation as being a wave with speed c. Given this wave equation, factoring out the time dependence of the - as yet unknown - solution, the resultant *Helmholtz equation* describes the radiation's profile in space [170]. Next, experiments in optics and photonics almost exclusively employ paraxial coherent laser light, the propagation direction of which is almost entirely constrained to a single propagation axis (the system's optical axis, usually chosen to be the z direction). Applying this *paraxial approximation* to the Helmholtz equation in turn gives

$$\frac{\partial^2 A(\boldsymbol{x})}{\partial x^2} + \frac{\partial^2 A(\boldsymbol{x})}{\partial y^2} = 2ik\frac{\partial A(\boldsymbol{x})}{\partial z}, \tag{5.5}$$

where k is the wavenumber and A the electromagnetic field amplitude (propagating in the z direction). Solutions to this equation are often the focus of optical studies.

Our proposed random number generator, which operates at the quantum level, measures properties of pairs of photons created via SPDC [30]. The well-known Laguerre-Gaussian (LG) modes, $\mathrm{LG}_p^\ell(\boldsymbol{q})$, which are also solutions to Eq. 5.5 above, are chosen as the complete basis for the vector space of each photon [171]. Here, $\ell \in \mathbb{Z}$ is the azimuthal index (a photon with such an azimuthal index possesses orbital angular momentum of $\hbar\ell$), $p \in \mathbb{Z}^{0+}$ is the radial index, and $\boldsymbol{q} \in \mathbb{R}^2$ is the two-dimensional wavevector component transverse to the optical axis. Note that $\mathrm{LG}_p^\ell(\boldsymbol{q})$, the momentum-space representation of an LG mode, is the Fourier transform of a real-space LG-mode solution. With this, the entangled biphoton state $|\psi_{\mathrm{SPDC}}\rangle$ can be written as a superposition of LG modes

$$|\psi_{\mathrm{SPDC}}\rangle = \sum_{\substack{\ell_s,\ell_i \\ p_s,p_i}} C_{p_s,p_i}^{\ell_s,\ell_i} |\ell_s, p_s\rangle |\ell_i, p_i\rangle, \tag{5.6}$$

where $|\ell, p\rangle = \int d\boldsymbol{q} \mathrm{LG}_p^\ell(\boldsymbol{q}) \hat{a}^\dagger(\boldsymbol{q})|0\rangle$ is the state of an LG-mode photon with indices ℓ and p, $\hat{a}^\dagger$ is the usual creation operator, $|0\rangle$ is the vacuum state, and the subscripts s, i merely distinguish the two photons (called the signal and idler photons for historical reasons). The probability amplitudes $C_{p_s,p_i}^{\ell_s,\ell_i}$ fully characterise the entangled biphoton state $|\psi_{\mathrm{SPDC}}\rangle$. The joint probability of finding the signal and idler photons in the $|\ell_s, p_s\rangle$ and $|\ell_i, p_i\rangle$ states, respectively, upon performing a joint projective measurement is given by $|C_{p_s,p_i}^{\ell_s,\ell_i}|^2$, where

$$C_{p_s,p_i}^{\ell_s,\ell_i} \propto \int d\boldsymbol{q}_s d\boldsymbol{q}_i \Phi(\boldsymbol{q}_s, \boldsymbol{q}_i) \left[\mathrm{LG}_{p_s}^{\ell_s}(\boldsymbol{q}_s)\right]^* \left[\mathrm{LG}_{p_i}^{\ell_i}(\boldsymbol{q}_i)\right]^*. \tag{5.7}$$

The quantity Φ describes the profile of the pump beam (usually a paraxial Gaussian beam) as well as the phase-matching condition [30]. By the conservation of momentum, the OAM charge of the input pump photon equals the sum of the OAM charges of the signal and idler photons the pump photon gives rise to, i.e. $\ell_p = \ell_s + \ell_i$ [172]. Furthermore, assuming a Gaussian pump beam (where $\ell_p = 0 = p_p$), the entangled down-converted photons have equal but oppositely charged OAM values, $\ell \equiv \ell_s = -\ell_i$. Note that although most studies on OAM focus on the azimuthal charge ℓ, the radial index p is important in its own right [173].

Finally, note that our chosen experimental measurement scheme is sensitive only to different OAM charges. Given a Gaussian pump, $C_{p_s,p_i}^{\ell_s,\ell_i}$ amplitudes with non-zero radial indices are generally found to be far smaller in magnitude compared with the $p = 0$ amplitudes. We can hence take the former to be approximately 0 and take only the latter into consideration in Eq. 5.6. Designating the idler, signal photon paths with A, B subscripts respectively, the SPDC state is hence

$$|\psi_{\text{SPDC}}\rangle = \sum_{\ell} C_\ell |\ell\rangle_A |-\ell\rangle_B, \tag{5.8}$$

where C_ℓ is the probability amplitude of the $|\ell\rangle_A|-\ell\rangle_B$ state. Therefore, performing a joint coincidence measurement on the state $|m\rangle_A|-m\rangle_B$ (i.e. projecting onto state $|m\rangle$ and $|-m\rangle$ in the idler and signal arms respectively) picks out the corresponding probability amplitude C_m. The probability of observing the state $|\psi_{\text{SPDC}}\rangle$ in the ℓth mode is given by $|C_\ell|^2$.

In practice, we shape, or 'structure' the paraxial light using spatial light modulators and projective measurements in order to achieve these higher-dimensional entangled states. These techniques are almost identical to those employed in Chapters 2 and 3. See [77] for a comprehensive review of modern techniques used in studies of structured light and the review articles listed in previous chapters for detailed explanations of SLMs and similar apparatuses.

5.4 OAM random number generator setup

The setup shown in Fig. 5.1 is a variation of the widely-adopted QRNG scheme based on path branching [152]. In the original scheme, the RN generator was built using a beamsplitter to create a superposition of two states labelled with path information. To allow for dynamic control over both the incident beam's spatial profile as well as our RNG's statistics, a phase-only Holoeye Pluto-2 SLM was used, which probabilistically directs the incident photon down one of two paths. This in essence mimics the action of a beamsplitter.

The equipment used in our setup is similar to that used in Chapters 2 and 3. First, a pair of degenerate type-I entangled photons, created with a 355nm mode-locked Vanguard UV laser and a nonlinear BBO crystal, are spatially separated into paths A and B with a D-shaped mirror. The crystal plane is imaged onto a SLM placed in each path.

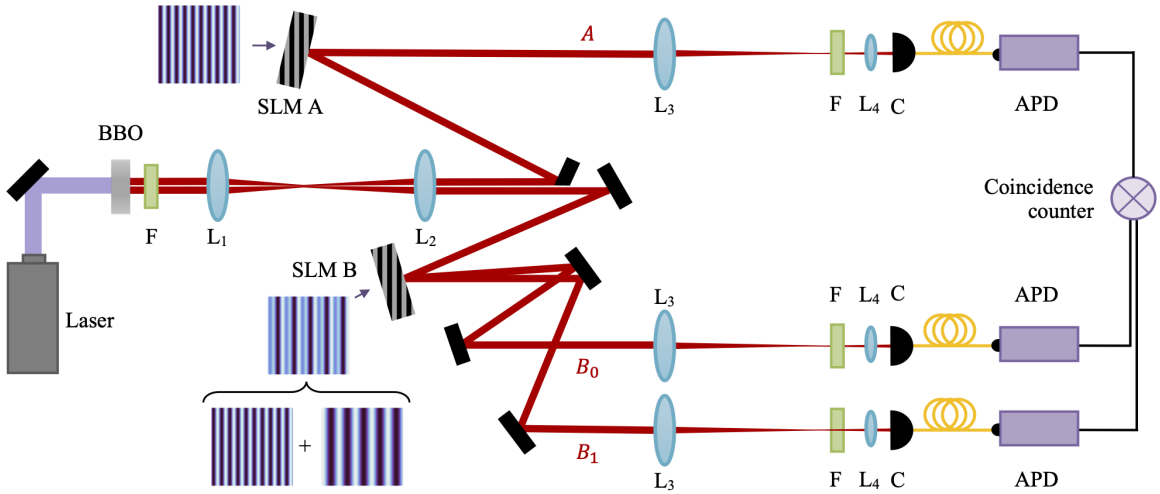

Fig. 5.1 **OAM random number generator setup**. First, the down-converted photon pair is split into two optical paths. The path A photon (the idler) simply acts as the heralding photon. The path B (signal) photon is itself probabilistically directed down either path B_0 or B_1 using SLM B. A random bit is generated when a coincidence detection event is registered between path A and either path B_0 or B_1. F: filter, L_1: 200mm lens, L_2: 400mm lens, L_3: 500mm lens, L_4: 2mm lens, C: coupler, APD: avalanche photodiode.

The modulated light, which lies in the first diffraction order, is separated from the unmodulated light by aligning the setup with holographic diffraction gratings loaded onto the SLMs. Being able to digitally control the frequency of the diffraction grating also makes the setup easier to align (later, SLM A is also used to project photon A onto different OAM modes when characterising the system and measuring its spiral bandwidth).

Photons in path A function as the heralding photons. SLM B, however, is masked with a juxtaposition of two diffraction gratings, each with different spatial frequencies, instead of a single one. This double diffraction grating causes a photon in path B incident on the SLM to be directed into one of two paths, B_0 or B_1. The choice of path occurs completely probabilistically and the probabilities themselves can be controlled by modulating the individual respective grating depths (i.e. the diffraction efficiencies) of the gratings comprising the juxtaposed SLM B mask; altering the grating depths alters the proportion of incident light diffracted into the first order of either grating.

To be more specific, if one is given a diffraction grating hologram with a maximum possible phase depth of 2π within some local region, subsequently scaling the phase range of the pixel at transverse position (x, y) by a factor of $M(x, y)$ (where $M \in [0, 1]$) splits the diffracted light into multiple orders according to [78]

$$|c_n(x,y)|^2 = \mathrm{sinc}^2\left[\pi(n - M(x,y))\right], \tag{5.9}$$

where n is the diffraction order and $|c_n|^2$ is the fraction of power in this nth order [174]. For the first order ($n = 1$), reducing the phase depth across the entire hologram directs a greater proportion of the incident photons out of the first order. The case of two juxtaposed gratings corresponding to paths B_0 and B_1 is slightly more complicated. However, one can still use this technique to digitally control any bias in the system to achieve the desired ratio of photons in each path. This provides us with a simple tool to mitigate experimental imperfections in the system, such as mismatched detector efficiencies and optical losses in each arm. Furthermore, this can also eliminate the need for cumbersome randomness distillation algorithms post measurement.

After the SLMs, lenses and couplers in the three paths couple the photons into fibres which are connected to Excelitas avalanche photodiodes. These devices output an electrical TTL pulse signal for every detection event observed. A Hydraharp 400 time tagged each pulse (with a resolution of 1ps). This creates a record of both the arrival time as well as the path in which the detection event occurred. With this record, to extract photon coincidences one simply reconciles the overlapping APD pulses which separately arise for a photon detection event in either path B_0 or B_1, with a pulse in path A. Indeed, photon A, the trigger photon, causes either the path B_0 or B_1 detector to register a corresponding entangled photon if the arrival times lie within a small, predetermined tolerance interval. Such a situation is a close approximation to a localised single-photon state [175].

The resultant data was then post-processed to generate the random bit strings and two detectors were said to have detected a pair of entangled photons if a single photon was tagged at each respective detector with the corresponding arrival times differing by a maximum of 25ns (such a value was chosen to minimise false coincidences). If detectors A and B_0 together registered an entangled photon pair, a '0' was appended to our random bit string. Likewise, a '1' was added for a coincidence between detectors A and B_1. This entire process was fully automated using LabVIEW.

Finally, it is worth mentioning that a perfectly unbiased system should register the same number of photon detection events in each of the B subpaths, the sum of which should furthermore equal the number of events registered in arm A. Experimentally, although the down-conversion efficiency of the crystal and the extraction algorithm itself affect the protocol's efficiency, the most significant bottleneck in the RN generation rate is typically the single-photon APDs [26].

5.5 Results & discussion

5.5.1 Path information random numbers

First, the experimental setup of Fig. 5.1 was used to generate RNs from the photons' path information. Perhaps unsurprisingly, there were initially disparities between the two arms and the setup hence outputted unequal coincidence detection probabilities, p_0 and p_1, between the detector pairs $A - B_0$ and $A - B_1$, respectively. In particular, we define a bias ratio, $R = p_0/p_1$, which should be 1 for a perfectly unbiased system. R was found to be 0.854 ± 0.002 initially (i.e. B_1 was slightly favoured). This gives a min-entropy value of $H_{\min} = 0.891 \pm 0.001$ bits, whereas the ideal value is 1 (note that one can express Eq. 5.4 in terms of R with $p_1 = 1/(R+1)$ and $p_0 = R/(R+1)$). While this at first may appear to be a small discrepancy, randomness tests typically pick up on this and flag the RNG as faulty. Indeed, a 1Mb sequence generated with our scheme, when subjected to the NIST Test Suite, failed to pass three of the 15 statistical tests as per Fig. 5.2(a): the p values were well below the chosen significance level of 0.01 (a level typical for cryptographic applications [161]). This error greatly affects the randomness of our protocol. To overcome such bias, many other QRNG systems apply numerical debiasing techniques to extract clean random bit strings from imperfect data [154]. However, such an extra step is often inefficient and retards the generation rate by necessitating the consumption of bits.

This problem is relatively easily overcome in our protocol by altering the diffraction efficiency of the more favoured arm (here B_1) by changing the phase grating depth of the SLM hologram. The particular SLM we employed was calibrated such that the displayed 8-bit grey-scale images represent a total possible phase of 2π. Scaling path B_1's diffraction grating by a factor $M \in [0, 1]$ (see Eq. 5.9) decreases p_1 according to $p_1 \to p_1' = p_1|c_1|^2$. Furthermore, the renormalised constraint $p_0' + p_1' = 1$ implies that $p_0 \to p_0' = 1 - (1 - p_0)|c_1|^2$. As such, the min-entropy becomes $H_{\min} = -\log_2(\max(p_0', p_1'))$.

The effect that the SLM scaling, M, and the initial bias ratio, R, have on $H_{\min}$ is depicted in Fig. 5.3(a). Given our initial bias ratio of $R = 0.854 \pm 0.002$, the slice of Fig. 5.3(a) with this R value is shown in Fig. 5.3(b), and the experimental data points confirm the anticipated relation. To maximise the entropy, the count rate (i.e. detection probability) of arm B_1 hence needed to be decreased to match that of arm B_0. This occurs when the grating in arm B_1 is scaled by a factor of $M = 0.852$. The SLM device used to do this has a typical resolution of 1/256 (with the grey-scale holograms corresponding to a total phase change of 2π). As such, the min-entropy resolution in this instance is given by

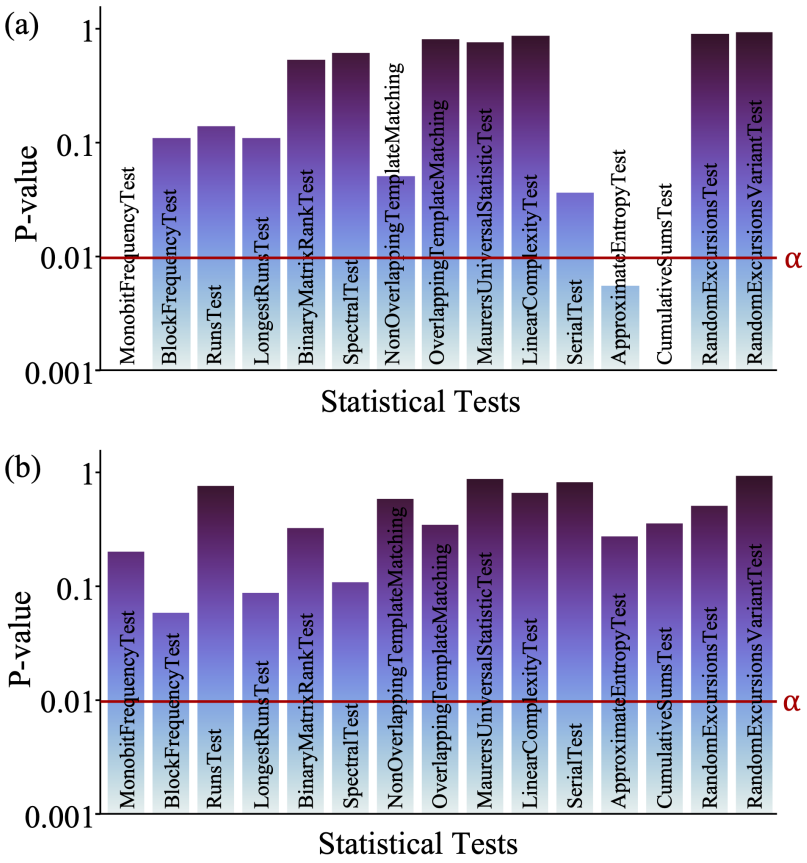

Fig. 5.2 **NIST Test Suite results for a 1Mb sequence**. (a) shows the results for the initial QRNG without having corrected the inherent experimental bias, while (b) gives the corrected results after having adjusted the SLM grating appropriately. p values above the significance level of $\alpha = 0.01$ indicate that the corresponding test was passed.

$$\delta H_{\min} \approx \delta M \left.\frac{\partial H_{\min}}{\partial M}\right|_{\substack{R=0.854,\\ M=0.852}} = \frac{1}{256} \times 1.438 \approx 0.006. \tag{5.10}$$

After carrying out this procedure to adjust the detection probabilities of both arms, a corrected bias ratio of $R' = p'_0/p'_1 = 0.999 \pm 0.001$ was achieved. This in turn resulted in a new min-entropy of $H_{\min} = 0.999 \pm 0.001$ bits per photon, which is very close to the theoretically ideal value of 1, at which point one observes maximum randomness. Indeed, an unprocessed generated random bit string of 1Mb, from the corrected system, passed all of the NIST tests (with the results given in Fig. 5.2(b)). This absence of patterns in the random bit string gives credence to the hypothesis that our QRNG outputs sufficiently random numbers. Note that despite the pass results increasing

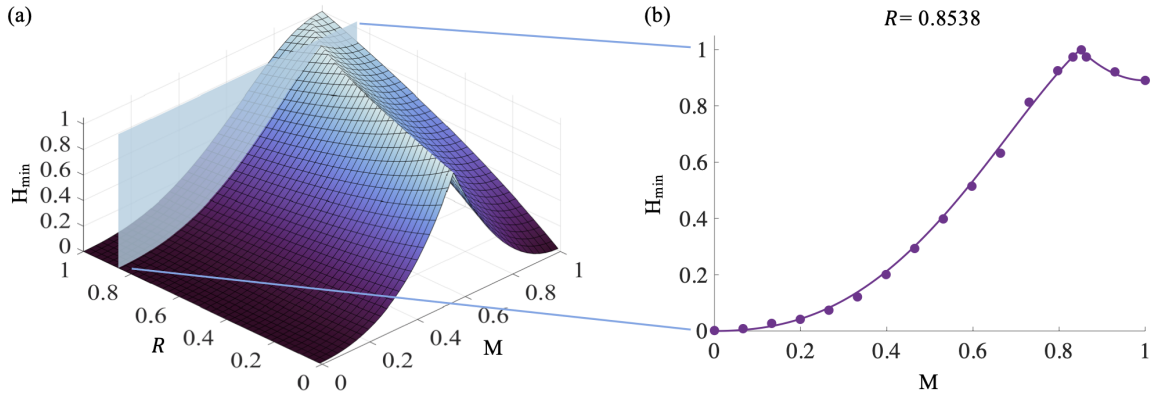

Fig. 5.3 **Relation between the min-entropy, grating depth and bias ratio of our system**. (a) Theoretical $H_{\min}$ value for our QRNG as a function of the grating scaling M and the bias ratio R. The initial, uncorrected system had a bias of $R = 0.854 \pm 0.002$, and (b) gives the predicted $H_{\min}$ value as a function of M for this R. Scaling the hologram using the peak M value of 0.852 subsequently gave a new corresponding min-entropy value of $H_{\min} = 0.999 \pm 0.001$ bits per photon. This is confirmed by the experimental data points.

our confidence in the generator, such statistical tests cannot generally be used as comparative measures between different RNG systems.

Next, in most quantum optics studies one also has to take detector dark counts and false coincidences into account as they are common challenges and may have a bearing on the quality of the RNG. In our case, we gauged the dark counts' effect by considering the ratio of the photon counts registered at the detectors (n_p) to the detector dark counts (n_d) in the form of the signal-to-noise ratio $S/N = 10 \log_{10}(n_p/n_d)$. For the particular Excelitas APDs used, the dark count rate is about 250Hz. Also, the mean photon counts recorded by each detector were observed to be 600kHz on average. This results in a S/N of 34dB, a negligible value. Furthermore, any effect from false coincidences would be far smaller. As such, the system indeed appeared to generate random numbers with statistics derived almost exclusively from genuine coincidences, and as such, derived from a quantum source.

This path information QRNG achieved a bit generation rate of 24kHz when single-mode fibres (which only accept Gaussian optical modes) were used, and up to 0.46MHz when the single-mode fibres were swapped out with multi-mode ones. It must be mentioned that optical QRNGs, which could exploit a number of different degrees of freedom, have managed to achieve far higher bit rates even after applying some debiasing protocols [26]. However, our protocol presented in this proof of principle demonstration is novel for two reasons. First, the OAM of a photon lies in a higher-

dimensional Hilbert space and, as yet, has not been studied as a source of entropy. Extracting more than one bit of information per detection event (i.e. using a higher-dimensional degree of freedom) is one of the most efficient ways of increasing a RNG's bit rate [26]. Second, our proposal is novel in that the technique of scaling the SLM hologram grating allows the experimenter to perform some debiasing of the system in real time. Despite the fact that offline processing in quantum systems is always required, this technique does mitigate the need for this; indeed, the real-time generation of bit strings is missing from most modern protocols. Our bit rate here could also be increased by using more sophisticated biphoton sources and newer equipment, such as ICCDs with better time resolution.

5.5.2 OAM random numbers

Next, our QRNG was adapted to generate random numbers from the OAM degree of freedom of entangled biphoton pairs. To achieve this, SLM B was loaded with a mask comprising a superposition of two Laguerre-Gaussian modes and diffraction grating holograms. The two diffraction gratings, with different spatial frequencies, probabilistically direct the incident path B photon down one of the two possible subpaths (and are also scaled to account for any bias, as outlined in Section 5.5.1), while the corresponding superimposed OAM holograms impart an OAM charge on the photon which is directed into the corresponding subpath. Combined with single-mode fibres (which only couple photons with OAM charges of 0), the system in effect performs projective measurements (**P3**) on the path B photon. A photon will hence only be registered by a detector in either of the subpaths if it possesses a specific OAM value. As such, this simple modification (which is a well-established spatial mode detection technique [79]) allows the QRNG to now draw its randomness from the OAM value of the down-converted photon incident on SLM B. Path A is fitted with a multi-mode fibre (which admits all spatial modes of any OAM value) and SLM A masked with only a diffraction grating. This is simply to ensure the correct heralding of path B photons.

The mode availability of each arm of the RNG was first characterised by spiral bandwidth measurements. This involved iterating through a set of projective OAM measurements in each path. The results of this process (namely the normalised coincidence counts for the various OAM projections) are given in Fig. 5.4. The full width at half maximum (FWHM) value of 19 indicates that a large proportion of the OAM values of photons A and B were correlated. Note that the path B projective measurement was performed, alongside that of path A, by appropriately combining measurements from both paths B_0 and B_1.

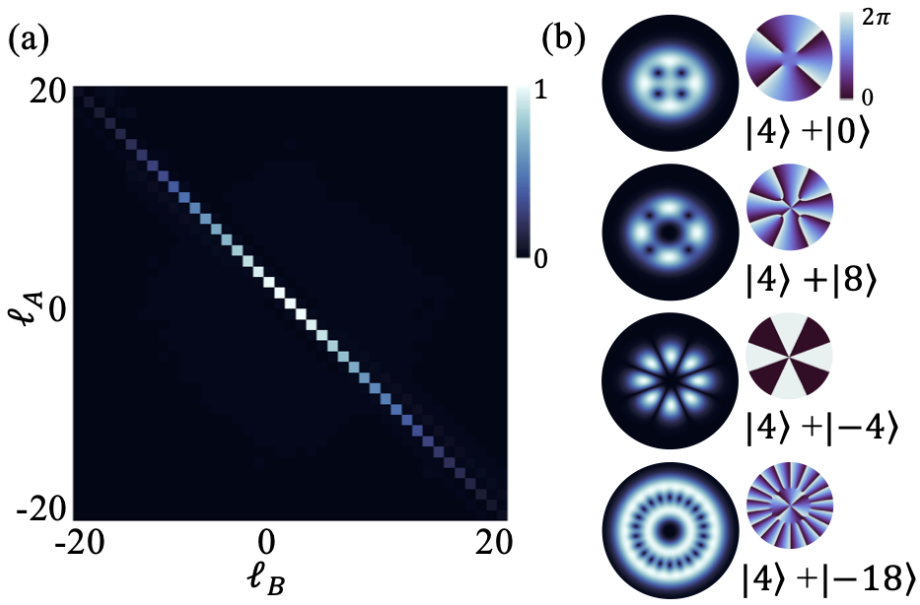

Fig. 5.4 **System spiral bandwidth characterisation**. (a) Normalised probability matrix for different OAM projection combinations in paths A and B. The FWHM of 19 indicates a high OAM mode availability; access to this potentially countably infinite set of OAM states is limited chiefly by experimental constraints. (b) Plots of some intensity and phase profiles of the various possible OAM combinations. Judiciously choosing these profiles offers another method of tailoring the probability distribution of the system.

These experimental coincidence count values allow one to deduce the entropy, and hence randomness, of the system. First, as before, the juxtaposed gratings on SLM B are scaled to ensure that it is equally likely for a path B photon to be directed down either path B_0 or B_1. Next, if a path B_0 photon is projected onto an ℓ_{B_0} eigenstate and an independent photon in path B_1 onto an ℓ_{B_1} eigenstate (note that they are independent since a photon in path B only traverses one of the two subpaths), the min-entropy is a function of these two OAM charges, $H_{\min} \equiv H_{\min}(\ell_{B_0}, \ell_{B_1})$. This is the case because the probabilities of registering a bit value of 0 or 1, i.e. p_0 or p_1 respectively, in general depend on the modes projected onto in the subpaths, namely ℓ_{B_0}, ℓ_{B_1}, as well as the mode projected onto in arm A, ℓ_A. So, $p_0 \equiv p(0|\ell_{B_0}, \ell_{B_1}, \ell_A)$ and similarly for p_1. However, photon A in this scheme simply functions as a heralding photon and the inclusion of the multi-mode fibre in path A means that all OAM values for photon A are registered (in the end, we do not project onto particular OAM values in path A; this is only necessary when characterising the system). This means that

when deducing the min-entropy conditioned on both ℓ_{B_0} and ℓ_{B_1} we use marginal probabilities with the photon A OAM value 'traced out' (i.e. summed over), so

$$p(0/1|\ell_{B_0}, \ell_{B_1}) = \sum_{\ell_A} p(0/1|\ell_{B_0}, \ell_{B_1}, \ell_A). \tag{5.11}$$

Furthermore, the probability of generating a 0 bit is independent of the chosen OAM projection value in path B_1 since a 0 bit value is only generated if a photon is registered in path B_0 and it doesn't matter what value was chosen for ℓ_{B_1}. Therefore

$$p(0|\ell_{B_0}, \ell_{B_1}) \equiv p(0|\ell_{B_0}), \tag{5.12}$$

and similarly for a 1 bit value, $p(1|\ell_{B_0}, \ell_{B_1}) \equiv p(1|\ell_{B_1})$. Finally, given that the probability of observing a 0 or 1 is proportional to the spiral bandwidth coincidence count values between $A - B_0$ or $A - B_1$ respectively, data corresponding to Fig. 5.4(a), but for the two subpaths rather than the entire B path, was collected. This allows one to deduce $p(0|\ell_{B_0})$ and $p(1|\ell_{B_1})$ by summing the coincidence count values over the ℓ_A variable (assuming a reasonable cutoff) and normalising the final answer. Similarly, one can calculate a bit generation rate for the different OAM values ℓ_{B_0} and ℓ_{B_1}. The experimental min-entropy and generation rates as functions of ℓ_{B_0}, ℓ_{B_1} are given in Fig. 5.5(a).

Various random bit strings were then experimentally generated for a subset of possible OAM projections, namely setting $\ell_{B_0} = 4$ and $\ell_{B_1} \in \{-20, \cdots, 20\}$ (note that the chief reason we need to project onto different OAM charges in this protocol is a result of the experimental measuring technique; using an OAM mode-sorter and an ICCD, for example, would allow one to measure all possible OAM values in real time without needing to project onto particular values). The experimental $H_{\min}$ and bit rate values are shown in Figs. 5.5(b) and (c) respectively. From this, one achieves the highest min-entropy value of 1 bit per detection event when projecting the two B subpaths onto OAM states possessing equal magnitudes (i.e. $|\ell_{B_0}| = |\ell_{B_1}|$). This is expected, as OAM momentum conservation ensures an equal probability of measuring the conjugate OAM value in either subpath. Next, given that the SPDC state's probability amplitudes are known to taper off for higher OAM values, projecting each subpath onto higher OAM charges results in lower detection probabilities and hence lower random bit generation rates, as confirmed in Fig. 5.5(c). Indeed, projecting the down-converted photons onto OAM eigenstates with increasingly larger differences in their absolute OAM values correspondingly lowers the min-entropy and bit generation rate.

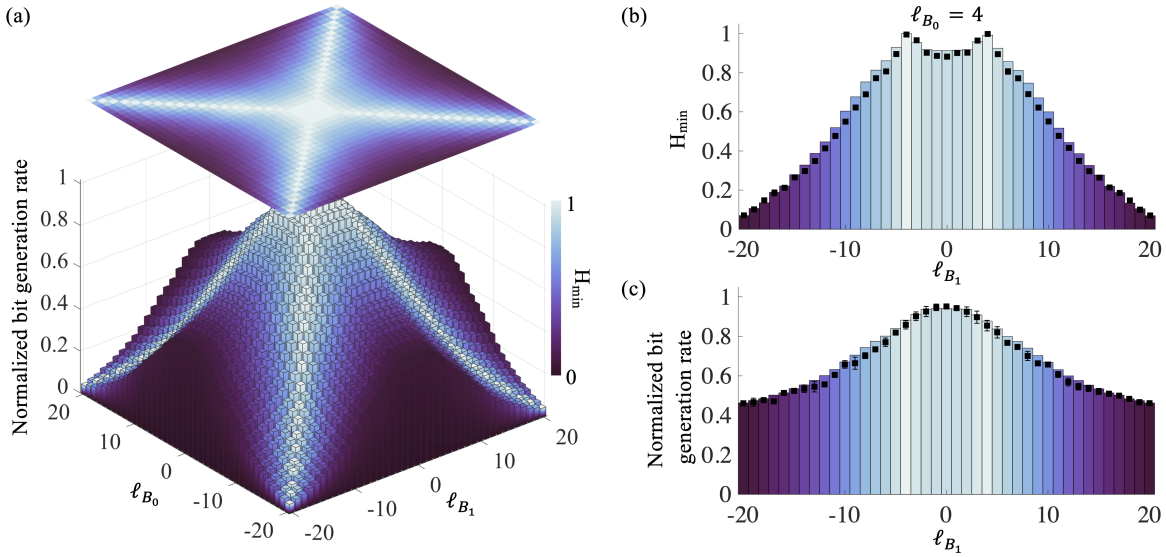

Fig. 5.5 **OAM QRNG experimental results**. (a) shows the min-entropy (hue) and normalised bit generation rate (bar height), as functions of the different OAM projection combinations, calculated from the spiral bandwidth measurements. With ℓ_{B_0} set to 4, random bit strings were then generated. (b) gives the corresponding experimental min-entropy values as a function of $\ell_{B_1} \in \{-20, \cdots, 20\}$ and (c) gives the normalised bit generation rates calculated from the generated random bit strings.

These results confirm the potential of using a photon's OAM degree of freedom to generate random bits. While work would still undoubtedly need to be done to improve the system's bit rates and efficiencies, this should be possible using modern apparatus. Contemporary RNG systems may consider incorporating OAM sensitive detectors to enhance them. Furthermore, the holographic grating scaling and OAM projection techniques demonstrated here potentially offer a method with which to tailor the probability distribution of the system, as many practical applications call for distributions other than the uniform one. With the current protocol this would unfortunately come at the cost of a reduced bit generation rate. However, given a system tailored with a particular probability distribution, observing random bit strings not following the expected distribution could also potentially alert the user to the presence of an adversary.

Finally, up until this point, only two OAM values were considered simultaneously as sources of entropy: the setup of Fig. 5.1 only has two subpaths in arm B, and these subpaths are in one-to-one correspondence with the chosen projected OAM values. Given that OAM eigenstates lie in a higher-dimensional Hilbert space, this and their relatively easy experimental manipulation suggests the possibility of exploiting their

higher-dimensional nature to build a 'multibit' QRNG. While the spatial information of a photon has previously been used to realise such multibit QRNGs [157, 176], no experiment has to date considered generating more than one bit, per detection event, using a photon's OAM. Indeed, high bit generation rates comparing favourably with existing QRNGs are not beyond the realm of possibility given the existing modulation/multiplexing schemes and OAM sensitive detection devices available.

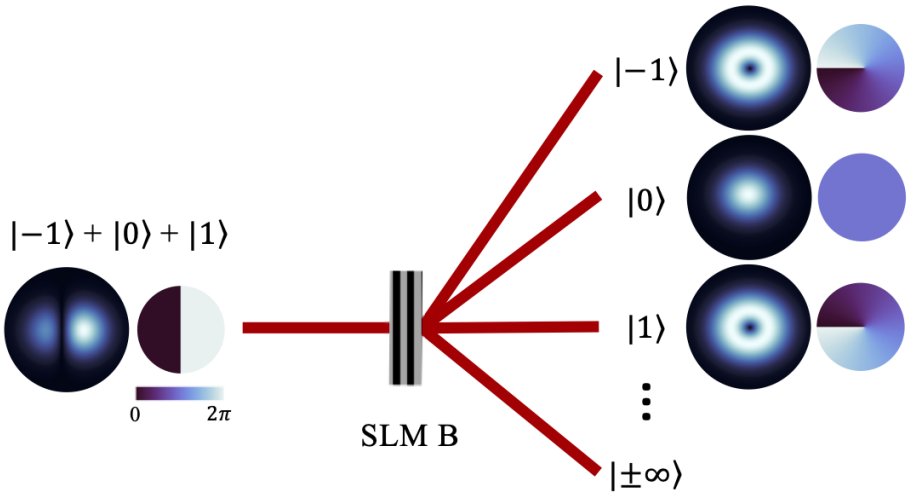

Fig. 5.6 **Multibit quantum random number generation using OAM**. The schematic shows how the previous setup is adapted to realise a multibit QRNG. By projecting photons in path B down OAM-dependent subpaths (where we chose $\ell \in \{-1, 0, 1\}$) and registering coincidence counts in any of these three paths (with photon A still the herald), random ternary values were easily generated. This approach could be scaled to higher dimensions.

With this in mind, the setup in Fig. 5.1 was adapted to include a third path, B_2. SLM B was masked with a multiplexed hologram consisting of three OAM values (chosen to be $\ell \in \{-1, 0, 1\}$), each with a unique diffraction grating (see Fig. 5.6). As such, the photons incident on SLM B were mapped down one of three OAM-dependent paths. The experiment was then repeated exactly as in the two-dimensional OAM case above, with photon A heralding the detection of a photon in path B_0, B_1 or B_2. This generated a ternary sequence of random values, resulting in a multibit QRNG which draws its entropy from the OAM content of a down-converted photon. The digital SLM debiasing techniques from before allow one to easily adjust the coincidence detection probabilities such that all three are equal (however, one could alter the gratings to achieve a custom arbitrary higher-dimensional probability distribution).

In this way, a random string of numbers, with each detection event corresponding to more than 1 bit of information, was generated. We hence achieved our goal of an

OAM-based higher-dimensional QRNG. To quantify the system, it is worth noting that there is, as yet, no obvious statistical test suite with which to probe the randomness of a ternary string. We hence instead turn to min-entropy as a quantitative measure. For an ideal three-dimensional QRNG, the amount of entropy attainable from each photon is $\log_2(3) = 1.585$ bits. Using Eq. 5.4, the min-entropy of the random strings generated from our system (after correcting and debiasing) was found to be $H_{\min} = 1.577 \pm 0.001$. This is close to the ideal value. Furthermore, the higher-dimensional nature of the generated strings means we also achieve an increased bit generation rate compared to the previous two-dimensional case. The two- and three-dimensional min-entropy results are summarised in Table 5.1.

Dimension	**Min-entropy (theoretical)**
$d = 2$	$0.999 \pm 0.001 \quad (1)$
$d = 3$	$1.577 \pm 0.001 \quad (1.585)$

Table 5.1 Measured $H_{\min}$ values for the $d = 2, 3$ OAM-based QRNG cases.

As per the schematic in Fig. 5.6, this OAM QRNG could be extended to even higher dimensions (subject to obvious experimental limitations such as the system's numerical aperture). However, scaling the system up in the current case would require an additional subpath for every additional OAM value to be included, and hence the system, as is, does not scale nicely. However, this is simply a result of the chosen detection equipment. A more efficient, feasible improvement could entail using mode sorting to conformally map a photon's input OAM charge to a lateral spatial position [177, 178] and subsequently detect such lateral positions with an array of single-photon detectors (such as with an ICCD).

5.6 Conclusion

In Chapter 5 we introduced both a novel technique and a new protocol. First, the integration of holographic SLMs in an optical QRNG scheme was demonstrated. This allowed for the easy digital control of the probability distribution of the system by replacing the traditional static beamsplitter with a device with which one can easily tailor the probability of the down-converted photon being directed down either subpath. This simple technique of hologram grating scaling also offers one a technique with which to partly mitigate any inherent asymmetries in the transmission and detection

portions of the system, which affects the quality of the generated random bits. This all occurs 'on the fly', not post measurement.

While many QRNGs indeed focus on drawing random numbers from a uniform distribution, other distributions are also necessary in practice. For example, any half-decent casino slot machine would want the player to lose a game far more often than win one. A series of these simple binary 'win-lose' games is modelled by a binomial distribution consisting of a sequence of independent drawings from a Bernoulli distribution. For this latter distribution, one draws a 0 with a probability p and a 1 with a probability $1 - p$. In an optical setup, although one can achieve such a Bernoulli distribution by, for example, tuning a half-wave plate in a path-information-based QRNG which incorporates a polarising beamsplitter, using our scheme makes the process more dynamic. Furthermore, although we only demonstrated the two- and three-dimensional cases, this technique easily adapts to higher-dimensional cases which would use more OAM values and could create more complicated probability distributions. It is worth mentioning however that the intrinsic OAM distribution of the down-converted biphoton state strongly depends on both the profile of the pump field incident on the nonlinear crystal as well as the type and size of the nonlinear crystal itself. Therefore, further advances in the area of pump shaping could be incorporated into this protocol to tune the distribution, and hence the system's entropy, more finely given a particular crystal [179, 180].

Second, we implemented a QRNG based on the OAM degree of freedom of down-converted photon states. The use of SLMs and single-mode fibres to project onto OAM eigenstates created a one-to-one correspondence between the paths and OAM charges. Using the above techniques, one can tailor the entropy of the system all while maintaining the inherent quantum indeterminism. This OAM QRNG was demonstrated in both a two- and three-dimensional case. The measured entropy in both cases were very close to their theoretical maxima and the bit strings in the two-dimensional case passed the complete NIST Test Suite despite having undergone no post-processing.

This proof of principle work is an important first step in realising an OAM-based, higher-dimensional QRNG. Two properties of an ideal QRNG would be a high bit generation rate as well as the real-time generation of random strings (i.e. no post-processing procedure required). The protocol presented here already includes the possibility of upping the rate if more sophisticated equipment were used and more OAM modes considered. In addition, modifying the setup to forgo the projective, iterative 'scanning' detection technique and instead using equipment capable of discriminating the various OAM modes in real time (such as using mode sorters and ICCDs) opens

up the latter possibility. Finally, although many efficient QRNGs already exist (see [26, 148]), the OAM scheme presented here could conceivably be incorporated into some of them to increase their efficiencies.

Chapter 6

Overall conclusion & outlook

Despite the fact that there have been many great theoretical and experimental studies into quantum mechanics since its birth in the first half of the 20th century, this is an area of physics which is somewhat unique in that it seems to constantly output new and unintuitive results, even in the present day. Given that all of physics, and by extension Nature itself, must ultimately have quantum mechanics as its bedrock, this is still an exciting time for science as a whole.

In this thesis, we presented four studies within the context of quantum photonics, a subfield of physics in which it is relatively easy to experimentally observe and test the four postulates outlined in the Introduction, along with their interesting consequences. We chiefly focused on quantum ghost imaging and quantum random number generation. This all represents but a small contribution to the existing body of knowledge. Indeed, although a number of interesting experiments were demonstrated, results arrived at and questions answered, as always, answering one scientific question potentially opens the door to new ones.

Chapter 2 demonstrated a novel four-way quantum ghost imaging scenario in which correlations between two pairs of initially independent down-converted photons were created using entanglement swapping. This entanglement swapping, carried out with a HOM filter and appropriate coincidence postselection, resulted in the creation of an anti-symmetric state with which to perform said ghost imaging, rather than the usual symmetric state arising from SPDC. One main result was the observation of a 'contrast reversed' ghost image in this anti-symmetric case, where brighter pixels in the object corresponded to darker pixels in the ghost image, and vice versa. This appears to stem from the symmetry of the tailored state, which shows how interesting symmetry as a concept is. Indeed, symmetry has a strong bearing on physics in a variety on contexts. For example, the well-known Bose-Einstein Condensation [34] and the Pauli

Exclusion Principle [181] phenomena are both a result of a quantum state's symmetry. Furthermore, changing a particle's state's symmetry has been observed elsewhere. For example, BCS theory [35, 182] details how the phenomenon of superconductivity in a material is a result of the formation of Cooper pairs, which are pairs of electrons occupying bound states at low temperatures. Single electrons have intrinsic spins of 1/2 and as such are fermions obeying Fermi-Dirac statistics [183]. However, by cooling a conventional superconductor material to extremely low temperatures, the state of pairs of electrons eventually possesses an energy below the Fermi energy of the system [183]. When this happens, the electron pair state is bound into a composite state with a total spin of either 0 or 1. States with integer spin obey Bose-Einstein statistics [183] because of the strong relation between a state's spin and its statistics/symmetry (by the so-called *spin-statistics theorem* [5]). The result of all of this is the many interesting superconductor phenomena which have been experimentally observed in recent decades. With this in mind, it may be interesting for future work to consider more deeply the link between the symmetry of a biphoton state and the ghost image obtained with said state, and whether a change in symmetry would have any resultant bearing on the photons' statistics.

Quantum technologies will become increasingly prevalent in society, and creating links between nonlocal quantum optical network systems may become necessary. Our four-way ghost imaging demonstration contains the core ingredients which may be required of any such future quantum optical network [76]. The efficiency reported on in Chapter 2 would obviously have to be improved upon, but the fact that the entanglement swapping protocol (which is how the links were created) theoretically works in higher dimensions is worth emphasising. Finally, the techniques presented could also be adapted in both classical and quantum settings to enhance or alter the observed ghost images in nontrivial ways. Quantum imaging is finding use in many devices [184] and any studies into improving imaging techniques should also prove fruitful.

Next, Chapter 3 also considered quantum ghost imaging but within the context of a simpler two-way setup. The state was now tailored using a pair of Dove prisms along with the usual HOM filter and appropriate postselection scheme. In the symmetric case the usual anticipated ghost image was observed. On the other hand, in the anti-symmetric case (i.e. in the presence of a HOM filter and postselection protocol), we observed a novel result in that the ghost image turned out to be a juxtaposed image consisting of the original object rotated both clockwise and counterclockwise by a controllable angle. This interesting result again appears to stem from the tailored

symmetry of the input state and as such brings forth interesting questions very similar to those stated above. However, two other important points which future work may consider looking into are worth mentioning. First, the action of the Dove prisms and the HOM filter (indeed, most optical equipment) are described by unitary operators and hence align neatly with **P2**. On the other hand, as mentioned in both the Introduction to this thesis as well as in Chapters 2 and 3, a key technique we used in engineering the requisite quantum states was that of postselecting on coincidence counts. By and large, postselection is a strange blend of postulates **P2** and **P3** and its inclusion in protocols is far from ideal. Studies into methods of generating more efficient sources of tailored, 'out-of-the-box' quantum states, such as pump shaping [32, 33], could potentially mitigate the need for postselection. However, barring better sources, are better measurement techniques possible which would forgo postselection? Would we even observe the same results without postselection? Is postselection a theoretical necessity?

In Chapter 3 we also discussed two techniques with which to perform the spatially-resolved measurement, namely the single-pixel scan and random mask scan. These methods both had their pros and cons, and it may be interesting to consider other techniques, such as those based on Hadamard matrices [185], in more detail within the context of ghost imaging. Finally, a deeper investigation into the subtleties between a two-particle quantum state's symmetry and its (in)distinguishability would also prove interesting. It is claimed that a HOM filter and postselection scheme only transmits the anti-symmetric portions of states [81]. However, a similar argument could be made that a HOM filter-postselection scheme registers distinguishable states and not indistinguishable ones. This difference may be important as two of the four Bell states ($|\Psi^{\pm}\rangle$) consist of particles with different quantum numbers and are hence distinguishable, yet one of these two is symmetric and the other anti-symmetric (the two $|\Phi^{\pm}\rangle$ Bell states are both indistinguishable and symmetric).

In Chapter 4 we changed tactics completely and outlined a novel model of quantum ghost imaging within the framework of quantum field theory. QFT is a more complete model of quantum mechanics than the usual framework used when studying quantum optics. However, it has some unwanted consequences. For example, it is impossible to define a position operator with all the required properties in QFT: attempts at doing so run into problems for massless particles of spin 1 or higher [186], and high energy calculations and experiments often tend to opt instead for the momentum representation. The Unruh-DeWitt detector model is perhaps one way to work around these problems. In our case, we used UDW detectors as analogies for both the ghost

object as well as the detection system. In doing so, we found that it should be possible to describe ghost imaging, and by extension other quantum photonics experiments too, using such techniques. However, the contrasts and intensities arrived at were quite small and so the next obvious step would be to improve the model to increase these values and perhaps make it more readily experimentally testable. Indeed, one could perform the calculations in the perturbative regime rather than the non-perturbative one we considered. This would complicate the mathematics in that the time-ordering operator in the Dyson series would now have a nontrivial effect on the results. Any results arrived at would also not be exact. However, such an approach would allow one to generalise the formulae of Chapter 4 to different switching functions, potentially resulting in stronger and longer coupling between the entangled scalar field and the detectors.

Another interesting study may be to consider higher-dimensional detectors, since usual UDW detectors are simply two-level first-quantised systems. This corresponds to the binary images we used as well as binary detection events (i.e. you either detect something or you don't). One could conceivably model detectors with more than two levels however, and using these should allow us to generalise the simulations to non-binary images as well as more complicated models of experimental detectors. Finally, further studies into the theoretical underpinnings of this detector model and, in particular, its potential in discriminating the orbital angular momentum of photons (or any relevant particle) would align well with the common OAM techniques increasingly being employed in higher-dimensional quantum photonics studies. A key assumption in the derivation of the UDW interaction Hamiltonian is that no orbital angular momentum be transferred between the detectors and the particles being probed [46, 187]. As such, it is hence unclear whether this model could be made useful for the study of OAM, but answering this question definitively would still be interesting.

Finally, in Chapter 5 we studied a new type of quantum random number generator which uses the OAM spectrum of down-converted photons as the source of entropy. This is the first demonstration of a QRNG which exploits this degree of freedom. First, we detailed how one can use a SLM in place of a traditional beamsplitter in a path-information QRNG to both tailor the probability distribution of the system to any one we wish as well as account for experimental imperfections in the transmission and detection sections of the setup. This is interesting as a SLM is an easy to use, relatively fast device allowing for both the easy digital control of a system and allowing us to forgo other usual static optical components. However, the main result was the demonstration of the system in generating random bit strings in both a two- and a

three-dimensional case. The experimental entropies obtained were extremely close to their theoretical maxima, which demonstrates the potential of the system. Finally, in the three-dimensional case, more than one bit of entropy was extracted per detection event.

Three potential next steps come to mind. First, it would be interesting to experimentally study how much one could push such a system to extract very high-dimensional multibits. Indeed, increasing the dimension of the measured state's Hilbert space is an efficient way of increasing the efficiency of a QRNG. Second, the current protocol generated the random bits after having collected all the measurements, whereas it would be useful to be able to generate higher-dimensional random bits in real time. This should be possible using more sophisticated equipment such as a more intense down-conversion source, an ICCD and an OAM mode sorter. This is an avenue we are currently investigating. Finally, many detection devices nowadays are capable of discriminating multiple different photon degrees of freedom simultaneously. For example, the aforementioned mode sorter/ICCD detection system should be sensitive to both the particle number as well as the OAM charge of an incident photon state. The theoretical techniques needed to simultaneously consider different degrees of freedom of entangled photon states have recently been developed (see [188, 189]). Adapting our experimental system to include such equipment would give one access to a much larger composite Hilbert space (**P4**) from which to extract entropy and potentially greatly increase the random bit generation rate of the QRNG.

Clearly the work presented in this thesis is but a small addition to our understanding of quantum mechanics. However, despite the tremendous advances made in understanding it and, by extension, Nature, over the past century or so, it is clear that many exciting discoveries remain before we can fully understand and appreciate one of science's great theories.

References

[1] M. A. Nielsen and I. Chuang. *Quantum computation and quantum information*. 10th Anniversary ed. Cambridge University Press, 2011.

[2] N. Bohr. Über die Serienspektra der Elemente. *Zeitschrift für Physik* 2.5 (1920), pp. 423–469.

[3] G. Jaeger. What in the (quantum) world is macroscopic? *American Journal of Physics* 82.9 (2014), pp. 896–905.

[4] S. Deffner and S. Campbell. *Quantum thermodynamics*. 2053-2571. Morgan & Claypool Publishers, 2019.

[5] M. E. Peskin and D. V. Schroeder. *An introduction to quantum field theory*. Advanced book classics. Avalon Publishing, 1995.

[6] C. E. Shannon. A mathematical theory of communication. *Bell System Technical Journal* 27.3 (1948), pp. 379–423.

[7] C. H. Bennett and G. Brassard. Quantum cryptography: public key distribution and coin tossing. *Theoretical Computer Science* 560.12 (2014), pp. 7–11.

[8] A. K. Ekert. Quantum cryptography based on Bell's theorem. *Physical Review Letters* 67.6 (1991), p. 661.

[9] C. H. Bennett et al. Teleporting an unknown quantum state via dual classical and Einstein-Podolsky-Rosen channels. *Physical Review Letters* 70 (13 1993), p. 1895.

[10] D. Bouwmeester et al. Experimental quantum teleportation. *Nature* 390.6660 (1997), pp. 575–579.

[11] V. Giovannetti, S. Lloyd, and L. Maccone. Advances in quantum metrology. *Nature Photonics* 5.4 (2011), p. 222.

[12] P. W. Shor. "Algorithms for quantum computation: discrete logarithms and factoring". *Proceedings 35th Annual Symposium on Foundations of Computer Science*. IEEE. 1994, pp. 124–134.

[13] L. K. Grover. "A fast quantum mechanical algorithm for database search". *Proceedings of the twenty-eighth annual ACM symposium on Theory of Computing*. 1996, pp. 212–219.

[14] Y. Cao, J. Romero, and A. Aspuru-Guzik. Potential of quantum computing for drug discovery. *IBM Journal of Research and Development* 62.6 (2018), pp. 6–1.

[15] R. Orus, S. Mugel, and E. Lizaso. Quantum computing for finance: overview and prospects. *Reviews in Physics* 4 (2019), p. 100028.

[16] S. J. van Enk, H. J. Kimble, and H. Mabuchi. Quantum information processing in cavity-QED. *Quantum Information Processing* 3.1-5 (2004), pp. 75–90.

[17] J. I. Cirac and P. Zoller. Quantum computations with cold trapped ions. *Physical Review Letters* 74.20 (1995), p. 4091.

[18] N. A. Gershenfeld and I. L. Chuang. Bulk spin-resonance quantum computation. *Science* 275.5298 (1997), pp. 350–356.

[19] F. Bouchard et al. Experimental investigation of high-dimensional quantum key distribution protocols with twisted photons. *Quantum* 2 (2018), p. 111.

[20] E. Knill, R. Laflamme, and G. J. Milburn. A scheme for efficient quantum computation with linear optics. *Nature* 409.6816 (2001), pp. 46–52.

[21] R. Raussendorf and H. J. Briegel. A one-way quantum computer. *Physical Review Letters* 86.22 (2001), p. 5188.

[22] M. A. Nielsen. Optical quantum computation using cluster states. *Physical Review Letters* 93.4 (2004), p. 040503.

[23] J. L. O'brien. Optical quantum computing. *Science* 318.5856 (2007), pp. 1567–1570.

[24] J. H. Shapiro and R. W. Boyd. The physics of ghost imaging. *Quantum Information Processing* 11.4 (2012), pp. 949–993.

[25] A. Acín and L. Masanes. Certified randomness in quantum physics. *Nature* 540.7632 (2016), pp. 213–219.

[26] X. Ma et al. Quantum random number generation. *npj Quantum Information* 2.1 (2016), pp. 1–9.

[27] B. S. Philippe Grangier and J. Vuckovic. Focus on single photons on demand. *New Journal of Physics* 6.E04 (2004).

[28] J. Beugnon et al. Quantum interference between two single photons emitted by independently trapped atoms. *Nature* 440.7085 (2006), pp. 779–782.

[29] D. C. Burnham and D. L. Weinberg. Observation of simultaneity in parametric production of optical photon pairs. *Physical Review Letters* 25 (2 1970), p. 84.

[30] Y. Shih. *An introduction to quantum optics: photon and biphoton physics*. Series in Optics and Optoelectronics. Taylor & Francis, 2011.

[31] L. Allen, M. J. Padgett, and M. Babiker. "IV) The orbital angular momentum of light". *Progress in Optics*. Vol. 39. Elsevier, 1999, pp. 291–372.

[32] A. M. Yao. Angular momentum decomposition of entangled photons with an arbitrary pump. *New Journal of Physics* 13.5 (2011), p. 053048.

[33] E. V. Kovlakov, S. S. Straupe, and S. P. Kulik. Quantum state engineering with twisted photons via adaptive shaping of the pump beam. *Physical Review A* 98.6 (2018), p. 060301.

[34] V. I. Yukalov. Basics of Bose-Einstein condensation. *Physics of Particles and Nuclei* 42.3 (2011), pp. 460–513.

[35] J. Bardeen, L. N. Cooper, and J. R. Schrieffer. Theory of superconductivity. *Physical Review* 108.5 (1957), p. 1175.

[36] R. H. Fowler. On Dense Matter. *Monthly Notices of the Royal Astronomical Society* 87 (1926), pp. 114–122.

[37] N. Bornman et al. Ghost imaging using entanglement-swapped photons. *npj Quantum Information* 5.1 (2019), pp. 1–6.

[38] N. Bornman et al. Ghost imaging with engineered quantum states by Hong-Ou-Mandel interference. *New Journal of Physics* 21.7 (2019), p. 073044.

[39] C.-K. Hong, Z.-Y. Ou, and L. Mandel. Measurement of subpicosecond time intervals between two photons by interference. *Physical Review Letters* 59.18 (18 1987), p. 2044.

[40] M. Schlosshauer. Decoherence, the measurement problem, and interpretations of quantum mechanics. *Reviews of Modern Physics* 76.4 (2005), p. 1267.

[41] D. R. Terno. Introduction to relativistic quantum information. *Quantum Information Processing: From Theory to Experiment* 199 (2006), p. 61.

[42] R. B. Mann and T. C. Ralph. Relativistic quantum information. *Classical and Quantum Gravity* 29.22 (2012), p. 220301.

[43] W. G. Unruh. Notes on black-hole evaporation. *Physical Review D* 14 (4 1976), p. 870.

[44] S. Hawking and W. Israel. *General relativity: an Einstein centenary survey*. Cambridge University Press, 2010.

[45] B. L. Hu, A. Roura, and S. Shresta. Vacuum fluctuations and moving atoms/detectors: from the Casimir-Polder to the Unruh-Davies-DeWitt-Fulling effect. *Journal of Optics B: Quantum and Semiclassical Optics* 6.8 (2004), S698.

[46] Á. M. Alhambra, A. Kempf, and E. Martín-Martínez. Casimir forces on atoms in optical cavities. *Physical Review A* 89.3 (2014), p. 033835.

[47] N. Bornman, A. Kempf, and A. Forbes. Quantum imaging using relativistic detectors. *Physical Review D* 100.12 (2019), p. 125004.

[48] M. de Oliveira, N. Bornman, and A. Forbes. Holographically controlled random numbers from entangled twisted photons. *Physical Review A* 102.3 (2020), p. 032620.

[49] T. N. Palmer et al. Representing model uncertainty in weather and climate prediction. *Annual Review of Earth and Planetary Sciences* 33 (2005), pp. 163–193.

[50] N. Bornman, A. Forbes, and A. Kempf. Random number generation & distribution out of thin (or thick) air. *Journal of Optics* 22.7 (2020), p. 075705.

[51] M. Jeanblanc, M. Yor, and M. Chesney. *Mathematical methods for financial markets*. Springer Science & Business Media, 2009.

[52] Y. Dodis et al. "On the (im)possibility of cryptography with imperfect randomness". *45th Annual IEEE Symposium on Foundations of Computer Science*. IEEE. 2004, pp. 196–205.

[53] W. M. De Muynck. Distinguishable- and indistinguishable-particle descriptions of systems of identical particles. *International Journal of Theoretical Physics* 14.5 (1975), pp. 327–346.

[54] J. Wang et al. Terabit free-space data transmission employing orbital angular momentum multiplexing. *Nature Photonics* 6 (2012), p. 488.

[55] M. Mafu et al. Higher-dimensional orbital-angular-momentum-based quantum key distribution with mutually unbiased bases. *Physical Review A* 88 (3 2013), p. 032305.

[56] M. Mirhosseini et al. High-dimensional quantum cryptography with twisted light. *New Journal of Physics* 17.3 (2015), p. 033033.

[57] A. C. Dada et al. Experimental high-dimensional two-photon entanglement and violations of generalized Bell inequalities. *Nature Physics* 7.9 (2011), pp. 677–680.

[58] M. Zukowski et al. "Event-ready-detectors" Bell experiment via entanglement swapping. *Physical Review Letters* 71 (26 1993), pp. 4287–4290.

[59] J.-W. Pan et al. Experimental entanglement swapping: entangling photons that never interacted. *Physical Review Letters* 80 (18 1998), pp. 3891–3894.

[60] Y. Zhang et al. Simultaneous entanglement swapping of multiple orbital angular momentum states of light. *Nature Communications* 8.1 (2017), p. 632.

[61] X.-L. Wang et al. Quantum teleportation of multiple degrees of freedom of a single photon. *Nature* 518 (2015), p. 516.

[62] T. B. Pittman et al. Optical imaging by means of two-photon quantum entanglement. *Physical Review A* 52.5 (5 1995), R3429.

[63] R. S. Bennink, S. J. Bentley, and R. W. Boyd. "Two-photon" coincidence imaging with a classical source. *Physical Review Letters* 89.11 (2002), p. 113601.

[64] R. S. Bennink et al. Quantum and classical coincidence imaging. *Physical Review Letters* 92.3 (2004), p. 033601.

[65] A. Valencia et al. Two-photon imaging with thermal light. *Physical Review Letters* 94.6 (2005), p. 063601.

[66] J. C. Howell et al. Realization of the Einstein-Podolsky-Rosen paradox using momentum-and position-entangled photons from spontaneous parametric down conversion. *Physical Review Letters* 92.21 (2004), p. 210403.

[67] B. Jack et al. Holographic ghost imaging and the violation of a Bell inequality. *Physical Review Letters* 103.8 (2009), p. 083602.

[68] L. Chen, J. Lei, and J. Romero. Quantum digital spiral imaging. *Light: Science & Applications* 3.3 (2014), e153.

[69] P. Ryczkowski et al. Ghost imaging in the time domain. *Nature Photonics* 10.3 (2016), p. 167.

[70] J. H. Shapiro. Computational ghost imaging. *Physical Review A* 78.6 (2008), p. 061802.

[71] B. I. Erkmen and J. H. Shapiro. Ghost imaging: from quantum to classical to computational. *Advances in Optics and Photonics* 2.4 (2010), pp. 405–450.

[72] Y. Altmann et al. Quantum-inspired computational imaging. *Science* 361.6403 (2018).

[73] O. Katz, Y. Bromberg, and Y. Silberberg. Compressive ghost imaging. *Applied Physics Letters* 95.13 (2009), p. 131110.

[74] K. W. C. Chan, M. N. O'Sullivan, and R. W. Boyd. Two-color ghost imaging. *Physical Review A* 79.3 (2009), p. 033808.

[75] S. Karmakar and Y. Shih. Two-color ghost imaging with enhanced angular resolving power. *Physical Review A* 81.3 (2010), p. 033845.

[76] C. Simon. Towards a global quantum network. *Nature Photonics* 11.11 (2017), p. 678.

[77] H. Rubinsztein-Dunlop et al. Roadmap on structured light. *Journal of Optics* 19.1 (2016), p. 013001.

[78] C. Rosales-Guzman and A. Forbes. *How to shape light with spatial light modulators*. SPIE Spotlight. SPIE Press, 2017.

[79] A. Forbes, A. Dudley, and M. McLaren. Creation and detection of optical modes with spatial light modulators. *Advances in Optics and Photonics* 8.2 (2016), pp. 200–227.

[80] A. Fedrizzi et al. Anti-symmetrization reveals hidden entanglement. *New Journal of Physics* 11.10 (2009), p. 103052.

[81] Y. Zhang et al. Engineering two-photon high-dimensional states through quantum interference. *Science Advances* 2.2 (2016), e1501165.

[82] S. P. Walborn et al. Multimode Hong-Ou-Mandel interference. *Physical Review Letters* 90.14 (2003), p. 143601.

[83] L. Kai-Hong et al. Nonlocal imaging by conditional averaging of random reference measurements. *Chinese Physics Letters* 29.7 (2012), p. 074216.

[84] J. Wen. Forming positive-negative images using conditioned partial measurements from reference arm in ghost imaging. *Journal of the Optical Society of America A* 29.9 (2012), pp. 1906–1911.

[85] G. Barreto-Lemos et al. Quantum imaging with undetected photons. *Nature (London)* 512 (2014), p. 409.

[86] J. Liu et al. Studying fermionic ghost imaging with independent photons. *Optics Express* 24.25 (2016), pp. 29226–29236.

[87] J. Calsamiglia. Generalized measurements by linear elements. *Physical Review A* 65 (3 2002), p. 030301.

[88] J. Calsamiglia and N. Lütkenhaus. Maximum efficiency of a linear-optical Bell-state analyzer. *Applied Physics B* 72.1 (2001), pp. 67–71.

[89] A. Forbes and I. Nape. Quantum mechanics with patterns of light: progress in high dimensional and multidimensional entanglement with structured light. *AVS Quantum Science* 1.1 (2019), p. 011701.

[90] S. K. Goyal et al. Qudit-teleportation for photons with linear optics. *Scientific Reports* 4 (2014), p. 4543.

[91] S. P. Walborn et al. Spatial correlations in parametric down-conversion. *Physics Reports* 495.4-5 (2010), pp. 87–139.

[92] A. Gatti et al. Ghost imaging with thermal light: comparing entanglement and classical correlation. *Physical Review Letters* 93.9 (2004), p. 093602.

[93] Y. Cai and S.-Y. Zhu. Ghost imaging with incoherent and partially coherent light radiation. *Physical Review E* 71.5 (2005), p. 056607.

[94] B. Sun et al. 3D computational imaging with single-pixel detectors. *Science* 340.6134 (2013), pp. 844–847.

[95] J. Cheng. Ghost imaging through turbulent atmosphere. *Optics Express* 17.10 (2009), pp. 7916–7921.

[96] P.-A. Moreau et al. Imaging with quantum states of light. *Nature Reviews Physics* 1.1 (2019), pp. 367–380.

[97] Y. Zhang et al. Hong-Ou-Mandel interference of entangled Hermite-Gauss modes. *Physical Review A* 94.3 (2016), p. 033855.

[98] W. L. Chan et al. A single-pixel terahertz imaging system based on compressed sensing. *Applied Physics Letters* 93.12 (2008), p. 121105.

[99] D. L. Donoho. Compressed sensing. *IEEE Transactions on Information Theory* 52.4 (2006), pp. 1289–1306.

[100] M.-J. Sun et al. Improving the signal-to-noise ratio of single-pixel imaging using digital microscanning. *Optics Express* 24.10 (2016), pp. 10476–10485.

[101] G. M. D'Ariano, M. G. A. Paris, and M. F. Sacchi. Quantum tomography. *Advances in Imaging and Electron Physics* 128 (2003), pp. 206–309.

[102] B. Tamir and E. Cohen. Introduction to weak measurements and weak values. *Quanta* 2.1 (2013), pp. 7–17.

[103] W. H. Zurek. Decoherence, einselection, and the quantum origins of the classical. *Reviews of Modern Physics* 75 (3 2003), pp. 715–775.

[104] J. Doukas and L. C. L. Hollenberg. Loss of spin entanglement for accelerated electrons in electric and magnetic fields. *Physical Review A* 79 (5 2009), p. 052109.

[105] R. Lopp, E. Martin-Martinez, and D. N. Page. Relativity and quantum optics: accelerated atoms in optical cavities. *Classical and Quantum Gravity* 35.22 (2018), p. 224001.

[106] D. R. Terno. Localization of relativistic particles and uncertainty relations. *Physical Review A* 89 (4 2014), p. 042111.

[107] E. Martin-Martinez. Causality issues of particle detector models in QFT and quantum optics. *Physical Review D* 92 (10 2015), p. 104019.

[108] E. T. Jaynes and F. W. Cummings. Comparison of quantum and semiclassical radiation theories with application to the beam maser. *Proceedings of the IEEE* 51.1 (1963), pp. 89–109.

[109] J. K. Andrew D. Greentree and J. Larson. Fifty years of Jaynes-Cummings physics. *J. Phys. B: At. Mol. Opt. Phys.* 46 (2013), p. 220201.

[110] D. Faccio. Laser pulse analogues for gravity and analogue Hawking radiation. *Contemporary Physics* 53.2 (2012), pp. 97–112.

[111] F. Belgiorno et al. Hawking radiation from ultrashort laser pulse filaments. *Physical Review Letters* 105.20 (2010), p. 203901.

[112] P. Simidzija and E. Martin-Martinez. All coherent field states entangle equally. *Physical Review D* 96.2 (2017), p. 025020.

[113] P. Simidzija and E. Martin-Martinez. Non-perturbative analysis of entanglement harvesting from coherent field states. *Physical Review D* 96.6 (2017), p. 065008.

[114] C. M. Natarajan, M. G. Tanner, and R. H. Hadfield. Superconducting nanowire single-photon detectors: physics and applications. *Superconductor Science and Technology* 25.6 (2012), p. 063001.

[115] B. Hall and B. C. Hall. *Lie groups, Lie algebras, and representations: an elementary introduction*. Graduate Texts in Mathematics. Springer, 2003.

[116] Z. Yang, M. Liscidini, and J. E. Sipe. Spontaneous parametric down-conversion in waveguides: a backward Heisenberg picture approach. *Physical Review A* 77 (3 2008), p. 033808.

[117] G. Vidal and R. F. Werner. Computable measure of entanglement. *Physical Review A* 65 (3 2002), p. 032314.

[118] H. Ollivier and W. H. Zurek. Quantum discord: a measure of the quantumness of correlations. *Physical Review Letters* 88 (2001), p. 017901.

[119] S. Luo. Quantum discord for two-qubit systems. *Physical Review A* 77.4 (2008), p. 042303.

[120] M. Ali, A. R. P. Rau, and G. Alber. Quantum discord for two-qubit X states. *Physical Review A* 81.4 (2010), p. 042105.

[121] D. E. Bruschi, I. Fuentes, and J. Louko. Voyage to Alpha Centauri: entanglement degradation of cavity modes due to motion. *Physical Review D* 85 (6 2012), 061701(r).

[122] Y. Dai, Z. Shen, and Y. Shi. Killing quantum entanglement by acceleration or a black hole. *Journal of High Energy Physics* 2015.9 (2015), p. 71.

[123] S. M. Carroll. *Spacetime and geometry: an introduction to general relativity*. Addison Wesley, 2004.

[124] D. Hummer, E. Martin-Martinez, and A. Kempf. Renormalized Unruh-DeWitt particle detector models for boson and fermion fields. *Physical Review D* 93 (2 2016), p. 024019.

[125] A. Pozas-Kerstjens and E. Martín-Martínez. Harvesting correlations from the quantum vacuum. *Physical Review D* 92 (6 2015), p. 064042.

[126] M. Aspelmeyer et al. Long-distance quantum communication with entangled photons using satellites. *IEEE Journal of Selected Topics in Quantum Electronics* 9.6 (2003), pp. 1541–1551.

[127] M. Erhard et al. Twisted photons: new quantum perspectives in high dimensions. *Light: Science & Applications* 7.3 (2018), p. 17146.

[128] F. Tamburini et al. Twisting of light around rotating black holes. *Nature Physics* 7.3 (2011), p. 195.

[129] R. Graham and S. Butler. *Rudiments of Ramsey theory*. Vol. 123. American Mathematical Society, 2015.

[130] N. Gisin et al. Quantum cryptography. *Reviews of Modern Physics* 74.1 (2002), p. 145.

[131] N. Metropolis and S. Ulam. The Monte Carlo method. *Journal of the American statistical association* 44.247 (1949), pp. 335–341.

[132] R. Y. Rubinstein and D. P. Kroese. *Simulation and the Monte Carlo method*. Vol. 10. John Wiley & Sons, 2016.

[133] A. Schiffler. Physical entropy in computer games. *Technoetic Arts* 8.1 (2010), pp. 39–45.

[134] J. von Neumann. "Various techniques used in connection with random digits". *Monte Carlo Method*. Ed. by A. S. Householder, G. E. Forsythe, and H. H. Germond. Vol. 12. National Bureau of Standards Applied Mathematics Series. Washington, DC: US Government Printing Office, 1951. Chap. 13, pp. 36–38.

[135] A. Einstein, B. Podolsky, and N. Rosen. Can quantum-mechanical description of physical reality be considered complete? *Physical Review* 47.10 (10 1935), p. 777.

[136] J. S. Bell. *Speakable and unspeakable in quantum mechanics: collected papers on quantum philosophy*. Cambridge University Press, 2004.

[137] M. Born. Statistical interpretation of quantum mechanics. *Science* 122.3172 (1955), pp. 675–679.

[138] A. Marandi et al. All-optical quantum random bit generation from intrinsically binary phase of parametric oscillators. *Optics Express* 20.17 (2012), pp. 19322–19330.

[139] M. J. Collins et al. Random number generation from spontaneous Raman scattering. *Applied Physics Letters* 107.14 (2015), p. 141112.

[140] C. R. S. Williams et al. Fast physical random number generator using amplified spontaneous emission. *Optics Express* 18.23 (2010), pp. 23584–23597.

[141] A. Argyris et al. Sub-Tb/s physical random bit generators based on direct detection of amplified spontaneous emission signals. *Journal of Lightwave Technology* 30.9 (2012), pp. 1329–1334.

[142] B. Qi et al. High-speed quantum random number generation by measuring phase noise of a single-mode laser. *Optics Letters* 35.3 (2010), pp. 312–314.

[143] M. Jofre et al. True random numbers from amplified quantum vacuum. *Optics Express* 19.21 (2011), pp. 20665–20672.

[144] C. H. Vincent. The generation of truly random binary numbers. *Journal of Physics E: Scientific Instruments* 3.8 (1970), p. 594.

[145] M. P. Silverman et al. Tests for randomness of spontaneous quantum decay. *Physical Review A* 61.4 (2000), p. 042106.

[146] H.-Q. Ma, Y. Xie, and L.-A. Wu. Random number generation based on the time of arrival of single photons. *Applied Optics* 44.36 (2005), pp. 7760–7763.

[147] M. Stipčević and B. M. Rogina. Quantum random number generator based on photonic emission in semiconductors. *Review of Scientific Instruments* 78.4 (2007), p. 045104.

[148] M. Herrero-Collantes and J. C. Garcia-Escartin. Quantum random number generators. *Reviews of Modern Physics* 89.1 (2017), p. 015004.

[149] L. Masanes, A. Acin, and N. Gisin. General properties of nonsignaling theories. *Physical Review A* 73.1 (2006), p. 012112.

[150] M. Fiorentino et al. Secure self-calibrating quantum random-bit generator. *Physical Review A* 75.3 (2007), p. 032334.

[151] M. A. Wayne et al. Photon arrival time quantum random number generation. *Journal of Modern Optics* 56.4 (2009), pp. 516–522.

[152] T. Jennewein et al. A fast and compact quantum random number generator. *Review of Scientific Instruments* 71.4 (2000), pp. 1675–1680.

[153] M. Ren et al. Quantum random-number generator based on a photon-number-resolving detector. *Physical Review A* 83.2 (2011), p. 023820.

[154] N. Nisan and D. Zuckerman. Randomness is linear in space. *Journal of Computer and System Sciences* 52.1 (1996), pp. 43–52.

[155] H.-K. Lo, H. F. Chau, and M. Ardehali. Efficient quantum key distribution scheme and a proof of its unconditional security. *Journal of Cryptology* 18.2 (2005), pp. 133–165.

[156] M. Xu et al. Adjustable unbalanced quantum random-number generator. *Chinese Optics Letters* 13.2 (2015), pp. 021405–021405.

[157] Q. Yan et al. Multi-bit quantum random number generation by measuring positions of arrival photons. *Review of Scientific Instruments* 85.10 (2014), p. 103116.

[158] A. Sarkar and C. M. Chandrashekar. Multi-bit quantum random number generation from a single qubit quantum walk. *Scientific Reports* 9.1 (2019), pp. 1–11.

[159] M. Erhard, M. Krenn, and A. Zeilinger. Advances in high-dimensional quantum entanglement. *Nature Reviews Physics* (2020), pp. 1–17.

[160] T. Symul, S. M. Assad, and P. K. Lam. Real time demonstration of high bitrate quantum random number generation with coherent laser light. *Applied Physics Letters* 98.23 (2011), p. 231103.

[161] A. Rukhin et al. *NIST special publication 800-22 1a: a statistical suite for random and pseudorandom number generators for cryptographic applications*. Tech. rep. National Institute of Standards and Technology, U.S. Department of Commerce, 2010.

[162] M. Li and P. Vitányi. *An introduction to Kolmogorov complexity and its applications*. Vol. 3. Springer, 2008.

[163] I. Goodfellow, Y. Bengio, and A. Courville. *Deep learning*. MIT press, 2016.

[164] J. von Neumann. *Mathematische Grundlagen der Quantenmechanik*. Julius Springer, 1932.

[165] U. M. Maurer. A universal statistical test for random bit generators. *Journal of Cryptology* 5.2 (1992), pp. 89–105.

[166] J. Soto. "Statistical testing of random number generators". *Proceedings of the 22nd National Information Systems Security Conference*. Vol. 10. NIST Gaithersburg, MD. 1999, p. 12.

[167] J. Walker. ENT: a pseudorandom number sequence test program. *Available at www.fourmilab.ch/random/S* (2008).

[168] R. G. Brown, D. Eddelbuettel, and D. Bauer. Dieharder: a random number test suite. *Open Source software library under development, available at: www.phy.duke.edu/˜rgb/General/dieharder.php* (2013).

[169] K. Marton et al. Generation and testing of random numbers for cryptographic applications. *Proceedings of the Romanian Academy - Series A* 13.4 (2012), pp. 368–377.

[170] A. Forbes. *Laser beam propagation: generation and propagation of customized light*. CRC Press, 2014.

[171] F. M. Miatto, A. M. Yao, and S. M. Barnett. Full characterization of the quantum spiral bandwidth of entangled biphotons. *Physical Review A* 83.3 (2011), p. 033816.

[172] A. Mair et al. Entanglement of the orbital angular momentum states of photons. *Nature* 412.6844 (2001), pp. 313–316.

[173] E. Karimi et al. Radial quantum number of Laguerre-Gauss modes. *Physical Review A* 89.6 (2014), p. 063813.

[174] E. Toninelli et al. Concepts in quantum state tomography and classical implementation with intense light: a tutorial. *Advances in Optics and Photonics* 11.1 (2019), pp. 67–134.

[175] C. K. Hong and L. Mandel. Experimental realization of a localized one-photon state. *Physical Review Letters* 56.1 (1986), p. 58.

[176] D. G. Marangon et al. Enhanced security for multi-detector quantum random number generators. *Quantum Science and Technology* 1.1 (2016), p. 015005.

[177] G. C. G. Berkhout et al. Efficient sorting of orbital angular momentum states of light. *Physical Review Letters* 105.15 (2010), p. 153601.

[178] G. Ruffato et al. A compact diffractive sorter for high-resolution demultiplexing of orbital angular momentum beams. *Scientific Reports* 8.1 (2018), pp. 1–12.

[179] G. Molina-Terriza, J. P. Torres, and L. Torner. Management of the angular momentum of light: preparation of photons in multidimensional vector states of angular momentum. *Physical Review Letters* 88.1 (2001), p. 013601.

[180] J. P. Torres et al. Preparation of engineered two-photon entangled states for multidimensional quantum information. *Physical Review A* 67.5 (2003), p. 052313.

[181] I. G. Kaplan. *The Pauli exclusion principle: origin, verifications, and applications*. John Wiley & Sons, 2017.

[182] J. R. Schrieffer. *Theory of superconductivity*. CRC Press, 2018.

[183] R. K. Pathria and P. D. Beale. *Statistical mechanics*. Academic Press, 2011.

[184] M. P. Edgar et al. Imaging high-dimensional spatial entanglement with a camera. *Nature Communications* 3.1 (2012), pp. 1–6.

[185] Z. Zhang et al. Hadamard single-pixel imaging versus Fourier single-pixel imaging. *Optics Express* 25.16 (2017), pp. 19619–19639.

[186] T. D. Newton and E. P. Wigner. Localized states for elementary systems. *Reviews of Modern Physics* 21 (3 1949), p. 400.

[187] E. Martín-Martínez, M. Montero, and M. del Rey. Wavepacket detection with the Unruh-DeWitt model. *Physical Review D* 87 (6 2013), p. 064038.

[188] F. S. Roux. Combining spatiotemporal and particle-number degrees of freedom. *Physical Review A* 98.4 (2018), p. 043841.

[189] F. S. Roux. Quantifying entanglement of parametric down-converted states in all degrees of freedom. *Physical Review Research* 2.2 (2020), p. 023137.

Appendix A

Chapter 2 appendix

A.1 State projection theory

In this section of the Appendix we discuss the theoretical details which allowed us to arrive at the main results of Section 2.3 in Chapter 2. Specifically, we consider the state of photon D (and hence the ghost image), given an object in arm A, under various projections in arms B and C. In all cases we place a transmission mask (i.e. object) in path A where the transmission $O(i)$ of pixel i is equal to either 1 or 0. The set $\{O(i)\}$ hence contains all the information about the object. The effect of this mask is to modify the state of photon A according to

$$\hat{O}|r_i\rangle_A \rightarrow O(i)|r_i\rangle_A. \tag{A.1}$$

Therefore, losses associated with absorption (i.e. $O(i) = 0$) fall away. Furthermore, $\mathcal{B} = \sum_i O(i)$ is the total number of pixels in the object O with transmission equal to 1.

A.1.1 Projection onto $\{|\Psi^-_{nm}\rangle_{BC}\}$

Consider projection onto the states $\{|\Psi^-_{nm}\rangle_{BC}\}$, which includes terms which contribute to the coincidences between the two output ports of the BS. The overlap between $|\Psi^-_{nm}\rangle_{BC}$ and the initial state $|\varphi\rangle_{ABCD}$ is given by

$$
\begin{aligned}
|\varphi^-_{nm}\rangle_{AD} &= {}_{BC}\langle\Psi^-_{nm}|\varphi\rangle_{ABCD} \\
&= \sum_i \sum_j \frac{1}{\sqrt{2}d} |r_i\rangle_A |r_j\rangle_D \left[\delta_{i,n}\delta_{j,m} - \delta_{i,m}\delta_{j,n}\right] \\
&= \frac{1}{\sqrt{2}d}[|r_n\rangle_A |r_m\rangle_D - |r_m\rangle_A |r_n\rangle_D], \qquad \text{(A.2)}
\end{aligned}
$$

with δ the Kronecker delta. The projection on a single two-dimensional anti-symmetric state in paths B and C clearly leads to a pure anti-symmetric state in paths A and D. Furthermore, since $\{|\Psi^-_{nm}\rangle_{BC}\}$ is the only set of anti-symmetric states, projecting onto this set is equivalent to projecting onto anti-symmetric states in paths B-C and results in a mixture of two-dimensional entangled qubit states for photons A-D.

The state of photon D, conditioned on both object O in arm A as well as us having projected onto anti-symmetric states in paths B-C, is denoted by $\rho_{D|\Psi^-,A}$. This state, multiplied by both the probability of projecting onto an anti-symmetric Bell state $|\Psi^-\rangle$ (i.e. p_{Ψ^-}) and by the probability of photon A encountering a transparent pixel in the transmission mask object through which it passes (i.e. p_A), is given by

$$
\begin{aligned}
p_{\Psi^-} p_A \rho_{D|\Psi^-,A} &= \sum_{m,n,k} \langle r_k|_A O(k) |\varphi^-_{nm}\rangle_{AD} \langle\varphi^-_{nm}|_{AD} O(k) |r_k\rangle_A \\
&= \sum_{m,n,k} \frac{1}{2d^2} O^2(k) \left[\delta^2_{n,k} |r_m\rangle_D \langle r_m|_D + \delta^2_{m,k} |r_n\rangle_D \langle r_n|_D\right] \\
&= \frac{1}{2d^2} \sum_n \left[|r_n\rangle_D \langle r_n|_D \times \sum_{m\neq n} O(m)\right] \\
&= \frac{1}{2d^2} \left[\sum_n O(n)\mathbb{I} - \sum_n O(n) |r_n\rangle_D \langle r_n|_D\right] \\
&= \frac{1}{2d^2} \left[\mathcal{B}\mathbb{I} - \Lambda\right], \qquad \text{(A.3)}
\end{aligned}
$$

where $\Lambda = \sum_n O(n) |r_n\rangle_D \langle r_n|_D$ is a diagonal matrix with diagonal entries corresponding to either opaque ($O(i) = 0$) or transparent ($O(i) = 1$) pixels in the object. This can also be found by multiplying the three factors p_{Ψ^-}, p_A, and $\rho_{D|\Psi^-,A}$ directly, where

$$
p_{\Psi^-} = \frac{d-1}{2d}; \quad p_A = \frac{\mathcal{B}}{d}; \quad \rho_{D|\Psi^-,A} = \frac{\mathcal{B}\mathbb{I} - \Lambda}{\mathcal{B}(d-1)}. \qquad \text{(A.4)}
$$

Next, the ghost image in arm D is reconstructed from a set of intensities $\{I(i)\}$ with $I(i)$ being the probability of detecting a photon at pixel i. $I(i)$ can be experimentally

determined by, for example, placing a transmission mask in path D which only transmits photons through pixel i while blocking all other light, or, as we did, by performing a scanning protocol using SLM D. In the current Ψ^- projection case, the set of intensities is determined from Eq. A.3 as

$$I_{\Psi^-}(i) = \frac{\mathcal{B} - O(i)}{2d^2}. \tag{A.5}$$

This result predicts that the ghost image's contrast will be reversed with respect to the original object. In other words, if pixel i in the object is bright ($O(i) = 1$), the corresponding pixel will be darker in the ghost image, and vice versa. To quantify this, we define a normalised contrast value for the ghost image where the maximum and minimum pixel values are taken with respect to the original object and the sum of the pixel values is unity. In the current case, we have

$$\mathcal{C}_{\Psi^-} = \frac{\frac{\mathcal{B}-1}{2d^2} - \frac{\mathcal{B}}{2d^2}}{\mathcal{B}\left(\frac{\mathcal{B}-1}{2d^2}\right) + (d-\mathcal{B})\left(\frac{\mathcal{B}}{2d^2}\right)} = \frac{-1}{\mathcal{B}(d-1)}. \tag{A.6}$$

The overall minus sign above indicates the predicted contrast reversal.

A.1.2 Projection onto $\{|\Psi^+_{nm}\rangle_{BC}\}$

Next consider the case whereby we project onto the set of states $\{|\Psi^+_{nm}\rangle_{BC}\}$. The overlap between an element of this set and the initial state, namely ${}_{BC}\langle\Psi^+_{nm}|\varphi\rangle_{ABCD}$, is given by

$$|\varphi^+_{nm}\rangle_{AD} =_{BC} \langle\Psi^+_{nm}|\varphi\rangle_{ABCD} = \frac{1}{\sqrt{2}d}[|r_n\rangle_A|r_m\rangle_D + |r_m\rangle_A|r_n\rangle_D]. \tag{A.7}$$

Projecting onto the pure symmetric state $|\Psi^+_{nm}\rangle_{BC}$ gives a pure symmetric state in paths A and D. The full state, when projecting onto the entire set, is a mixture of symmetric, entangled two-qubit states.

Analogously to Eq. A.3, the state of photon D, namely $\rho_{D|\Psi^+,A}$ (now conditioned on us having projected onto the set of symmetric states $\{|\Psi^+_{nm}\rangle_{BC}\}$ in paths B-C), multiplied by both the probability of projecting onto $|\Psi^+\rangle$ (i.e. p_{Ψ^+}) as well as the probability p_A from before, gives

$$\begin{aligned} p_{\Psi^+}p_A\rho_{D|\Psi^+,A} &= \sum_{m,n,k} \langle r_k|_A O(k)|\varphi^+_{nm}\rangle_{AD}\langle\varphi^+_{nm}|_{AD}O(k)|r_k\rangle_A \\ &= \frac{1}{2d^2}\left[\mathcal{B}\mathbb{I} - \Lambda\right], \end{aligned} \tag{A.8}$$

which can also be factored

$$p_{\Psi^+} = \frac{d-1}{2d}; \quad p_A = \frac{\mathcal{B}}{d}; \quad \rho_{D|\Psi^+,A} = \frac{\mathcal{B}\mathbb{I} - \Lambda}{\mathcal{B}(d-1)}. \tag{A.9}$$

Interestingly, note that $\rho_{D|\Psi^+,A} = \rho_{D|\Psi^-,A}$. However, our scheme of postselecting on simultaneous photon detection events filters out all states but the anti-symmetric ones $\{|\Psi^-_{nm}\rangle_{BC}\}$. On the other hand, postselecting on the absence of simultaneous photon detection events would filter out the anti-symmetric states and leave behind only symmetric states, of which the set $\{|\Psi^+_{nm}\rangle_{BC}\}$ forms only part [80, 81, 82].

The set of pixel intensities in the current Ψ^+ case is found, from Eq. A.8, to be

$$I_{\Psi^+}(i) = \frac{\mathcal{B} - O(i)}{2d^2}. \tag{A.10}$$

Like before, the contrast of the ghost image is reversed with respect to that of the object and the normalised contrast value is identical to that in the Ψ^- case, i.e.

$$\mathcal{C}_{\Psi^+} = \frac{-1}{\mathcal{B}(d-1)}. \tag{A.11}$$

It should be noted that if one could postselect, in paths B and C, on only the current set of symmetric Bell-like states Ψ^+, we would also observe contrast-reversed ghost images when measuring the conditioned entangled state in paths A and D. However, our filtering/postselection scheme selects states based on their symmetry. The set of Ψ^+ states is but one, incomplete set of symmetric states. The final set $\{|\Phi_n\rangle_{BC}\}$ which we will consider below are also symmetric states, but would not give contrast-reversed ghost images.

A.1.3 Projection onto $\{|\Phi_n\rangle_{BC}\}$

Finally we move onto the set $\{|\Phi_n\rangle_{BC}\}$, where the overlap ${}_{BC}\langle\Phi_n|\varphi\rangle_{ABCD}$ is

$$|\varphi_n\rangle_{AD} =_{BC} \langle\Phi_n|\varphi\rangle_{ABCD} = \frac{1}{d}|r_n\rangle_A|r_n\rangle_D, \tag{A.12}$$

and so projecting onto the full set $\{|\Phi_n\rangle_{BC}\}$ leads to a mixture of pure symmetric states for photons A and D. Again, analogous with the previous two subsections, the conditioned state for photon D, namely $\rho_{D|\Phi,A}$, multiplied by both the probability of projecting onto $|\Phi\rangle$ (i.e. p_Φ) as well as p_A, is

$$p_\Phi p_A \rho_{D|\Phi,A} = \sum_{n,k} \langle r_k|_A O(k)|\varphi_n\rangle_{AD}\langle\varphi_n|_{AD} O(k)|r_k\rangle_A = \frac{1}{d^2}\Lambda, \tag{A.13}$$

which, factored, is

$$p_\Phi = \frac{1}{d}; \quad p_A = \frac{\mathcal{B}}{d}; \quad \rho_{D|\Phi,A} = \frac{\Lambda}{\mathcal{B}}. \tag{A.14}$$

The set of pixel intensities for this Φ case is

$$I_\Phi(i) = \frac{O(i)}{d^2}. \tag{A.15}$$

Notice that the ghost image here is not contrast reversed with respect to the original object as was the case previously: brighter pixels in the object will be brighter in the ghost image, and vice versa. When postselecting on anti-symmetric states, the contribution from these Φ states will mask the contrast reversal from the Ψ^+ states. Finally, the normalised contrast value for this case is given by

$$\mathcal{C}_\Phi = \frac{1}{\mathcal{B}}, \tag{A.16}$$

with the positive sign indicating no contrast reversal with respect to the original object.

A.1.4 Anti-symmetric vs. symmetric projections

We'll finally compare the reconstructed ghost image pixel intensities that we observe when postselecting on either symmetric or anti-symmetric states in paths B-C. In the anti-symmetric case, the intensity of pixel i in the ghost image is given by Eq. A.5, while it is given by a combination of Eqs. A.10 and A.15 in the symmetric case, such that

$$\text{Anti-symmetric } \{|\Psi^-\rangle\} \qquad I_{\text{AS}}(i) = \frac{\mathcal{B} - O(i)}{2d^2}, \tag{A.17}$$

$$\text{Symmetric } \{|\Psi^+\rangle, |\Phi\rangle\} \qquad I_{\text{S}}(i) = \frac{\mathcal{B} + O(i)}{2d^2}. \tag{A.18}$$

Note that if we were to project onto either symmetric (S) or anti-symmetric (AS) states together, the state of photon D would be proportional to the identity matrix. It would hence be maximally mixed and contain no information about the object. This can be seen by summing Eqs. A.3, A.8 and A.13, i.e.

$$\rho_{D|\text{AS},A} + \rho_{D|\text{S},A} \propto \mathbb{I}. \tag{A.19}$$

Finally, the normalised contrast values for projections onto all anti-symmetric and all symmetric states are given by

$$\mathcal{C}_{\mathrm{AS}} = \frac{-1}{\mathcal{B}(d-1)}; \quad \mathcal{C}_{\mathrm{S}} = \frac{1}{\mathcal{B}(d+1)}. \tag{A.20}$$

The factors of $1/\mathcal{B}$ are present as we chose to define the contrasts normalised with respect to the initial object; they would not be present if we were to normalise with respect the ghost image instead.

A.2 HOM results

The visibility of the HOM dip in Fig. 2.4, without any background count subtraction, is measured to be 0.56. This value is a result of both the anti-symmetric postselection scheme as well as the high background counts present in the experiment. Such background counts are caused by the large numerical aperture (of approximately 0.22) of the multi-mode fibres in paths B and C. Higher single photon detection events in paths B and C will give rise to more false four-fold coincidences which do not originate from actual correlated events. As such, roughly 25% of the recorded coincidence counts are from false background counts as well as up to 90% of the coincidences detected in the middle of the HOM dip. This has a significant deleterious effect on the dip's visibility. One could instead employ fibres with smaller cores as well as minimise external sources of infrared light in order to mitigate this and arrive at a more accurate visibility measurement.

A.3 Experimental setup discussion

While teleporting images through an entanglement swapping process is a necessary step for transmitting information across a quantum network, such four-photon experiments do present some challenges. Our experiment suffers from low count rates due in large part to us having measured a single pixel at a time. In the case of the two-pixel image, we can at best detect $p = 50\%$ of the total single counts at any one time; in the four-pixel case, that number is 25%. As this reduction occurs in both paths A and D and because the detection of these modes also reduces the counts in paths B and C by the same amount, we see a p^4 reduction in the four-fold coincidences with an increase in resolution. In the four-pixel case, this is a factor of 0.004. For this reason, increasing the resolution of the image makes it prohibitively time-consuming to obtain sufficient

counts. Furthermore, the theory for our experiment predicts a decreasing contrast with an increase in dimension d. Taken together, these aforementioned limitations make accessing higher-dimensional spaces difficult. However, we predict that these technical challenges can be overcome and that the observed contrast decrease with dimension can be ameliorated as outlined.

Appendix B

Chapter 3 appendix

B.1 Engineered ghost imaging experimental setup details

Consider the setup shown in Fig. 3.1 of Chapter 3. A mode-locked laser operating in the picosecond regime with an 80MHz pulse repetition rate, centred at 355nm with an average power of 350mW, is used to pump a 3-mm-long nonlinear, type-I β-barium borate (BBO) crystal. Degenerate, spatially-entangled photon pairs centred at 710nm (labelled A and B) are generated in the crystal by spontaneous parametric down-conversion (SPDC). The small difference in the angle of emission between the two photons (of around 3°) allows us to separate them with a simple D-shaped mirror. The photon in path A traverses two consecutive Dove prisms. One of them, which is fixed to a rotation mount, is rotated by an angle θ about the optical axis to introduce a specific phase between the spatial modes. Path B's length is adjusted to achieve HOM interference.

Paths A and B are then combined using a 50:50 beamsplitter (BS), the core element of the HOM filter. As discussed in the body of Chapter 3, only anti-symmetric input states will result in a single photon being emitted from each output port of the BS, and so an anti-symmetric state can be considered as having been created when the detection system is conditioned on coincidences. The symmetric states are tested by removing the BS. Next, the photons are directed to the ghost imaging section of the setup. The object and image arms are controlled using a single SLM encoded with amplitude and phase holograms (one half of the screen was used for the object and the other for the image). The plane of the crystal is imaged onto the SLM with a 5× magnification system (namely a $4f$-system with f1 = 100mm and f2 = 500mm, not

shown in Fig. 3.1) in both paths A and B. This gives a $\sim$ 5mm SPDC beam diameter at the SLM. The SLM plane is then imaged with a 375$\times$ de-magnification system (a $4f$-system with f3 = 750mm and f4 = 2mm, also not shown) onto couplers connected to few-mode fibres (FMFs). FMFs with $\sim 13\mu$m-core diameters are used to increase the collection area instead of using single-mode fibres with $\sim 5\mu$m cores. Multi-mode fibres with $\sim 62.5\mu$m cores were found to give images with too much noise. The SLM-FMF combination allows us to make joint projective measurements of particular spatial modes. Interference bandpass filters with bandwidths of 10nm are used prior to the FMFs, which are in turn connected to avalanche photodiodes to detect single photons. Coincidences are registered between the two paths using a PICOQUANT coincidence counter. The coincidence window is set to 12ns to minimise any possible accidental false positives from neighbouring electronic TTL pulses.

B.2 State symmetry under a basis change

A well-known result from high energy physics is that a change of basis does not change a state's symmetry. Here we outline a simple proof of this.

Let $\mathcal{H}_n := (V, \langle\cdot,\cdot\rangle)$ be a complex Hilbert space of dimension n and let the sets $\{u_1, u_2, \cdots, u_n\}$, $\{v_1, v_2, \cdots, v_n\}$ be two orthonormal bases of V. We define the linear 'change of basis' matrix operator M such that $Mu_i = v_i \ \forall\ i$. It is easy to see that M is then unitary, i.e. $\langle Mx, My\rangle = \langle x, y\rangle \ \forall\ x, y \in V$. Indeed, let $x = \sum_{i=1}^n \alpha_i u_i$, $y = \sum_{j=1}^n \beta_j u_j$ be arbitrary vectors. Then

$$\langle x, y\rangle = \sum_{i,j} \alpha_i \overline{\beta}_j \langle u_i, u_j\rangle = \sum_{i=1}^{n} \alpha_i \overline{\beta}_i, \tag{B.1}$$

$$\langle Mx, My\rangle = \sum_{i,j} \alpha_i \overline{\beta}_j \langle Mu_i, Mu_j\rangle = \sum_{i,j} \alpha_i \overline{\beta}_j \langle v_i, v_j\rangle = \sum_{i=1}^{n} \alpha_i \overline{\beta}_i. \tag{B.2}$$

The converse (i.e. that a unitary matrix is a change of basis matrix) can be shown too: let U be a unitary matrix, let $\{|u_i\rangle\}$ be an orthonormal basis, and define $|t_i\rangle := U|u_i\rangle$ for all i. Then $\langle t_i|t_j\rangle = \langle u_i|U^\dagger U|u_j\rangle = \langle u_i|u_j\rangle = \delta_{i,j}$, so $\{|t_i\rangle\}$ is an orthonormal basis too. Therefore, given a matrix U, U is unitary iff U represents a change of basis.

Next, let $\mathcal{H}_A, \mathcal{H}_B$ be Hilbert spaces of dimension n and m and let $\{|i\rangle_A\}, \{|j\rangle_B\}$ be respective orthonormal bases. Any arbitrary (anti-)symmetric state $|\Psi\rangle \in \mathcal{H}_A \otimes \mathcal{H}_B$ can be written as

$$|\Psi\rangle = \sum_{i=1}^{n}\sum_{j=1}^{m} a_i b_j \left(|i\rangle_A|j\rangle_B + \nu|j\rangle_A|i\rangle_B\right), \tag{B.3}$$

with $\nu = 1(-1)$ for the (anti-)symmetric case. Next, define the exchange operator P which switches the two particles in a state $|x, y\rangle$: $P|x, y\rangle = |y, x\rangle$. If the state $|x, y\rangle$ is symmetric, then $|x, y\rangle = |y, x\rangle$; if it is anti-symmetric, then $|x, y\rangle = -|y, x\rangle$.

Applying P to $|\Psi\rangle$ necessarily requires $\mathcal{H}_A = \mathcal{H}_B$, and hence $n = m$. So

$$\begin{aligned} P|\Psi\rangle &= \sum_{i,j=1}^{n} a_i b_j \left(|j\rangle_A|i\rangle_B + \nu|i\rangle_A|j\rangle_B\right) \\ &= \nu \sum_{i,j=1}^{n} a_i b_j \left(|i\rangle_A|j\rangle_B + \nu|j\rangle_A|i\rangle_B\right) = \nu|\Psi\rangle. \end{aligned} \tag{B.4}$$

The eigenvalue of P, i.e. ν, tells us whether the state $|\Psi\rangle$ is symmetric or anti-symmetric. Next, consider two $n \times n$ unitary matrices U_1 and U_2 which change the bases of $\mathcal{H}_A$ and $\mathcal{H}_B$, respectively, to any other bases. It turns out that P commutes with the change of basis transformation $U_1 \otimes U_2$ if $U_1 = U_2$. To see this, consider

$$(U_1 \otimes U_1)P|\Psi\rangle = (U_1 \otimes U_1)\nu|\Psi\rangle = \nu(U_1 \otimes U_1)|\Psi\rangle, \tag{B.5}$$

and, since U_1 maps a basis to another basis, we have

$$\begin{aligned} P(U_1 \otimes U_1)|\Psi\rangle &= P\sum_{i,j=1}^{n} a_i b_j \left(U_1|i\rangle_A U_1|j\rangle_B + \nu U_1|j\rangle_A U_1|i\rangle_B\right) \\ &= \sum_{i,j=1}^{n} a_i b_j \left(U_1|j\rangle_A U_1|i\rangle_B + \nu U_1|i\rangle_A U_1|j\rangle_B\right) \\ &= \nu(U_1 \otimes U_1)|\Psi\rangle. \end{aligned} \tag{B.6}$$

So, $P|\Psi\rangle = \nu|\Psi\rangle \implies P(U_1 \otimes U_1)|\Psi\rangle = \nu(U_1 \otimes U_1)|\Psi\rangle$. The symmetry of a state is hence unchanged by an arbitrary change of basis.

B.3 R/R^{-1} shift between photons A and B

Here we outline how to shift the R dependence from photon A to photon B in Eq. 3.8 of Chapter 3. First, note that given a bijective mapping $\sigma : S_1 \to S_2$ from a finite set S_1 to a finite set S_2 (with $|S_1| = |S_2|$), the sum of the values of a function f evaluated

on mapped elements of S_1, i.e. $\sum_{m\in S_1} f(\sigma(m))$, is equal to the sum of the values of f evaluated on elements of the mapped set S_2, i.e. $\sum_{n\in S_2} f(n)$. That is to say, since $\sigma(S_1) = S_2$, we have $\sum_{m\in S_1} f(\sigma(m)) = \sum_{m\in\sigma(S_1)} f(m)$. This idea can be extended to the following identity for arbitrary functions f and g, where σ^{-1} is the inverse bijection

$$\sum_{m\in S_1} f(\sigma(m))g(m) = \sum_{m\in\sigma(S_1)} f(m)g(\sigma^{-1}(m)). \tag{B.7}$$

Next, if we assume that the pixels of the SLM screen are small enough that every pixel in the transverse plane after the rotation R can be associated with a unique pixel in the original unrotated plane, then R is a bijection. In fact, R is a particular type of bijection, called a permutation, since the domain and range of R are the same set. As such, there exists an inverse permutation, R^{-1}, which represents a rotation of the transverse plane by the same magnitude as R but in the opposite direction. With R as the permutation and applying Eq. B.7 to the first term of Eq. 3.8, we obtain

$$\sum_{\boldsymbol{r}\in\mathcal{S}} c(\boldsymbol{r})|R\boldsymbol{r}\rangle_A|\boldsymbol{r}\rangle_B = \sum_{\boldsymbol{r}\in R(\mathcal{S})} c(R^{-1}\boldsymbol{r})|\boldsymbol{r}\rangle_A|R^{-1}\boldsymbol{r}\rangle_B, \tag{B.8}$$

with $\mathcal{S}$ the set of discrete pixel positions. However, the permutation R is simply a rearrangement of the elements of $\mathcal{S}$, and since we are summing over all pixels, we can replace $R(\mathcal{S})$ with $\mathcal{S}$ above. Finally, under the assumption that the probability amplitudes $c(\boldsymbol{r})$ are invariant under rotations (a paraxial pump beam, along with most optical components in typical quantum optics setups, are often agnostic to rotations of the transverse coordinates and so this assumption is reasonable), Eq. 3.8 is equal to

$$|\Psi_{bs}\rangle = \mathcal{K}\sum_{\boldsymbol{r}} c(\boldsymbol{r})|\boldsymbol{r}\rangle_A\left(|R^{-1}\boldsymbol{r}\rangle_B - |R\boldsymbol{r}\rangle_B\right). \tag{B.9}$$

B.4 Different measurement schemes

Here we make some brief comments on the theory behind the two ghost imaging measurement schemes described in Section 3.4.1 of Chapter 3.

B.4.1 Single pixel scan

Given an object O masked on $\mathrm{SLM_A}$, after dividing $\mathrm{SLM_B}$ into a set of pixels every such pixel has a unique 2D position vector $\boldsymbol{r}$. Switching on pixel $\boldsymbol{r}_i$ on $\mathrm{SLM_B}$ and turning off all other pixels (or, more precisely, coupling only photons incident on pixel $\boldsymbol{r}_i$ to the avalanche photodiode) can be represented by the operator $\langle M_i|_B = \langle \boldsymbol{r}_i|_B$.

Then the observables $|p_{nbs,i}|^2$ or $|p_{bs,i}|^2$ (which can be interpreted as the number of coincidence counts per unit time), which correspond respectively to Eqs. 3.10 and 3.11 from Section 3.3.3, are given by

$$p_{nbs,i} = \langle M_i|_B \langle O|\Psi_{nbs}\rangle = \mathcal{N}^* c(\boldsymbol{r}_i) O(R\boldsymbol{r}_i), \tag{B.10}$$

$$p_{bs,i} = \langle M_i|_B \langle O|\Psi_{bs}\rangle = \mathcal{N}^* c(\boldsymbol{r}_i) \left(O(R\boldsymbol{r}_i) - O(R^{-1}\boldsymbol{r}_i)\right). \tag{B.11}$$

Repeating this process for every pixel i in $\mathrm{SLM_B}$ gives a set of observables $\{|p_{nbs,i}|^2\}$ or $\{|p_{bs,i}|^2\}$ which can be used to reconstruct the original ghost object O according to $O(\boldsymbol{r}_i) = |p_{nbs/bs,i}|^2$.

B.4.2 Random mask scan

For this protocol, given the same object O from before, we generate a set of N random binary 50:50 black:white masks $\{M_i\}$. For the ith mask, loading the measurement SLM ($\mathrm{SLM_B}$) with M_i can be represented by the operator $\langle M_i|_B = w_i^* \sum_{\boldsymbol{s}} M_i^*(\boldsymbol{s}) \langle \boldsymbol{s}|_B$, where all information about the ith mask is contained in the binary function $M_i(\boldsymbol{s}) \in \{0, 1\}$. Note that this scheme could be adapted to random masks with any arbitrary ratio of black:white pixels. If all generated random masks have the exact same ratio (as in our case), the coefficients w_i will all be equal in magnitude (practically, the observed coincidence count values would all be normalised with respect to the same mean value). As such, w_i can be absorbed into $\mathcal{N}$ in which case the observables $|m_{nbs,i}|^2$ or $|m_{bs,i}|^2$ (which are again interpreted as the coincidence count rates) are given by

$$m_{nbs,i} = \langle M_i|_B \langle O|\Psi_{nbs}\rangle = \mathcal{N}^* \sum_{\boldsymbol{r}} c(\boldsymbol{r}) O(R\boldsymbol{r}) M_i^*(\boldsymbol{r}), \tag{B.12}$$

$$m_{bs,i} = \langle M_i|_B \langle O|\Psi_{bs}\rangle = \mathcal{N}^* \sum_{\boldsymbol{r}} c(\boldsymbol{r}) \left(O(R\boldsymbol{r}) - O(R^{-1}\boldsymbol{r})\right) M_i^*(\boldsymbol{r}). \tag{B.13}$$

Finally, the original object O, for a sufficiently large random mask set (i.e. $N \gg 1$) can be reconstructed from the convex sum $O(\boldsymbol{r}) \approx \sum_{i=1}^{N} |m_{nbs/bs,i}|^2 M_i(\boldsymbol{r})$.

Appendix C

Chapter 4 appendix

C.1 Unruh-DeWitt simulation variables

Tables C.1 to C.3 give the parameters and functions used in the simulations in Chapter 4, with $d = 3$, $m = 0$, $\sigma = 1/10$, $\mathbf{p}_p = (0, 0, -2\pi)$ and $f(x, y, z) = \mathscr{N} e^{-(x^2+y^2+z^2)/2\sigma^2}$.

Function/Parameter	**Value**
λ, τ	$1, 0$
$X_1^\mu(\tau)$	$(\tau, 1, 0, 0)$
$X_2^\mu(\tau)$	$(\tau, -1, 0, 0)$

Table C.1 Variables for 2 detector inertial example.

Function/Parameter	**Value**
λ, τ	$1, 0$
r, θ	$1, \pi/6$
$X_1^\mu(\tau)$	$(\tau, r\cos(\theta), r\sin(\theta), 0)$
$X_2^\mu(\tau)$	$(\tau, r\cos(\theta), -r\sin(\theta), 0)$
$X_3^\mu(\tau)$	$(\tau, -r\cos(\theta), -r\sin(\theta), 0)$
$X_4^\mu(\tau)$	$(\tau, -r\cos(\theta), r\sin(\theta), 0)$

Table C.2 Variables for 4 detector inertial example.

Function/Parameter	**Value**
λ, r, θ	1, 1, 0
a	$\frac{1}{r\cos(\theta)}$
$X_1^\mu(\tau)$	$(\frac{1}{a}\sinh(a\tau), \frac{1}{a}\cosh(a\tau), r\sin(\theta), 0)$
$X_2^\mu(\tau)$	$(\tau, -\frac{1}{a}, r\sin(\theta), 0)$

Table C.3 Variables for 2 detector non-inertial example.